New concepts in infrared photodetector designs

P. Martyniuk, J. Antoszewski, M. Martyniuk, L. Faraone, and A. Rogalski

---

Articles you may be interested in

Three color infrared detector using InAs/GaSb superlattices with unipolar barriers
Appl. Phys. Lett. **98**, 121106 (2011); 10.1063/1.3570687

Third-generation infrared photodetector arrays
J. Appl. Phys. **105**, 091101 (2009); 10.1063/1.3099572

Assessment of quantum dot infrared photodetectors for high temperature operation
J. Appl. Phys. **104**, 034314 (2008); 10.1063/1.2968128

Graded band gap for dark-current suppression in long-wave infrared W-structured type-II superlattice photodiodes
Appl. Phys. Lett. **89**, 121114 (2006); 10.1063/1.2356697

Monolithic integration of near-infrared Ge photodetectors with Si complementary metal–oxide–semiconductor readout electronics
Appl. Phys. Lett. **80**, 3268 (2002); 10.1063/1.1477267

APPLIED PHYSICS REVIEWS—FOCUSED REVIEW

New concepts in infrared photodetector designs

P. Martyniuk,[1] J. Antoszewski,[2] M. Martyniuk,[2] L. Faraone,[2] and A. Rogalski[1]

[1]*Institute of Applied Physics, Military University of Technology, 2 Kaliskiego Str., 00-908 Warsaw, Poland*
[2]*School of Electrical, Electronic and Computer Engineering, The University of Western Australia, Crawley 6009, Australia*

In 1959, Lawson and co-workers published the paper which triggered development of variable band gap $Hg_{1-x}Cd_xTe$ (HgCdTe) alloys providing an unprecedented degree of freedom in infrared detector design. HgCdTe ternary alloy has been used for realization of detectors operating under various modalities including: photoconductor, photodiode, and metal-insulator-semiconductor detector designs. Over the last five decades, this material system has successfully overcome the challenges from other material systems. It is important to notice that none of these competitors can compete in terms of fundamental properties. The competition may represent more mature technology but not higher performance or, with the exception of thermal detectors, higher operating temperatures (HOTs) for ultimate performance. In the last two decades, several new concepts for improvement of the performance of photodetectors have been proposed. These new concepts are particularly addressing the drive towards the so called HOT detectors aiming to increase detector operating temperatures. In this paper, new strategies in photodetector designs are reviewed, including barrier detectors, unipolar barrier photodiodes, multistage detectors and trapping detectors. Some of these new solutions have emerged as a real competitor to HgCdTe photodetectors. © 2014 AIP Publishing LLC. [http://dx.doi.org/10.1063/1.4896193]

TABLE OF CONTENTS

I. INTRODUCTION

The years during World War II saw the origins of the modern infrared (IR) detector technology. Photon IR technology combined with semiconductor material science, photolithography technology developed for integrated circuits, and the impetus of Cold War arms race have propelled extraordinary advances in IR capabilities within a short time period during the last century.[1] In 1959, the publication of Lawson and co-workers[2] triggered development of variable band gap $Hg_{1-x}Cd_xTe$ (HgCdTe) alloys providing an unprecedented degree of freedom in infrared detector design.

HgCdTe is a pseudo-binary alloy semiconductor that crystallizes in the zinc blende structure. Because of its bandgap tunability with composition x, $Hg_{1-x}Cd_xTe$ has become the most important/versatile material for detector applications over the entire IR range. As the Cd composition increases, the $Hg_{1-x}Cd_xTe$ energy bandgap gradually increases from a negative value for HgTe to a positive value for CdTe. The bandgap energy tunability allows this material to be used in IR detector applications spanning the short wavelength IR (SWIR: 1–3 μm), middle wavelength IR (MWIR: 3–5 μm), long wavelength IR (LWIR: 8–14 μm), and very LWIR (VLWIR: 14–30 μm) ranges.

HgCdTe technology development was and continues to be primarily driven by military applications. A negative aspect attached to the support of defense agencies has been the associated secrecy requirements that inhibit meaningful collaborations among research teams on a national and especially on an international level. In addition, the primary focus has been on the development of focal plane arrays (FPAs) rather than on establishing the knowledge base. Nevertheless, significant progress has been made over last

five decades. At present, HgCdTe is the most widely used variable gap semiconductor for IR photodetectors.

The specific advantages of HgCdTe are the direct energy gap, ability to obtain both low and high carrier concentrations, high mobility of electrons, and low dielectric constant. The extremely small change of lattice constant with composition makes growth of high quality layers and heterostructures possible. HgCdTe can be used for detectors operating under various modalities (photoconductors, photodiodes, and metal-insulator-semiconductor (MIS) detectors), and can be optimized for operation within an extremely wide range of the IR spectrum (from visible region to 30 μm) and at temperatures ranging from that of liquid helium to room temperature.

The main motivations to replace HgCdTe are associated with technological problems associated with processing of this material. Many of them originate with the weak Hg-Te bond, and the resulting bulk, surface and interface instabilities. Uniformity and yield are still issues in need of addressing, especially in the LWIR spectral range. Nevertheless, HgCdTe remains the leading semiconductor for IR detectors.

HgCdTe has inspired the development of the four "generations" of IR detector devices (see Fig. 1). The late 1960s and early 1970s saw the development of the first-generation based on photoconductor linear arrays. These systems relied on scanning optics and did not include multiplexing functions in the focal plane. In the mid-1970s, attention turned to the photodiodes for passive IR imaging applications and is generally considered as the onset on the second generation of IR detectors. In contrast to photoconductors, photodiodes with their very low power dissipation, inherently high impedance, negligible 1/f noise, and easy multiplexing on focal plane silicon chip can be assembled in two-dimensional (2-D) arrays containing more than a megapixel of elements, limited only by existing processing

technologies. The main attention turned towards HgCdTe photodiodes with the idea of an all-solid-state electronically scanned 2-D IR detector array instigated with the invention of charge coupled devices (CCDs) by Boyle and Smith.[3] By the end of 1970s, the emphasis was directed towards large photovoltaic HgCdTe arrays in the MW and LW spectral bands for thermal imaging. Recent efforts have been extended to short wavelengths, e.g., for starlight imaging in the SW range, as well as to VLWIR space borne remote sensing beyond 15 μm.

The third generation HgCdTe and type-II superlattice (T2SL) systems continue to be currently developed, and concept development towards the so-called fourth generation systems was also recently initiated. The definition of fourth generation systems is not well established. These systems provide enhanced capabilities in terms of greater number of pixels, higher frame rates, better thermal resolution, as well as, multicolor functionality and other on-chip functions. Multicolor capabilities are highly desirable for advanced IR systems. Collection of data in distinct IR spectral bands can discriminate for both the absolute temperature and the unique signature of objects within the scene. By providing this new dimension of contrast, multiband detection also offers advanced color processing algorithms to further improve sensitivity compared to that of single-color devices. It is expected that the functionalities of fourth generation systems could manifest themselves as spectral, polarization, phase, or dynamic range signatures that could extract more information from a given scene.[4] For example, Fig. 2 shows the first demonstration of a monolithically integrated plasmonic FPA camera in the mid-infrared region, using a metal with a two-dimensional hole array on top of an intersubband quantum-dots-in-a-well (DWELL) heterostructure FPA coupled to a read-out integrated circuit.[5] This camera opens
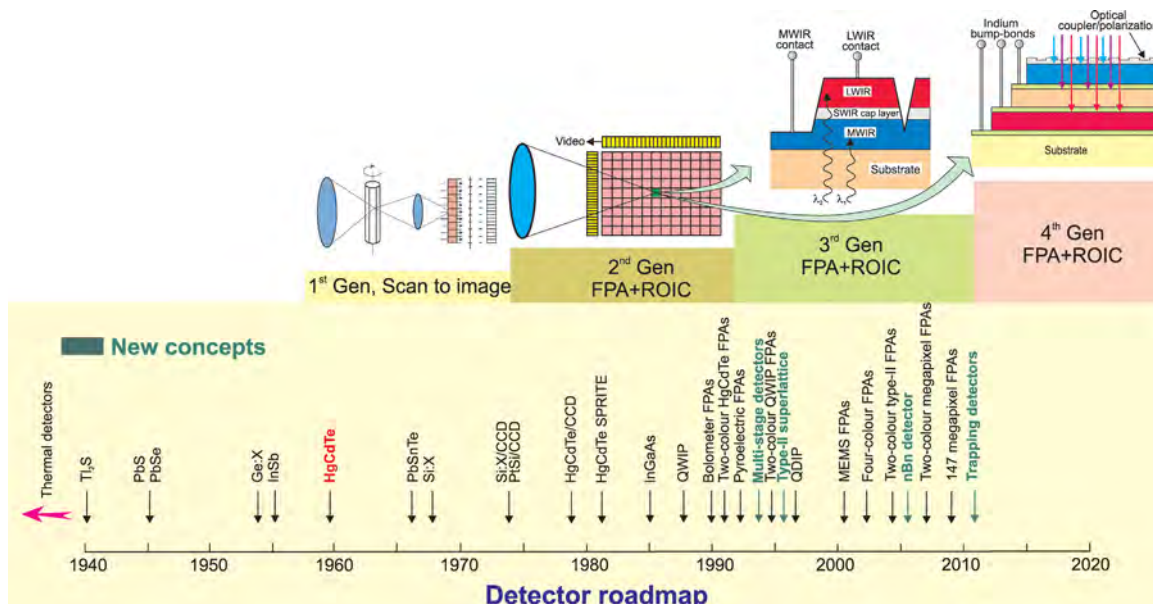
FIG. 1. History of the development of infrared detectors and systems. New types of detectors considered in this paper are marked by blue color. Four generation systems can be considered for principal military and civilian applications: first generation (scanning systems), second generation (staring systems–electronically scanned) third generation (staring systems with large number of pixels and two-color functionality), and fourth generation (staring systems with very large number of pixels, multi-color functionality and other on-chip functions; e.g., better radiation/pixel coupling, avalanche multiplication in pixels, and polarization/phase sensitivity).

FIG. 2. Schematic of the plasmonic DWELL focal plane array. (a) Heterostructure schematic and band diagram of the DWELL absorber. (b) Schem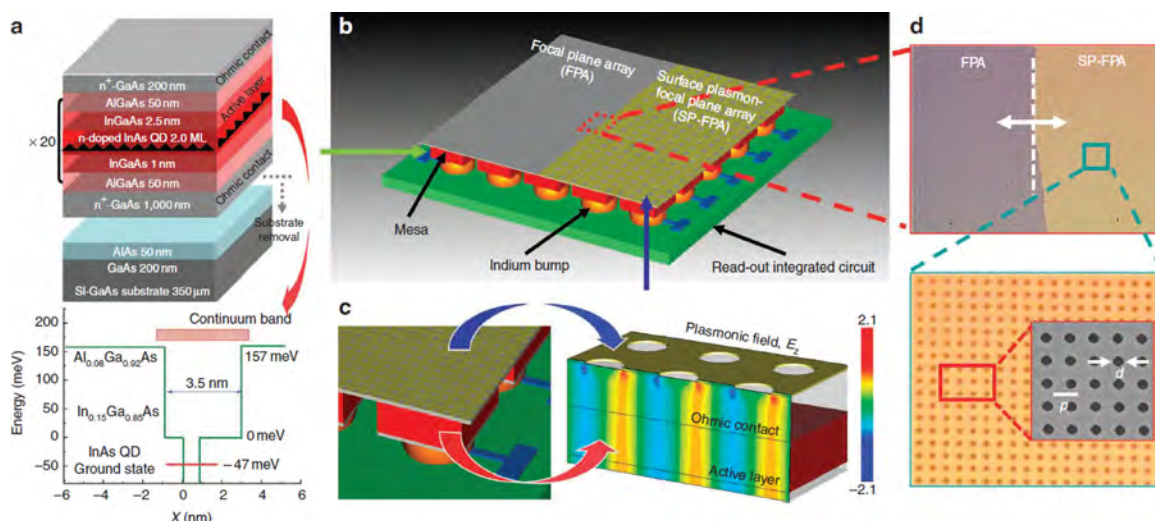atic view of the surface plasmon (SP) structure defined on one half of the DWELL FPA after hybridization with a read-out integrated circuit and subsequent substrate removal. (c) Zoomed-in image showing the FPA bonded to the ROIC along with the SP electric field profile. (d) Visible images of the two halves of the FPA clearly showing the non-plasmonic and plasmonic sections. The orthogonal pitches of the two-dimensional grating are both fixed at 1.79 μm (p). The metal thickness is about 50 nm. The circular aperture size (d) is fixed at 0.5 p. Reprinted with permission from Lee *et al.*, Nat. Commun. **2**, 286 (2011). Copyright 2011 Macmillan Publishers Ltd.

the way for development of pixel-level color-vision spectro-polarimetric imagers.

Cryogenic cooling of detectors has always been the burden of sensitive IR systems. Many efforts have been made to develop imaging IR systems that would not require cryogenic cooling. During the last two decades, we have observed a revolutionary emergence of FPAs based on thermal detectors, i.e., bolometers and pyroelectric devices. At present, full television-compatible arrays are used, but they cannot be expected to replace the high-performance cryogenically cooled arrays without a scientific breakthrough. A response much shorter than that achievable with thermal detectors is required for many applications. Thermal detectors seem to be unsuitable for the IR thermal imaging systems, which are moving toward faster frame rates and multispectral operation. A response time much shorter than that achievable with thermal detectors is also required for many non-imaging applications. Photon detectors (photodetectors) make it possible to achieve both high sensitivity and fast response. Recent considerations of the fundamental photodetector mechanisms suggest that, in principle, near-perfect detection can be achieved in the MWIR and LWIR ranges without the need for cryogenic cooling.[6–8]

A number of concepts to improve performance of high-operating temperature (HOT) photodetectors have been proposed. Apart from photoconductive detectors and photodiodes, three other types of IR photodetectors can operate at near room temperature; photoelectromagnetic (or PEM) detectors, magnetoconcentration detectors, and Dember effect detectors. While significant improvements have been obtained by suppression of Auger thermal generation in excluded photoconductors[9] and extracted photodiodes,[10,11] these non-equilibrium devices require significant bias currents and exhibit excessive low frequency 1/f noise that extends up to MHz range.

Recently, there has been considerable progress towards new materials development and device design innovations. In particular, significant advances have been made during the last two decades in the area of band-gap engineering of various compound semiconductors that has led to new detector architectures. New emerging strategies include barrier structures such as nBn detector, low-dimensional solids (especially T2SLs) with lower generation-recombination leakage mechanisms, photon trapping detectors, and multi-stage/cascade infrared devices.

This review paper presents approaches, materials, and device structures of the new types of infrared detectors. The intent is to focus on designs having the largest impact on the main stream of infrared detector technologies today. A secondary aim is to outline the evolution of detector technologies showing why certain device designs and architectures have emerged recently as technologies alternative to the HgCdTe ternary alloy. The third goal is to emphasize the applicability of novel detectors in design of FPAs.

II. FUNDAMENTAL PERFORMANCE LIMITS OF INFRARED PHOTODETECTORS

In general, the detectivity (D^*) of an infrared photodetector is limited by generation and recombination rates G and R in the active region of the device. It can be expressed as[12,13]

$$D^* = \frac{\lambda}{2^{1/2}hc(G+R)^{1/2}} \left(\frac{A_o}{A_e}\right)^{1/2} \frac{\eta}{t^{1/2}},\qquad(1)$$

where λ is the wavelength, h is the Planck's constant, c is the velocity of light, and η is the quantum efficiency. Here, the detector is considered as a slab of homogeneous semiconductor with actual "electrical" area, A_e, thickness, t, and

volume, $A_e t$. Usually, the optical (A_o) and electrical areas of the device are the same or similar. However, the use of some kind of optical coupler/concentrator can increase the A_o/A_e ratio by a large factor.

For a given wavelength and operating temperature, the highest performance can be obtained by maximizing the ratio of the quantum efficiency to the square root of the sum of the sheet thermal generation and recombination rates $\eta/[(G+R)t]^{1/2}$. This means that high quantum efficiency must be obtained with a thin device.

A possible way to improve the performance of IR detectors is to reduce the physical volume of the semiconductor, thus reducing the amount of thermal generation. However, this must be achieved without decrease in quantum efficiency, optical area, and field of view (FOV) of the detector.

The detectivity of an optimized infrared photodetector is limited by thermal processes in the active region of the device. It can be expressed as[12,13]

$$D^* = 0.31 \frac{\lambda}{hc} k \left(\frac{\alpha}{G}\right)^{1/2}, \tag{2}$$

where $1 \leq k \leq 2$, and is dependent on the contribution of recombination and backside reflection. The k-coefficient can be modified by using more sophisticated coupling of the detector with IR radiation, e.g., using photonic crystals or surface plasmon-polaritons.

The ratio of the absorption coefficient to the thermal generation rate, α/G, is the fundamental figure of merit of any material intended for infrared photodetection. The α/G ratio versus temperature for various material systems capable of band gap tuning is shown in Fig. 3 for a hypothetical energy gap equal to 0.25 eV ($\lambda = 5\,\mu$m) (Fig. 3(a)) and 0.124 eV ($\lambda = 10\,\mu$m) (Fig. 3(b)). Procedures used in calculations of α/G for different material systems are given in Ref. 14. Analysis shows that the narrow gap semiconductors are more suitable for high temperature photodetectors in comparison to competing technologies such as extrinsic devices, QWIP (quantum well IR photodotector), and QDIP (quantum dot IR photodotector) devices. The main reason for high performance of intrinsic photodetectors is high density of states in the valence and conduction bands, which results in strong absorption of infrared radiation. Figure 3(b) predicts that recently emerging competing IR material, type-II SL, is the most efficient material technology for IR

detection in long wavelength region, theoretically perhaps even better than HgCdTe. It is characterized by a high absorption coefficient and relatively low fundamental (band-to-band) thermal generation rate. However, this theoretical prediction has not been confirmed by experimental data. It is also worth noticing that theoretically AlGaAs/GaAs QWIP is also a better material than extrinsic silicon.

Background radiation is frequently the main source of noise in a detector. Then, background limited infrared performance detectivity, D^*_{BLIP}, is

$$D^*_{BLIP} = \frac{\lambda}{hc}\left(\frac{\eta}{\phi_B}\right)^{1/2}, \tag{3}$$

where ϕ_B is the background photon flux density. Once background-limited performance is reached, quantum efficiency, η, is the only detector parameter that can influence detector's performance.

Figure 4 shows the spectral detectivity of a background limited photodetector operating at 300, 230, and 200 K versus the wavelength calculated for 300 K background radiation and hemispherical FOV ($\theta = 90$ deg). The minimum D^*_{BLIP} (300 K) occurs at 14 μm and is equal to 4.6×10^{10} cmHz$^{1/2}$/W. For some photodetectors which operate at near equilibrium conditions–such as non-sweep-out photoconductors, the recombination rate is equal to the generation rate. For these detectors, the contribution of recombination to the noise will reduce D^*_{BLIP} by a factor of $2^{1/2}$. Note that D^*_{BLIP} does not depend on area and the A_o/A_e ratio. As a consequence, the background limited performance cannot be improved by making A_o/A_e large.

It is interesting to consider the performance requirements of near-room temperature photodetectors for thermal cameras. Thermal resolution of infrared thermal systems is usually characterized by the noise equivalent temperature difference (*NETD*). It can be shown that[1]

$$NETD = \frac{4F^2 \Delta f^{1/2}}{A_d^{1/2} t_{op}} \left[\int_{\lambda_a}^{\lambda_b} \frac{dM}{dT} D^*(\lambda) d\lambda\right]^{-1}, \tag{4}$$

where F is the optics f-number, Δf is the frequency band, A_d is the detector area, t_{op} is the optics transmission, and M is the spectral emittance of the blackbody described by the Planck's law.
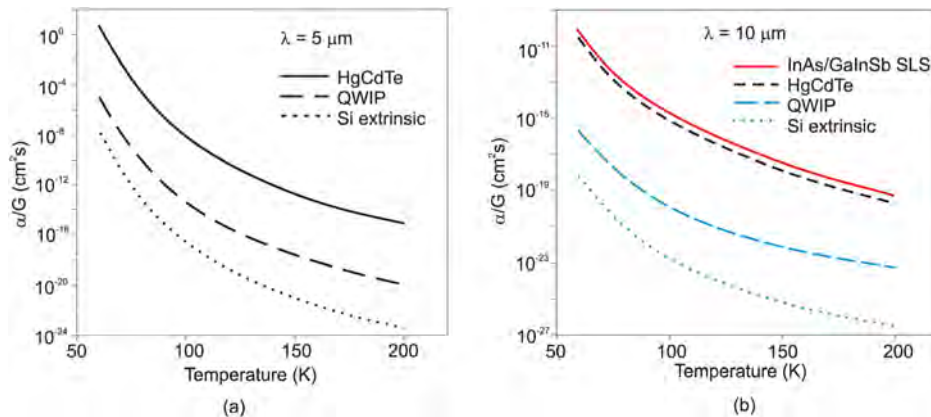

FIG. 3. α/G ratio versus temperature for (a) MWIR–$\lambda = 5\,\mu$m, and (b) LWIR–$\lambda = 10\,\mu$m photodetectors based on HgCdTe, QWIP, Si extrinsic, and type-II superlattice (for LWIR only) material technology. From J. Piotrowski and A. Rogalski, *High-Operating Temperature Infrared Photodetectors*. Copyright 2007 SPIE Press. Reproduced by permission of SPIE.
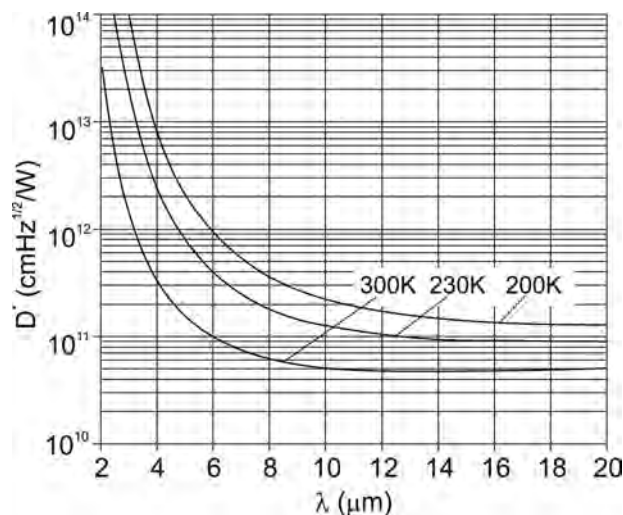
FIG. 4. Calculated spectral detectivities of a photodetector limited by the hemispherical FOV background radiation of 300 K as a function of the peak wavelength for detector operating temperatures of 300, 230, and 200 K. From J. Piotrowski and A. Rogalski, *High-Operating Temperature Infrared Photodetectors*. Copyright 2007 SPIE Press. Reproduced by permission of SPIE.
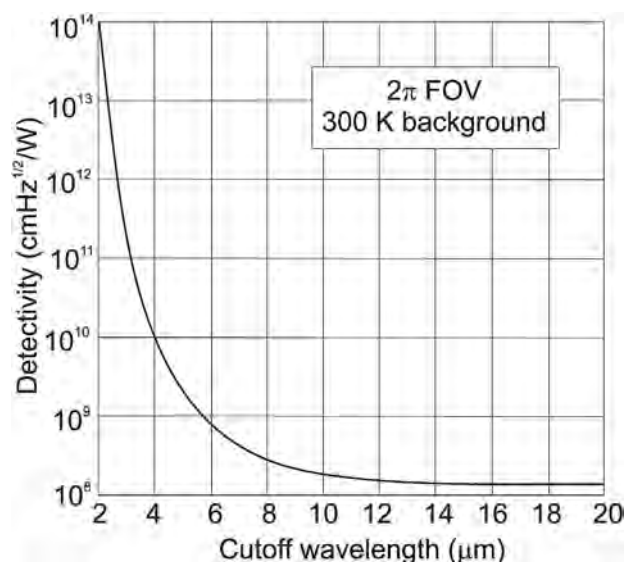

FIG. 5. Detectivity needed to obtain $NETD = 0.1$ K in a photon counter detector thermal imager as a function of cutoff wavelength. From J. Piotrowski and A. Rogalski, *High-Operating Temperature Infrared Photodetectors*. Copyright 2007 SPIE Press. Reproduced by permission SPIE.

As Eq. (4) shows, the thermal resolution improves with an increase in detector area. However, increasing detector area results in reduced spatial resolution. Hence, a reasonable compromise between the requirement of high thermal and spatial resolution is necessary. Improvement of thermal resolution without detrimental effects on spatial resolution may be achieved by:

- an increase of detector area combined with a corresponding increase of focal length and the objective aperture,
- improved detector performance, and
- an increase in number of detectors.

Increase of aperture is undesirable because it increases sizes, mass, and price of an IR system. It is more appropriate to use a detector with higher detectivity. This can be achieved by better coupling of the detector with the incident radiation. Another possibility is the application of multi-elemental sensor, which reduces each element bandwidth proportionally to the number of elements for the same frame rate and other parameters.

Figure 5 shows the dependence of detectivity on the cut-off wavelength for a photodetector thermal imager with a re-solution of 0.1 K. Detectivities of 1.9×10^8 cmHz$^{1/2}$/W, 2.3×10^8 cmHz$^{1/2}$/W, and 2×10^9 cmHz$^{1/2}$/W are necessary to obtain $NETD = 0.1$ K for 10 μm, 9 μm, and 5 μm cutoff wavelength, respectively. The above estimations indicate that the ultimate performance of the uncooled photodetectors is not sufficient to achieve a thermal resolution of 0.1 K. The thermal resolution below 0.1 K is achieved for staring thermal imagers containing thermal FPAs.

III. TRENDS IN INFRARED FOCAL PLANE ARRAYS

Infrared focal plane arrays are critical components in many of the military and civilian applications for advanced imaging systems. In this section, we focus on the continuing requirements for extended detector capability to support applications for future generations of infrared sensor systems.

Figure 6 illustrates the trend in array size over the past 40 years. Imaging IR FPAs have been developing in-line with the ability of silicon integrated circuit (ICs) technology to read and process the array signals, and also to display the resulting image. The progress in IR arrays has also been steady mirroring the development of dense electronic structures such as dynamic random access memories (DRAMs). FPAs have had nominally the same development rate as DRAM ICs, which have followed the Moore's Law with a doubling-rate period of approximately 18 months; however, with FPAs lagging DRAMs by about 5–10 years. The 18-month doubling time is evident from the slope of the graph presented in the inset of Fig. 6, which shows for MWIR FPAs, the log of the number of pixels per array as a function of the first year of commercial availability. CCDs with close to 2 gigapixels offer the largest formats.

IR array sizes will continue to increase, but perhaps at a rate that falls below the Moore's Law trend. An increase in array size is already technically feasible. However, the market demand for larger arrays is not as strong as before the megapixel milestone was achieved. In particular, astronomers were the driving force towards the day when the optoelectronic arrays could match the size of the photographic film. Since large arrays dramatically multiply the data output of a telescope system, the development of large format mosaic sensors of high sensitivity for ground-based astronomy is the goal of many astronomic observatories around the world. This is somewhat surprising given the comparative budgets of the defense market and the astronomical community.

Infrared photodetectors are typically operated at cryogenic temperatures to decrease the noise of the detector arising from various mechanisms associated with the narrow
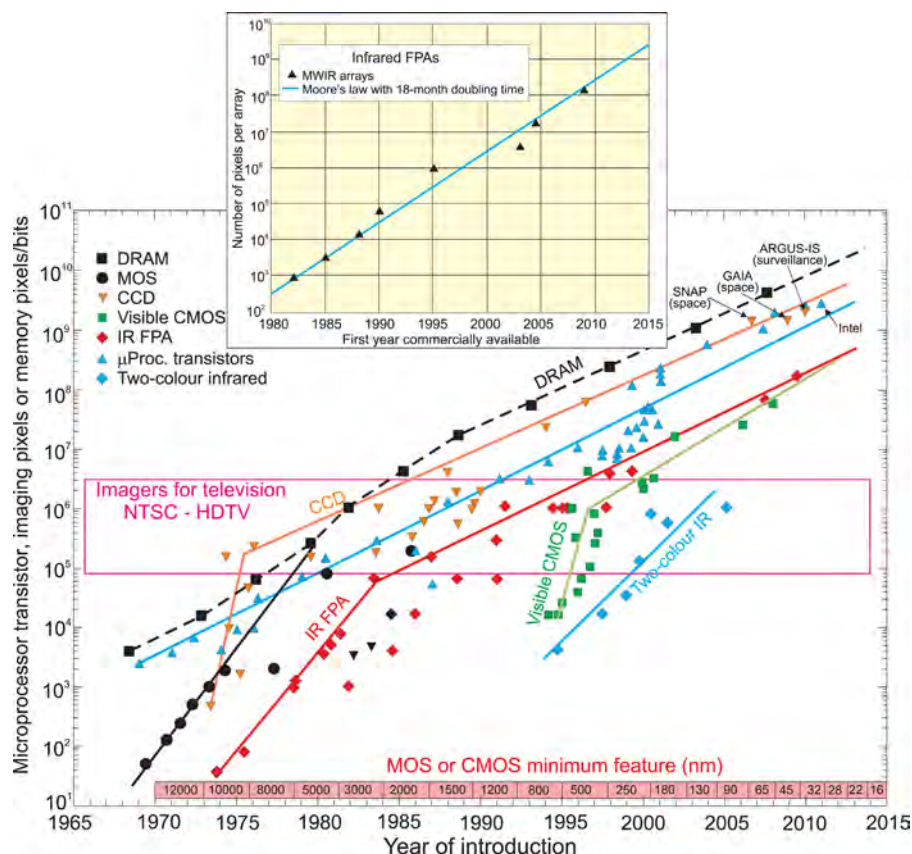
FIG. 6. Imaging array formats compared with the complexity of silicon microprocessor technology and dynamic access memory (DRAM) as indicated by transistor count and memory bit capacity. Adapted from Ref. 15 with completions. The timeline design rule of MOS/CMOS features is shown at the bottom. CCDs with close to 2 gigapixels offer the largest formats. Note the rapid rise of CMOS imagers which are challenging CCDs in the visible spectrum. The number of pixels on an infrared array has been growing exponentially, in accordance with Moore's Law, for 30 years with a doubling time of approximately 18 months. Infrared arrays with size above 100 mega pixels are now available for astronomy applications. Imaging formats of many detector types have gone beyond that required for high definition television.

band gap. There are considerable efforts to decrease system cost, size, weight, and power consumption, to increase the operating temperature in so-called HOT detectors.

Increasing the operating temperature of detector reduces the cooling load allowing more compact cooling systems with higher efficiency. For example, for an operating temperature of 150 K, the cool-down time and steady state power dissipation in the standard Selex Hawk integrated dewar cooler assembly (IDCA) are reduced by around 40% and 55%, respectively, in comparison to operation at 80 K (see Fig. 7). To achieve near background limited infrared photodetector (BLIP) performance at temperatures above 150 K, the previously optimized engine cooled configuration

consumed 1–2 W in steady state. At present, after improved processing of MWIR HgCdTe photodiode arrays grown by MOCVD, similar performance at temperatures in the range of 200–220 K introduces the opportunity for thermoelectrically cooled operation.

Because the cost of the optics made from Ge (the standard material for IR optics) rises approximately with the square of the lens diameter, the reduction of the pixel size results in significantly reduced cost of the optics. These reductions in optics size would have a major benefit in reducing the overall size, weight, and cost of portable IR systems. In addition, the reduction in pixel size allows for larger number of FPAs to be fabricated on each wafer.

Pixel reduction is also needed to increase the detection and identification range of infrared imaging systems. It appears that, e.g., the detection range of many uncooled IR imaging systems is limited by pixel resolution rather than sensitivity. Figure 8 presents a trade-off analysis of the detection range and sensor optics for a thermal weapon sight using the NVESD NVTherm IP model, assuming a detector sensitivity of 35 mK *NETD* (*F*/1, 30 Hz) for the 25, 17, and 12 μm pitch pixel of uncooled FPAs. The advantages of small pixel pitch and large format FPAs are obvious. By switching to smaller pitch and larger format detectors, the detection range of a weapon sight increases significantly with a fixed optical entrance aperture.

Pixel size as small as 10 μm has been demonstrated. A general trend has been to reduce the pixel size, and this trend is expected to continue. Systems operating at shorter wavelengths are more likely to benefit from small pixel sizes
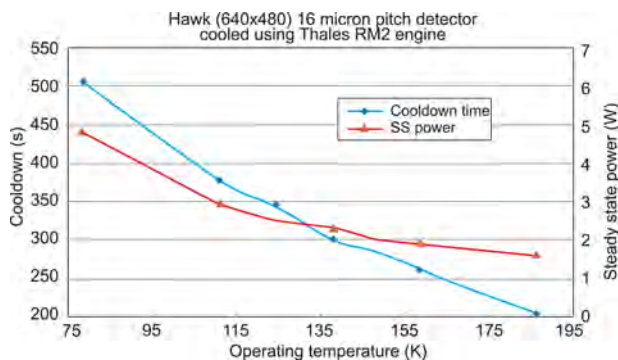

FIG. 7. Selex Hawk IDCA performance in the operating temperature range of 80-195 K (power excludes cooler control electronics losses). Reproduced with permission from Pillans *et al.*, Proc. SPIE **8353**, 83532W (2012). Copyright 2012 SPIE.
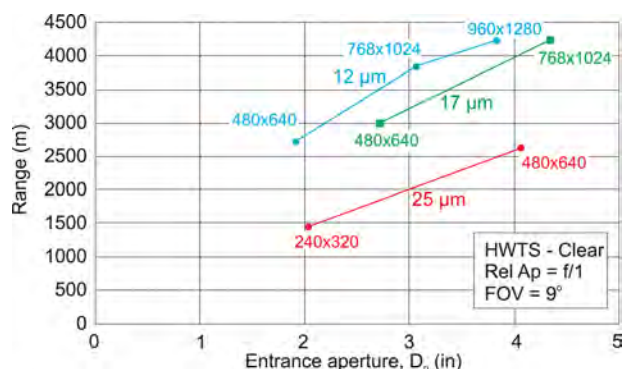
FIG. 8. Calculated detection range as a function of sensor optics for increasing detector pixel size and format using NVESD NVTherm IP modeling, assuming a 35 mK *NETD* (F/1, 30 Hz) for all detectors. Reproduced with permission from Li *et al.*, Proc. SPIE **7298**, 72980S (2009). Copyright 2009 SPIE.

because of the smaller diffraction-limited spot size. Diffraction-limited optics with low f-numbers (e.g., F/1) could benefit from pixels down to the order of one wavelength across; about 10 μm in the LWIR. Over sampling the diffractive spot may provide some additional resolution for smaller pixels, but this saturates quickly as the pixel size is decreased. Pixel reduction is also needed for reduction of system cost (reduction of the optics diameter, dewar size and weight, power, and increase of reliability). The pitch of 15 μm is used in HgCdTe arrays produced today at Sofradir, and pitches of 10-μm and less will be scheduled in short term [see Fig. 9(a)].[16–18] A similar tendency has been observed in the case of microbolometers [see Fig. 9(b)].[19]

The current trend in FPAs for imaging systems is reduction of pixel size with improved spatial resolution if the imaging lens does not limit resolution.[20] Diffraction constrains the maximum spatial frequency transmitted through an optical system to be $\nu_{max} = 1/[\lambda(F)]$, where F is the system f-number. Table I shows the minimum useful pixel pitch as a function of maximum wavelength and F equal to 2 or larger (used in the most high performance systems).[21]

The Darpa Nyquist-Limited Infrared Detectors (NIRD) Program (DARPA-BAA-08–54)[22] has been launched to develop 5-μm pitch IR detectors. This value, if attained, will reach diffraction limit on most practical optical systems.

Taking into account the detector size and system f-number, Driggers *et al.*[23] have recommended LWIR detectors to be fabricated with 5 μm and MWIR with 3 μm size, respectively. It is generally interesting to investigate pixel scaling beyond the diffraction limit using wavelength- and even subwavelength-scale optics that are enabled by modern nanofabrication (diffraction-limited pixel size is still relatively large compared with feature size that can be achieved with state-of-the-art nanofabrication approaches).

IV. COUPLING OF INFRARED RADIATION WITH DETECTOR–A NEW PERSPECTIVE

Advances in optoelectronics related materials science, such as metamaterials and nanostructures, have opened doors for new non-classical approaches to device design methodologies, which are expected to offer enhanced performance along with reduced product cost for wide range of applications. Additionally, plasmonics takes advantage of the very large (and negative) dielectric constant of metals, to compress the wavelength and enhance electromagnetic fields in the vicinity of metal conductors. Coupling light into semiconductor materials remains a challenging and active research topic. Micro- and nano-structured surfaces have become a widely used design tool to increase light absorption and enhance the performance of broadband detectors without employing anti-reflection coatings.

Since absorption coefficient is a strong function of the wavelength, the wavelength range in which an appreciable photocurrent can be generated is limited for a given detector material. So, broadband absorption is usually inadequate due

TABLE I. Minimum useful pixel pitch.

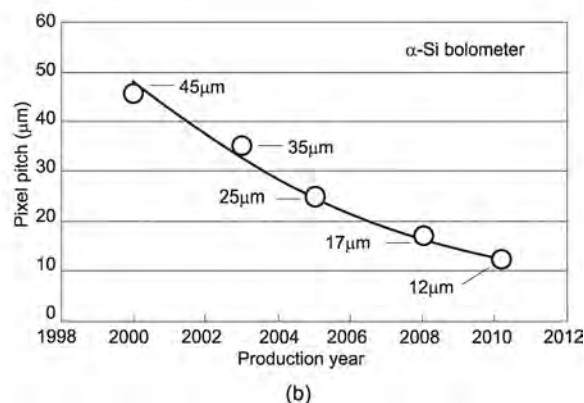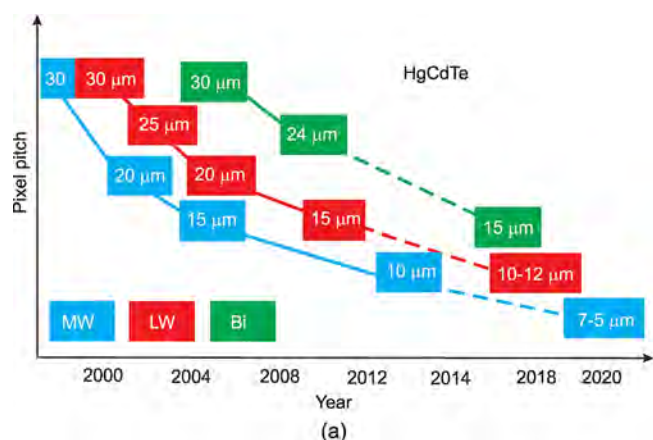| Detection wavelength (μm)	Optics F/#		
	2	3	4
5 μm	5 μm	7.5 μm	10 μm
12 μm	12 μm	18 μm	24 μm

FIG. 9. Pixel pitch for (a) HgCdTe photodiodes, and for (b) amorphous silicon microbolometes have continued to decrease due to technological advancements. Reproduced with permission from Destefanis *et al.*, Proc. SPIE **8012**, 801235 (2011). Copyright 2011 SPIE and see http://www.sofradir-ec.com/wp-uncooled-detectors-achieve.asp for ULIS.
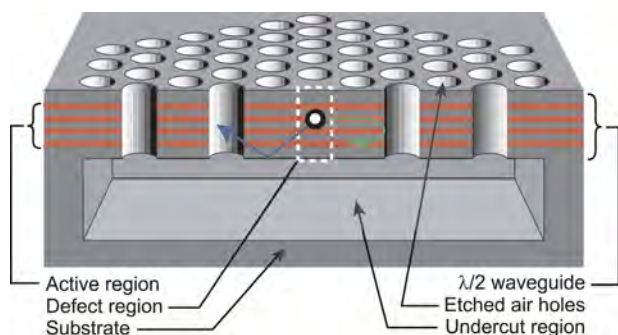
FIG. 10. Cross section through the photonic crystal microcavity.

to quantum efficiency roll-off. Research on photonic crystal (PC) structures with a periodic refractive index modulation has opened up several ways for the control of light. Most existing devices are realized as two-dimensional (2D) PC structures, as they are compatible with standard semiconductor processing.[24–26]

PC crystal represents a regular array of holes (defects) that is used to modify the local refractive index to provide localized modes in the "photonic" band structure (see Fig. 10). By removing a single hole, energy well for photons is formed similar to that of electrons in a quantum wire structure. The periodic variation in the refractive index gives rise to Bragg scattering of photons, which opens up forbidden energy gaps in the in-plane photon dispersion relation. The PC has a grating effect that "diffracts" the normally incident radiation to the in-plane direction. In addition, a $\lambda/2$ high-index slab is used to trap photons in the vertical direction by internal reflection at the air-slab interface. As a result, the combination of Bragg reflection from the 2D PC and internal reflection results in a three-dimensionally (3D) confined optical mode.

An example of metal PC-integrated detector design is shown in Fig. 11 along with a schematic cross sectional view of the sample structure.[26] The PC is a 100 nm-thick Au film perforated with a 3.6 μm period square array of circular holes having diameter of 1.65 ± 0.05 μm. This array of circular holes couples to surface plasma waves at 11.3 and 8.1 μm for reverse and forward bias, respectively, where InAs QDIPs exhibit the strongest detectivity (up to thirty-fold enhancement).

Figure 12 shows the low temperature photoresponse (10 K) of the metal PC QDIP and reference devices at -3.0 V and 3.4 V.[26] The arrows in the figure indicate the reference devices which exhibit two, rather broad colour response with indistinct peaks for both -3.0 V and 3.4 V cases. The peak shift with applied voltage has been interpreted in terms of the quantum confined Stark effect. On the other hand, the metal PC devices have totally different voltage dependent spectral responsivities in both, the peak wavelengths and especially the response intensity. They show four peaks at identical wavelengths but amplitude varying for both biases. The peak at 11.3 μm, which is much stronger than that of the reference device, is dominant for reverse bias while the peak at 8.1 μm is more intense than any other peak for forward bias. The two remaining peaks at 5.8 and 5.4 μm are relatively weak.

Advantage of the above approach is that it can be easily incorporated into the FPA fabrication process of present day infrared sensors. Holes with $2-3$ μm in diameter for a response wavelength range of $8-10$ μm can be defined using conventional optical lithography. An introduction of straightforward modification of a single or multielement defect in the PC can selectively increase the response of photons with a specific energy. Thereby, by changing the dimensions of the defect, the resonance wavelength can be altered leading to the fabrication of a spectral element in each pixel of the FPA. This would have a revolutionary impact on multispectral imaging and hyperspectral imaging detectors.

An important class of 2D PC structures are photonic crystal slabs (PCSs) consisting of a dielectric structure with a periodic modulation in only two dimensions and refractive index guiding in the third. Figure 13(a) shows a QWIP fabricated as a PCS structure.[27] The PC structure is underetched by selective removal of the sacrificial AlGaAs layer to create the free standing PCS. A schematic illustration of the final device is shown in Fig. 13(b). The photoresponse of the PCS-QWIP shows a wider response peak but additionally displays several pronounced resonance peaks.

New solutions are arising with the use of plasmonic structures which open novel avenues for photodetectors development.[28–31] The goal of infrared plasmonics is to increase the absorption in a given volume of detector's material. As mentioned in Sec. II, smaller volumes provide lower
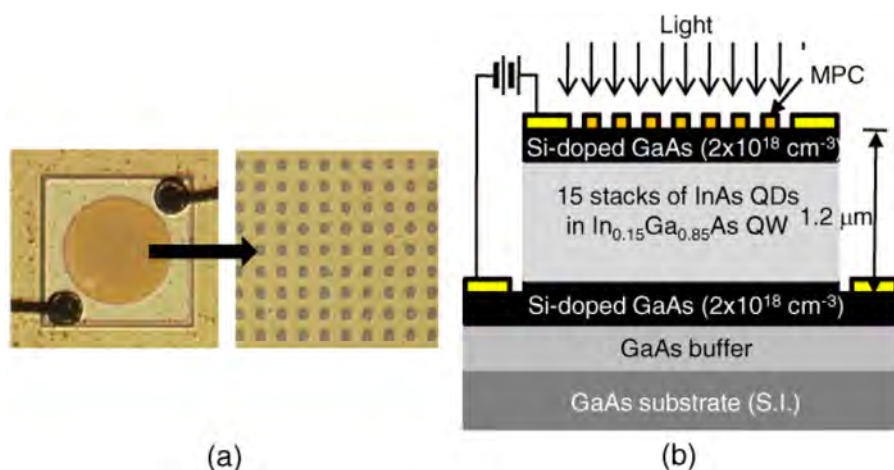

(a)   (b)

FIG. 11. (a) Optical microscope images of the metal PC device with 16 times magnification revealing the details of the metal PC. The period of the circular holes is 3.6 μm; (b) a schematic cross sectional structure of the metal PC device. Reproduced with permission from Lee *et al.*, Opt. Express **17**(25), 23160–23168 (2009). Copyright 2009 The Optical Society.
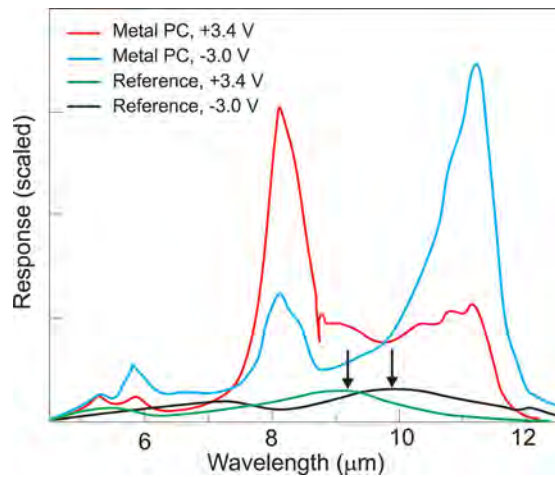
FIG. 12. Spectral response curves of the reference device (two spectra at the bottom with the arrows indicating the highest peak in each spectrum) and the metal PC device (other two spectra with higher responsivity) for −3.0 V and 3.4 V at 10 K. Reproduced with permission from Lee *et al.*, Opt. Express **17**(25), 23160–23168 (2009). Copyright 2009 The Optical Society.
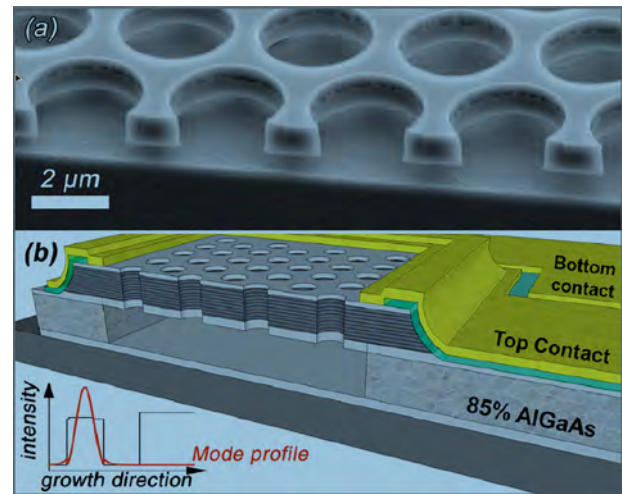

FIG. 13. PCS-QWIP design. (a) SEM image of a cleaved PCS, (b) Cross section through the PCS-QWIP structure. Reprinted with permission from Appl. Phys. Lett. **98**, 011105 (2011). Copyright 2011 AIP Publishing LLC.

noise, while higher absorption results in a stronger output signal. This leads to miniaturized detector structures with length scales that are much smaller than those being currently achieved.

Surface plasmons (SPs) are coherent electron oscillations which exist at the interface between any two materials where the real part of the dielectric function changes sign across the interface (e.g., a metal-dielectric interface, such as a metal sheet in air). When SPs couple with a photon, the resulting hybridized excitation is called a surface plasmon polariton (SPP), a transverse-magnetic optical surface wave that may propagate along the surface of a metal until energy is lost either via absorption in the metal or radiation into free-space.

Schematic representation of an electron density wave propagating along a metal-dielectric interface is shown in Fig. 14. The charge density oscillations and associated electromagnetic fields comprise SPP waves. The local electric field component is enhanced near the surface and decays exponentially with distance in a direction normal to the interface.

Surface plasmon photodetectors typically combine a metallic structure that supports plasmons with photodetection structure based on internal photoemission or electron-hole creation.[30] Different architectures are used to support SPPs on metalo-dielectric structures involving planar metal waveguides, metal gratings, nanoparticles such as islands, spheres, rods, and antennas, or optical transmission through one or many sub-wavelength holes in a metal film. However, great challenges still remain to fully realize many promised potentials.

SPs were first studied in the visible region. It appears that common metals such as gold or silver have plasmon resonances in blue or deep ultra-violet wavelength ranges. Recently, an increased research effort is directed to the infrared. However, when moving from the visible to the infrared range, metal films with arrays of holes that ordinarily show optical transmission are quite opaque. There are no metals available whose plasmon resonances are in the IR range under 10 μm in wavelength. Moreover, the integration of plasmonic structure with active detector region is intrinsically incompatible due to the low-quality metal deposition techniques in comparison with high-quality epitaxial growth of semiconductors or dielectrics. As a result, many intrinsic plasmonic properties can be masked by the poor metal quality or poor semiconductor-metal interfaces. In addition, wavelength tuneability is difficult to realize since the plasmonic resonance frequency is fixed for a given metal. Thus, other alternatives to metals such as highly doped semiconductors have been proposed; e.g., InAs/GaSb bi-layer structure.[32]
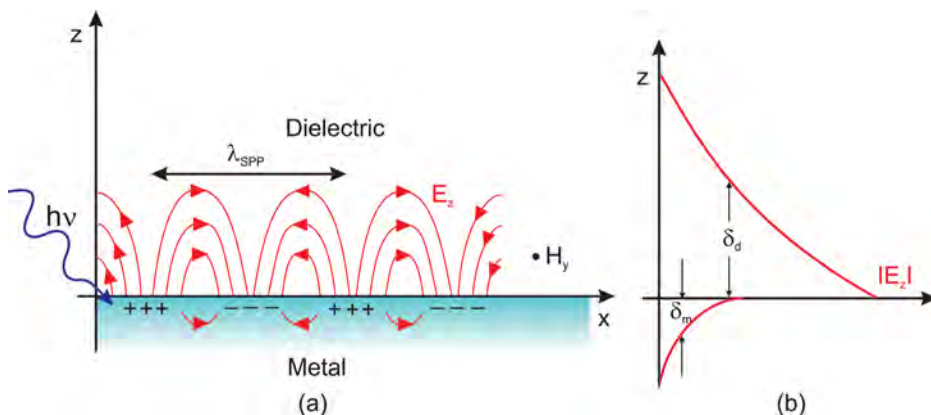

FIG. 14. (a) Schematic illustration of electromagnetic wave and surface charges at the interface between the metal and the dielectric material, and (b) the local electric field component is enhanced near the surface and decays exponentially with distance in a direction normal to the interface.
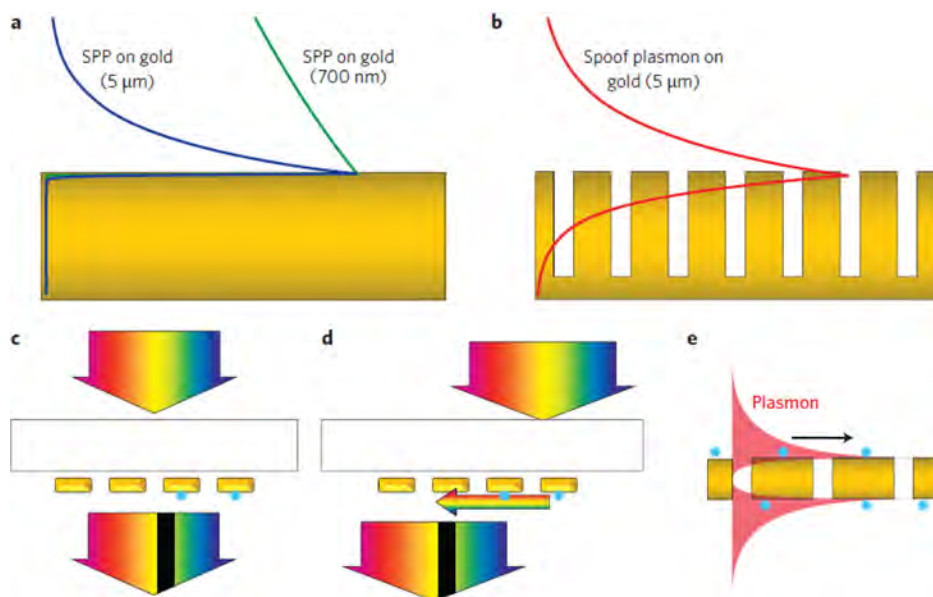
FIG. 15. Optical field of SPs and surface-enhanced infrared absorption. (a) The optical field of a SPP is closely bound to the material surface at visible wavelengths (700 nm, green) but weakly bound at mid-IR wavelengths (5 μm, blue). (b) Optical field of spoof plasmons on gold at a wavelength of 5 μm, showing strong confinement (red). (c) Chemicals (blue stars) on gold islands exhibit better absorption than an unstructured substrate. (d) Using surface plasmons to increase the absorption enhancement. (e) SP-enhanced infrared absorption in a hole array. Plasmons bound to the surface interact with the molecules deposited on and inside the hole array. Reprinted with permission from R. Stanley, Nat. Photonics **6**, 409–411 (2012). Copyright 2012 Macmillan Publishers Ltd.

Figure 15 shows schematically the difference in surface-enhanced between visible and infrared absorption. As shown in Fig. 15(a), the optical field of a SPP is closely bound to the material surface at visible wavelengths but weakly bound at mid-IR wavelengths. Metal surfaces with indentations or holes can give rise to leaky waveguides (spoof plasmonics) or can be used to couple light into dielectric waveguides, what is shown in Fig. 15(b). This solution is used for improving the performance of QWIP and QDIP detectors.[33,34]

Different plasmonic techniques are used to enhance infrared detectors. A technique very popular for THz detectors[35] involves antenna-like structure to couple incident radiation to surface plasmons.[36] Another technique uses a metal grating coupler like that presented in Fig 11. By confining the quantum dots in a waveguide structure and using a metallic grating coupler, a considerable increase in absorption is observed. Very effective alternative approach that is based on a deep sub-wavelength pitch grating in the surface of the metal, as schematically shown in Fig. 15(b).[37] This design leads not only to resonance in the grating but also to extremely tight confinement of light.

Utilizing either a single-metal or a double-metal plasmon waveguide, Rosenberg *et al.*[33] have considered a plasmonic photonic crystal resonator for use in mid-infrared photodetectors. Its good frequency and polarization selectivity can be used in hyperspectral and hyperpolarization detectors. By suitable scaling of the photonic crystal holes and waveguide width, such a resonator can be optimized for use at any wavelength from the terahertz to the visible bands. Figure 16 shows the proposed schematic structure of an FPA with double-metal plasmonic photonic crystal resonators. Only the top metal photonic crystal lithography step differs from standard fabrication process of hybrid arrays.

V. PHOTON TRAPPING DETECTORS

As Eq. (1) indicates, the performance of infrared detector can be improved by reducing volume of detector's active region. In this section, we focus our considerations on reducing the detector material volume via a concept of photon trapping (PT). Reduction of the dark current should be achieved without degrading the quantum efficiency. Figure 17 shows the effect of volume reduction on quantum efficiency and *NETD*[38,39] using a simple first-order model consisting of the Bruggeman effective-medium[40] combining HgCdTe with a composition $x \approx 0.3$ with void material. The fill factor is calculated as the volume of material remaining divided by the volume of the unit cell. As expected, as the volume is reduced (and fill factor is increased), the quantum
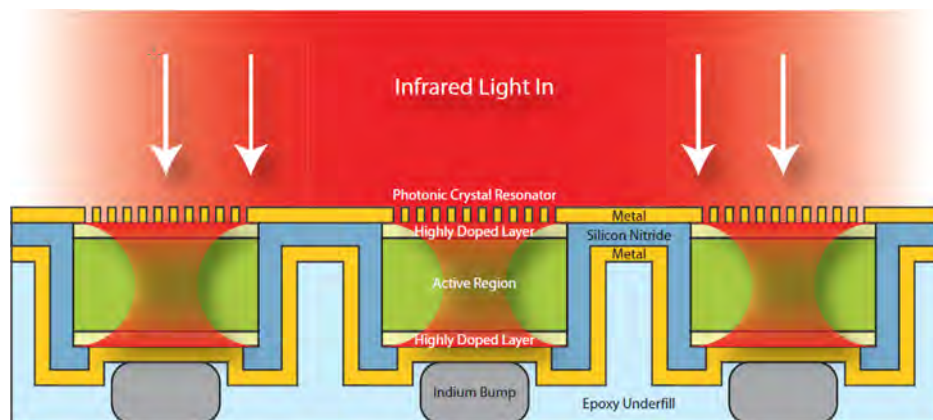

FIG. 16. A design schematic for a resonant double-metal plasmonic photonic crystal FPA. Reproduced with permission from Rosenberg *et al.*, Opt. Express **18**(4), 3672–3686 (2010). Copyright 2010 The Optical Society.
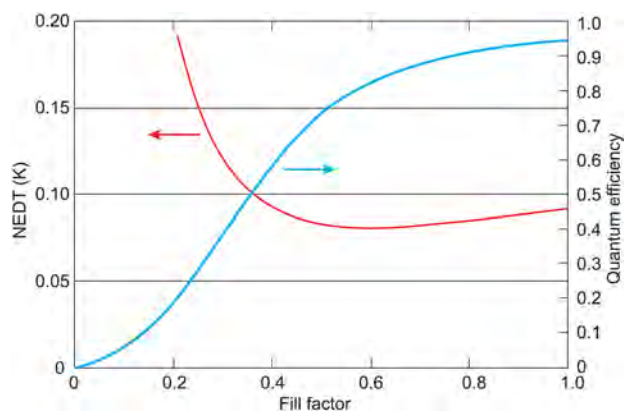
FIG. 17. Effect of volume reduction on quantum efficiency and noise equivalent temperature difference. Reproduced with permission from Smith *et al.*, Proc. SPIE **8353**, 83532R (2012). Copyright 2012 SPIE.

efficiency is increased and the *NETD* value generally decreases improving the performance until a critical point when photon collection begins to decrease faster than noise, and hence, the overall performance degrades. The modeled trends are observed in measured devices.

Photon trapping detectors have been demonstrated independently in II–VI[38,39,41] and III–V[41–44] based epitaxial materials. Sub-wavelength in size semiconductor pillar arrays within a single detector have been designed and structured as an ensemble of 3D photonic structure units using either a top-down or bottom-up process scheme to significantly increase absorption and quantum efficiency. The sub-element architecture can be of different shapes such as pyramidal, sinusoidal, or rectangular.[42] For example, Fig. 18 shows the photon trap structures with pillars and holes of varying volume fill factors. These samples were fabricated from HgCdTe layers on Si grown by MBE with cut-off wavelength of 5 μm at 300 K.

Schuster and Bellotti[45] have simulated numerically the crosstalk in reduced pitch HgCdTe PT structures with 6-μm and 8-μm pixel pitches in a 3 × 3 array as shown in Fig. 19(a)

for an array with 8-μm pixel pitch. The pillars being 5.0-μm tall, 2.0-μm in diameter at the base, and 0.5-μm in diameter just below their tip have nearly sinusoidal profile and are arranged in a square lattice with 2.0-μm sides [see Fig. 19(b)]. Beneath the pillars, there is a 3.0-μm absorbing layer followed by the cap layer.

Theoretical estimates show that the PT arrays have a slightly higher optical crosstalk compared to non-PT arrays, but significantly less diffusion crosstalk, thus indicating that PT arrays will have significantly better device performance than non-PT arrays in terms of crosstalk, especially for small pixel pitches. Moreover, the calculation of the Modulation Transfer Function (MTF) from a spot scan of the arrays shows that PT structures have superior resolving capability compared to non-PT structures. Thus, as the detector array technology moves towards pixels size reduction, the PT approach is an effective means of diffusion crosstalk reduction and an increase of the quantum efficiency without employing antireflection coatings.

Finite-difference time-domain (FDTD) simulation of pillar structures indicates resonance between them (Fig. 20) and confirms the photon trapping process via total internal reflection, effectively serving as a waveguide to direct incident energy away from the removed regions and into the remaining absorber material. For example, Fig. 20 presents the optical generation rate as a function of wavelength from 0.5 μm to 5.0 μm for a single HgCdTe pillar and the uppermost part of the absorber layer beneath the pillars. At wavelength of 0.5 μm, the optical generation is concentrated at the edge of the pillar and as the wavelength is increased the optical generation region gradually extends deeper into the pillars. At 5.0 μm, there is very little of optical generation at the tip of the pillar, but instead, there is significant optical generation further into the pillar and into the absorber layer.

It has been confirmed experimentally that volume reduction leads to improved device performance and, consequently, to higher operating temperature of detector arrays. Process improvements, such as a unique self-aligned contact
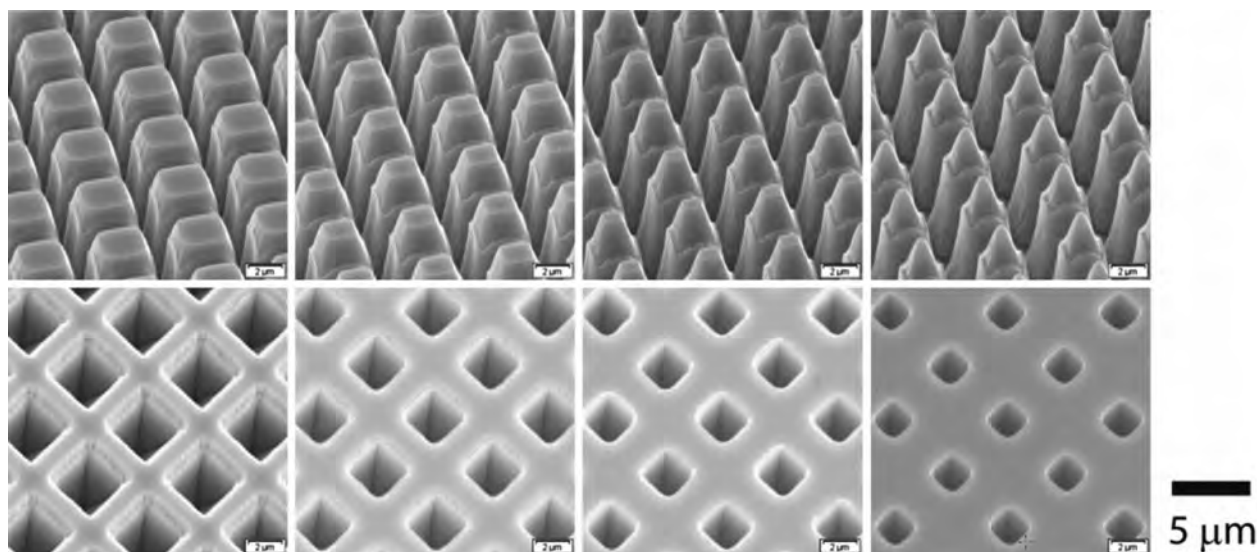

FIG. 18. Examples of photon trapping HgCdTe microstructures with test photonic crystal fields with varying fill factor for FTIR demonstration. Reprinted with permission from Wehner *et al.*, J. Electron. Mater. **40**, 1840–1846 (2011). Copyright 2011 Springer Science and Business Media, Fig. 3.
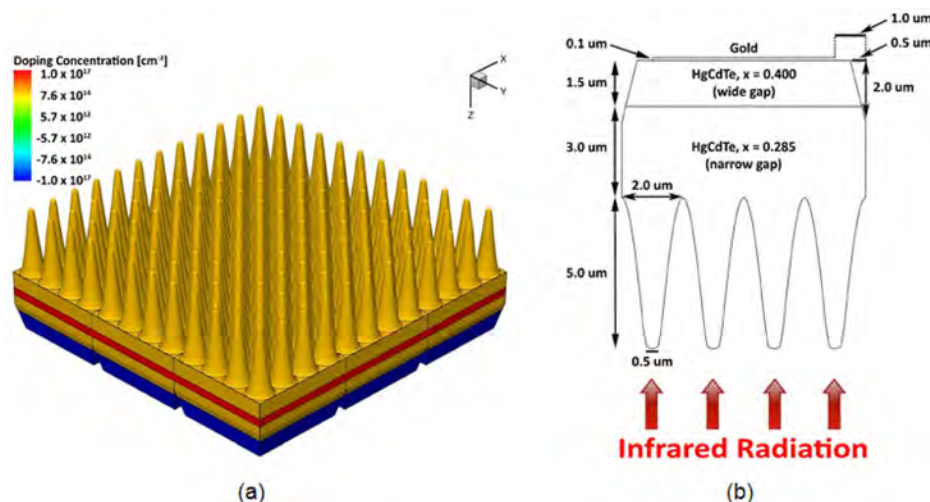
FIG. 19. PT detector array. (a) Three dimensional view of the 3×3 pixel array with 8-μm pixels. (b) Schematic representing the geometry of a single pixel of an HgCdTe array with 8-μm pixels incorporating a PT structure. Reproduced with permission from Opt. Express **21**(12), 14712 (2013). Copyright 2013 The Optical Society.

metal processes and advanced stepper technologies, have been developed to achieve the critical dimensions and lithography alignments required for advanced PT detector designs with a smaller feature within the unit cell. Figure 21 shows advanced hexagonal photonic crystal designs with holes in a standard 30-μm mesa with features on a 5-μm pitch. Large format MBE HgCdTe/Si epitaxial wafer arrays with cut-off wavelengths ranging from 4.3 μm to 5.1 μm at 200 K exhibit improved performance compared to unpatterned mesas, with measured *NETD* of 40 mK and 100 mK at temperatures of 180 K and 200 K, respectively, with good operability.[41]

Utilization of InAsSb absorber on GaAs substrates instead of HgCdTe absorber enables fabrication of MWIR low-cost, large-format HOT FPAs. Souza and co-workers[42–44] have described research efforts in developing visible to mid-wave (0.5 μm to 5.0 μm) broadband PT InAsSb-based

detectors operating at high temperature (150–200 K) with low dark current and high quantum efficiency.

The InAs$_{0.82}$Sb$_{0.18}$ ternary alloy with 5.25-μm cut-off wavelength at 200 K was grown on a lattice-mismatched GaAs substrate. To compare the detector performance, both $128 \times 128/60$-μm as well as $1024 \times 1024/18$-μm detector arrays consisting of bulk absorber structures as well as photon-trap pyramid structures were fabricated. This novel detector design was based on pyramidal PT InAsSb structures in conjunction with barrier-based device architecture to suppress both generation-recombination dark current, as well as the diffusion current through absorber reduced volume. The pixel arrays were defined very simply by etching through the contact layer up to the barrier. Figure 22(a) shows a 5-μm cut-off wavelength nBn detector structure operated at 200 K with AlAsSb barrier and pyramid-shaped

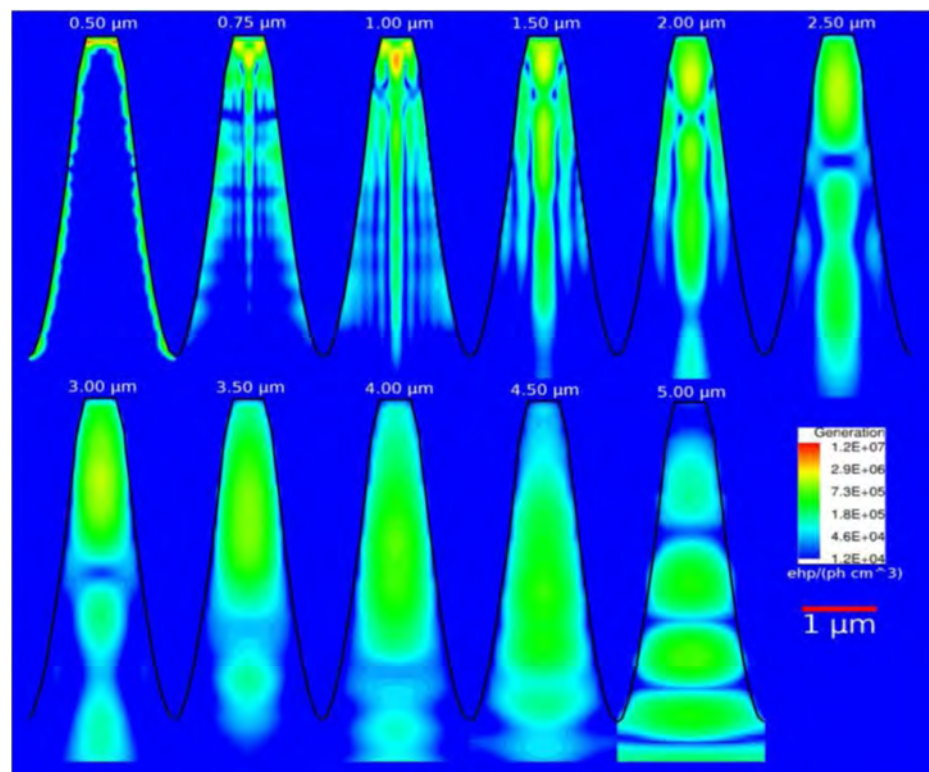FIG. 20. Optical generation profile of a single HgCdTe pillar back-illuminated with planewaves within the wavelength range of 0.5–5.0 μm. Reproduced with permission from J. Schuster and E. Bellotti, Opt. Express **21**(12), 14712 (2013). Copyright 2009 The Optical Society.
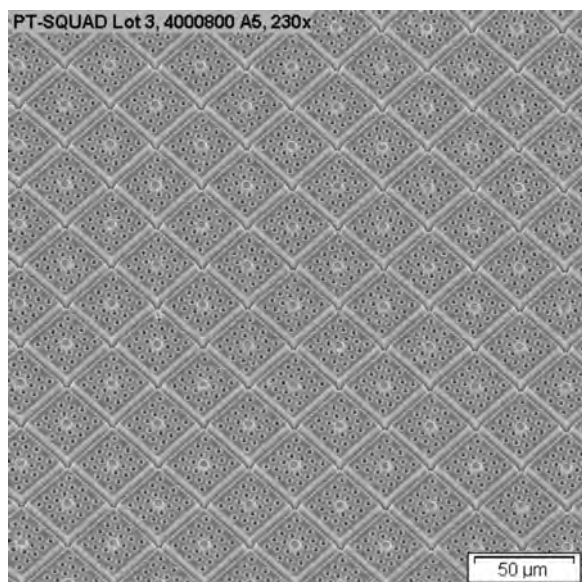
FIG. 21. MWIR 512×512 30-μm pitch MBE HgCdTe/Si array consisting of photonic crystal holes on a 5-μm pitch in a standard mesa. Reproduced with permission from Smith *et al.*, Proc. SPIE **8353**, 83532R (2012). Copyright 2012 SPIE.

absorbers fabricated in the n-type InAsSb absorber. Based on optical simulation, the engineered pyramidal structures minimize the reflection and provide $>90\%$ absorption over the entire 0.5 μm to 5.0 μm spectral range [see Fig. 22(b)] while providing up to $3 \times$ reduction in absorber volume.

The measured dark current density in the pyramidal structured diodes is reduced by a factor of 3 in comparison with conventional diodes with the bulk absorber, which is consistent with volume reduction due to the creation of the absorber topology. High detectivity ($>10^{10}$ cmHz$^{1/2}$/W) and high internal quantum efficiency ($>90\%$) have been achieved over the entire 0.5 μm to 5.0 μm spectral range.

VI. BARRIER INFRARED DETECTORS

Historically, the first barrier detector was proposed by White in 1983[46] as a high impedance photoconductor. It postulates an n-type heterostructure with a narrow gap absorber region coupled to a thin wide bandgap layer, followed by a narrow bandgap contact region. The concept assumes almost zero valence band offset approximation throughout the heterostructure, allowing flow of only minority carriers in a photoconductor. Little or no valence band offset was difficult to realize using standard infrared detector materials such as InSb and HgCdTe. Situation has changed dramatically in the middle of first decade of XXI century after the introduction of 6.1 Å III–V material detector family and when the first high-performance detectors and FPAs were demonstrated.[47,48] Introduction of unipolar barriers in various designs based on T2SLs drastically changed the architecture of infrared detectors.[49] In general, unipolar barriers are used to implement the barrier detector architecture for increasing the collection efficiency of photogenerated carriers and reducing dark current generation without inhibiting photocurrent flow. The ability to tune the positions of the conduction and valence band edges independently in a broken-gap T2SL is especially helpful in the design of unipolar barriers.

The term "unipolar barrier" was coined to describe a barrier that can block one carrier type (electron or hole) but allows an un-impeded flow of the other (see Fig. 23). Between different types of barrier detectors, the most popular is nBn detector shown in Fig. 23. The n-type semiconductor on one side of the barrier constitutes a contact layer for biasing the device, while the n-type narrow-bandgap semiconductor on the other side of the barrier is a photon-absorbing layer whose thickness should be comparable to the absorption length of light in the device, typically several microns. The same doping type in the barrier and active layers is key to maintaining a low, diffusion limited dark current. The barrier needs to be carefully engineered. It must be nearly lattice matched to the surrounding material and have zero offset in the one band and a large offset in the other. It should be located near the minority carrier collector and away from the region of optical absorption. Such barrier arrangement allows photogenerated holes to flow to the contact (cathode) while majority carrier dark current, re-injected photocurrent, and surface current are blocked (see bottom right side of Fig. 23). Effectively, the nBn detector is designed to reduce the dark current (associated with

(a)

(b)

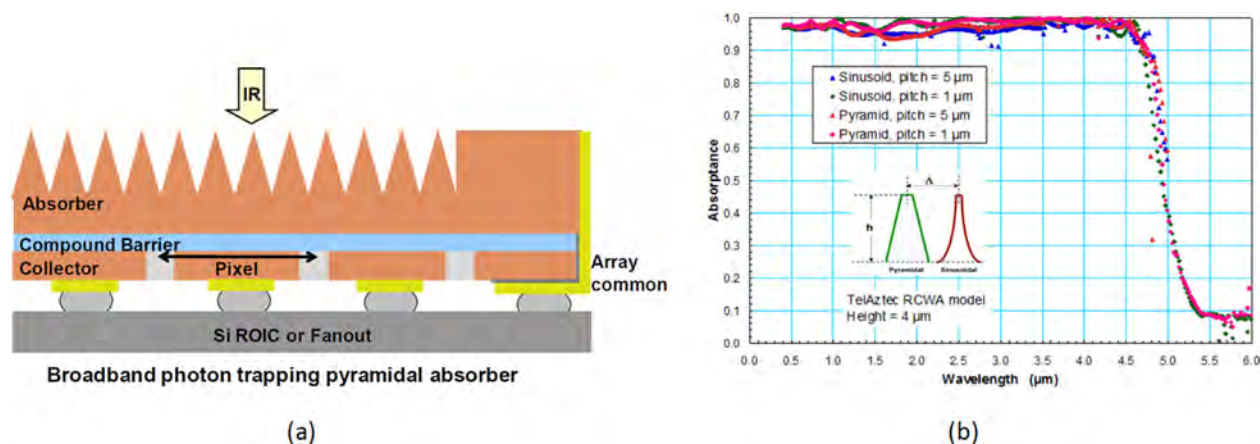FIG. 22. Photon trapping nBn detector in the InAsSb/AlAsSb material system: (a) detector architecture with pyramid shaped absorber layer, (b) optical simulation of broadband detector response. Reproduced with permission from D'Souza *et al.*, Proc. SPIE **8353**, 835333 (2012), Copyright 2012 SPIE and Reproduced with permission from N. K. Dhar and R. Dat Proc. SPIE **8353**, 835302 (2012). Copyright 2012 SPIE.
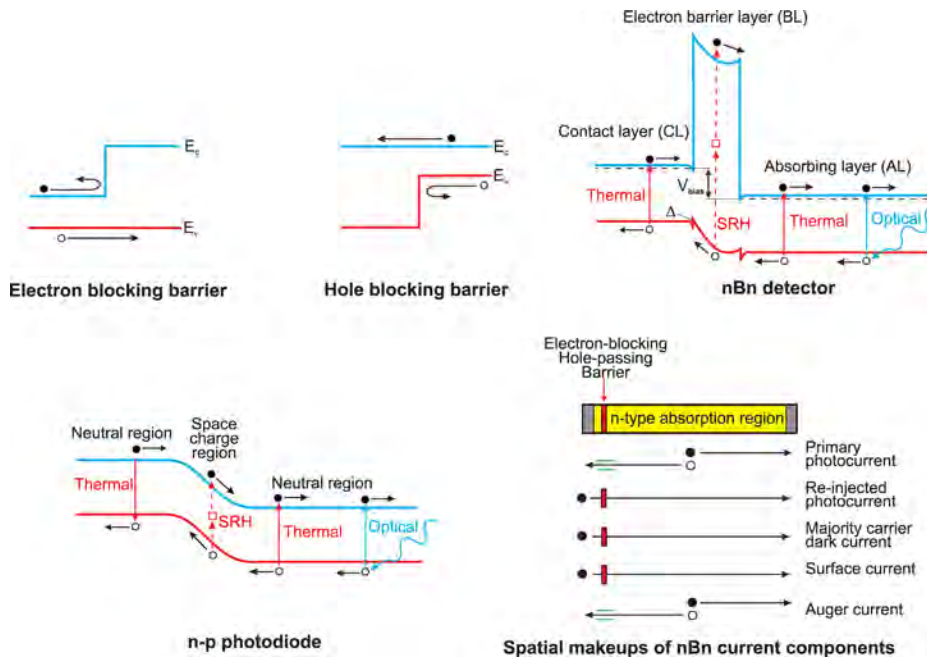
FIG. 23. Illustrations of electron- and hole-blocking unipolar barriers, band gap diagram of nBn barrier detector (the valence-band offset, Δ, is shown explicitly) and p-n photodiode. Bottom right side of nBn barrier detector shows spatial makeups of the various current components and barrier blocking. Reprinted with permission from Savich *et al.*, Infrared Phys. Technol., **59**, 152–155 (2013), Copyright 2013 Elsevier.

Shockley-Read-Hall (SRH) processes) and noise without impeding the photocurrent (signal). In particular, the barrier serves to reduce the surface leakage current. Spatial makeups of the various current components and barrier blocking in nBn detector are shown in the bottom right side of Fig. 23.[50]

The nBn detector is essentially a photoconductor with unity gain, due to the absence of majority carrier flow, and in this respect is similar to a photodiode–the junction (space charge region) is replaced by an electron blocking unipolar barrier (B), and that the p-contact is replaced by an n-contact. It can be stated that the nBn design is a hybrid between photoconductor and photodiode.

Figure 24 shows a typical Arrhenius plot of the dark current in a conventional diode and in an nBn detector. The diffusion current typically varies as $T^3\exp(-E_{g0}/kT)$, where E_{g0} is the band gap extrapolated to zero temperature, T is the temperature, and k is Boltzman's constant. The generation-recombination current varies as $T^{3/2}\exp(-E_{g0}/2kT)$ and is dominated by the generation of electrons and holes by SRH traps in the depletion region. Because in an nBn detector there is no depletion region, the generation-recombination contribution to the dark current from the photon-absorbing layer is totally suppressed. The lower portion of Arrhenius plot for the standard photodiode has a slope that is roughly half that of the upper portion. The solid line (nBn) is an extension of the high temperature diffusion limited region to temperatures below T_c, which is defined as the crossover temperature at which the diffusion and generation-recombination currents are equal. In low-temperature region, the nBn detector offers two important advantages. First, it should exhibit a higher signal-to-noise ratio than a conventional diode operating at the same temperature. Second, it will operate at a higher temperature than a conventional diode with the same dark current. The latter is depicted by the horizontal green-dashed line in Fig. 24.

Absence of a depletion region offers a way for materials with relatively poor SRH lifetimes, such as all III–V compounds, to overcome the disadvantage of large depletion dark currents.

The operating principles of the nBn and related detectors have been described in detail in the literature.[48–55] While the idea of nBn design has originated with bulk InAs materials,[48] its demonstration using T2SL-based materials facilitates the experimental realization of the barrier detector concept with better control of band edge alignments.[56]

Klipstein *et al.*[57] have considered a wide family of barrier detectors, which they divide into two groups: XB_nn and XB_pp detectors (see Fig. 25). In the case of the former group, all designs have the same n-type B_nn structural unit, but use different contact layers (X), in which either the doping, material, or both are varied. If we take, e.g., C_pB_nn and nB_nn
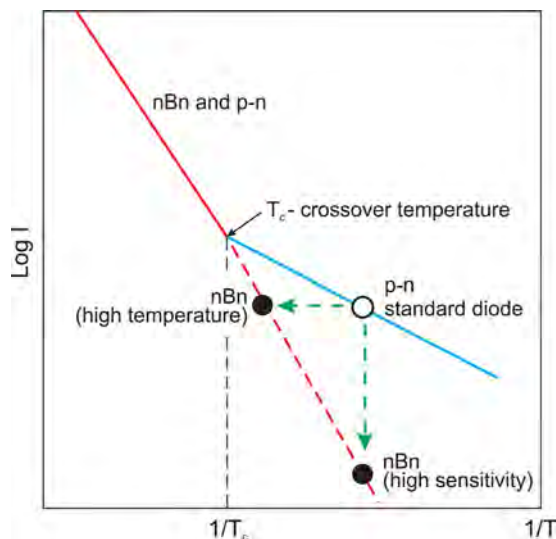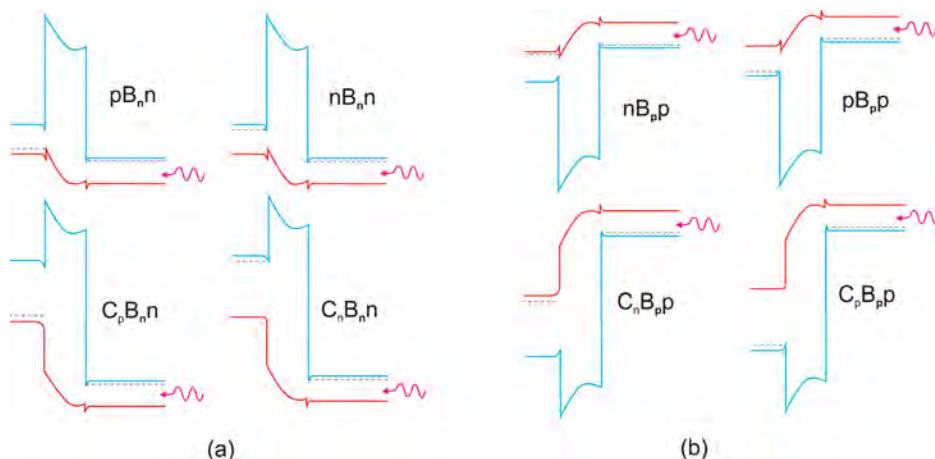

FIG. 24. A schematic Arrhenius plot of the dark current in a standard diode and in an nBn device. Reproduced with permission from Klipstein *et al.*, Opt. Eng. **50**, 061002 (2011). Copyright 2011 SPIE.

FIG. 25. Schematic band profile configurations under operating bias for XB_nn (a) and XB_pp (b) barrier detector families. In each case, the contact layer (X) is on the left, and infrared radiation is incident onto the active layer on the right. When X is composed of the same material as the active layer, both layers have the same symbol (denoting the doping type), otherwise it is denoted as C (with the doping type as a subscript). Reproduced with permission from Klipstein *et al.*, SPIE Newsroom, 2011. Copyright 2011 SPIE.

devices, C_p is the p-type contact made from a different material than the active layer, whereas n is n-type contact made from the same material as the active leyer. In the case of a pB_nn structure, the p-n junction can be located at the interface between the heavily doped p-type material and the lower-doped barrier, or within the lower-doped barrier itself. Our barrier detector family also has p-type members, designated as XB_pp, which are polarity-reversed versions of the n-type detectors. The pBp architecture should be employed when the surface conduction of the materials is p-type and must be used with p-type absorbing layer. This structure can be realized using, e.g., a p-type InAs/GaSb T2SLs as the absorbing layer.[58,59] In addition, the called pMp device consists of two p-doped superlattice active regions and a thin M-structure with higher energy barrier. The band gap difference between superlattice M structure falls in the valence band, creating a valence band barrier for the majority holes in the p-type semiconductor.

Unipolar barriers can also be inserted into a conventional p-n photodiode architecture.[50,60] There are two possible locations into which a unipolar barrier can be implemented: (i) outside of depletion layer in the p-type layer or (ii) near the junction, but at the edge of the n-type absorbing layer (see Fig. 26). Depending on the barrier placement, different dark current components are filtered. For example, placing the barrier in the p-type layer blocks surface current, but currents due to diffusion, generation-recombination, trap-assisted tunneling (TAT), and band-to-band tunneling (BBT) cannot be blocked. If the barrier is placed in the n-type region, the junction generated currents and surface currents are effectively filtered out. The photocurrent shares the same spatial makeup as the diffusion current, what is shown in Fig. 27.

Unipolar barriers can significantly improve the performance of infrared photodiodes, as is shown in Fig. 28 for InAs material system. For InAs, $AlAs_{0.18}Sb_{0.82}$ is an ideal electron blocking unipolar barrier material. Theoretical predictions suggests that the valence band offset (VBO) should be less than k_BT for $AlAs_ySb_{1-y}$ barrier composition in the range of $0.14 < y < 0.18$. Figure 28 compares the temperature dependent R_0A product data for an n-side unipolar barrier photodiode with that of a conventional p-n photodiode. The unipolar barrier photodiode shows performance near Rule 07 with activation energy near the bandgap of InAs indicating diffusion limited performance and six orders of magnitude higher R_0A value in low temperature range than that of conventional p-n junction.

A. Material considerations for barrier infrared detectors

The barrier detector can be implemented in different semiconductor materials. Its practical application has been demonstrated in InAs,[48,50,60] InAsSb,[51,53,57,61,62] InAs/GaSb T2SLs,[49,52,58,59] and recently, also in HgCdTe ternary alloy.[63,64]

The main requirement which must be met to construct the barrier detector structure is "zero" band offset in proper
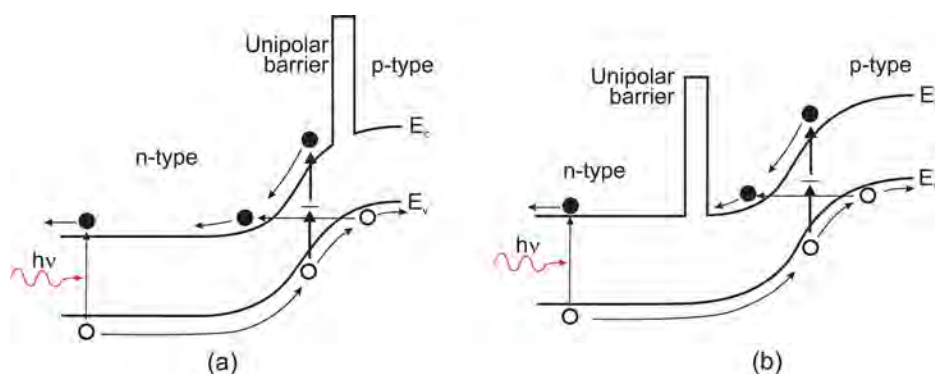

FIG. 26. Band diagrams of a p-side (a) and an n-side (b) unipolar photodiode under bias. Reprinted with permission from Savich *et al.*, Infrared Phys. Technol., **59**, 152–155 (2013). Copyright 2013 Elsevier.
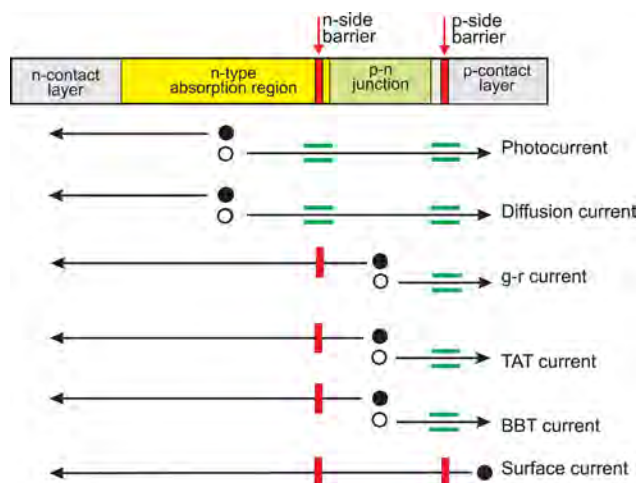
FIG. 27. Placing the barrier in a unipolar barrier photodiode results in the filtering of surface currents and junction related currents. Diffusion current is not filtered because it shares the same spatial makeup as the photocurrent. Reprinted with permission from Savich *et al.*, Infrared Phys. Technol., **59**, 152–155 (2013). Copyright 2013 Elsevier.

FIG. 28. R_0A product of a conventional InAs photodiode and a comparable n-side barrier photodiode. Reprinted with permission from Savich *et al.*, Infrared Phys. Technol., **59**, 152–155 (2013). Copyright 2013 Elsevier.

band correlated to the carrier type which is to be blocked. For material systems where a large conduction band offset is not achievable, the pBn architecture may be preferable. The traditional nBn structure requires biased device operation. For applications where zero bias operation is crucial, again pBn architecture may be used.[65] The large band offset requirement in one band and zero offset in the other is not the only requirement for fabrication of barrier detectors; the lattice matching between surrounding materials is also significant.

Table II lists some physical properties of semiconducting families used for fabrication of infrared photodetectors. All compounds have diamond (D) or zincblende (ZB) crystal structure. Moving across the table from the left to the right, there is a trend in change of chemical bond from the covalent group IV-semiconductors to more ionic II–VI semiconductors with increasing lattice constant. The chemical bonds become weaker, and the materials become softer, what is reflected in the values of the bulk modulus. The materials with larger contribution of covalent bond are mechanically more robust, which leads to better manufacturability. This is evidenced in the dominant position of silicon within electronic materials and GaAs in optoelectronics materials. On the other hand, the band gap energy of semiconductors on the right side of the table tends to have smaller values. Due to their direct band gap structure, strong band-to-band absorption leading to high quantum efficiency is observed (e.g., in InSb and HgCdTe).

Currently, among the materials used in fabrication of barrier detectors, 6.1 Å III–V family plays decisive role offering high performance connected with high design flexibility, direct energy gaps and strong optical absorption. This family is formed by three semiconductors of an approximately matched lattice constant of around 6.1 Å: InAs, GaSb, and AlSb form, with the room temperature energy gaps ranging from 0.36 eV (InAs) to 1.61 eV (AlSb).[66] Like other semiconductor alloys, they are of interest principally for their heterostructures, especially combining InAs with
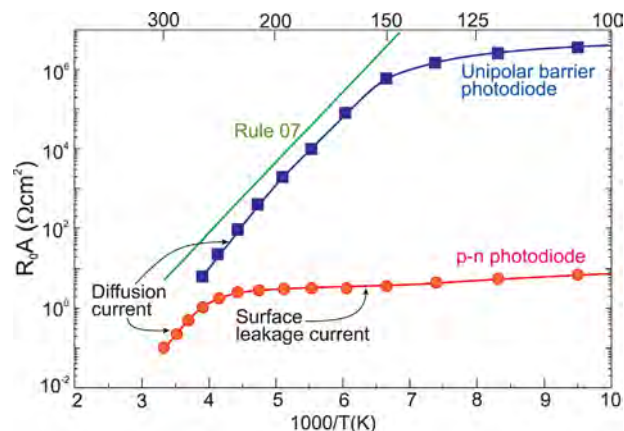
the two antimonides and their alloys. This combination offers a band alignment that is drastically different from that of the more widely studied AlGaAs system, and it is the flexibility in the band alignment that forms are one of the principal reasons for interest in the 6.1 Å family. The most exotic band alignment is that of InAs/GaSb heterojunctions, which Sakaki *et al.*[67] identified as the broken gap alignment in 1977. At the interface, the bottom of conduction band of InAs is located below the top of the valence band of GaSb by about 150 meV. In such a heterostructure, with partial overlapping of the InAs conduction band with the GaSb-rich solid solution valence band, electrons and holes are spatially separated and localized in self-consistent quantum wells formed on both sides of the heterointerface. This leads to unusual tunneling-assisted radiative recombination transitions and novel transport properties. As illustrated in Fig. 29, with the availability of type-I (nested, or straddling), type-II staggered, and type-II broken gap (misaligned, or type III) band offsets between the GaSb/AlSb, InAs/AlSb, and InAs/GaSb material pairs, respectively, there is considerable flexibility in forming a rich variety of alloys and superlattices.

Basic properties of the artificial material, InAs/GaSb T2SLs, supported by simple theoretical considerations are given by Ting *et al.*[49] Their properties may be superior to those of the HgCdTe alloys and are completely different from those of constituent layers. The staggered band alignment of T2SL shown in Fig. 30(a) creates a situation in which the energy band gap of the superlattice can be adjusted to form either a semimetal (for wide InAs and GaSb layers) or a narrow bandgap semiconductor (for narrow layers) material. The band gap of the SL is determined by the energy difference between the electron miniband E_1 and the first heavy hole state HH_1 at the Brillouin zone centre and can be varied continuously in a range between 0 and about 250 meV. One advantage of using type-II superlattice in LW and VLWIR is the ability to fix one component of the material and vary the other to tune the wavelength. An example of the wide tunability of the SLs shown in Fig. 30(b).[68]

The SL band structure reveals important information about carrier transport properties. E_1 band shows strong dispersion along both the growth (z) and in-plane direction (x),

TABLE II. Selected properties of common families of semiconductors used in fabrication of infrared photodetectors. D–diamond, ZB–zincblende, id–indirect, d–direct, L–light hole, H–heavy hole.

	Si IV	Ge IV	GaAs III–V	AlAs III–V	InP III–V	InGaAs III–V	AlInAs III–V	InAs III–V	GaSb III–V	AlSb III–V	InSb III–V	HgTe II–VI	CdTe II–VI
Lattice constant (Å)/structure	5.431 (D)	5.658 (D)	5.653 (ZB)	5.661 (ZB)	5.870 (ZB)	5.870 (ZB)	5.870 (ZB)	6.058 (ZB)	6.096 (ZB)	6.136 (ZB)	6.479 (ZB)	6.453 (ZB)	6.476 (ZB)
Bulk moduls (Gpa)	98	75	75	74	71	69	66	58	56	55	47	43	42
Band gap (eV)	1.124 (id)	0.660 (id)	1.426 (d)	2.153 (id)	1.350 (d)	0.735 (d)		0.354 (d)	0.730 (d)	1.615 (id)	0.175 (d)	−0.141 (d)	1.475 (d)
Electron effective mass	0.26	0.39	0.067	0.29	0.077	0.041		0.024	0.042	0.14	0.014	0.028	0.090
Hole effective mass	0.19	0.12	0.082(L) 0.45(H)	0.11(L) 0.40(H)	0.12(L) 0.55(H)	0.05(L) 0.60(H)		0.025(L) 0.37(H)	0.4	0.98	0.018(L) 0.4(H)	0.40	0.66
Electron mobility (cm²/Vs)	1450	3900	8500	294	5400	13800		3×10^4	5000	200	8×10^4	26500	1050
Hole mobility (cm²/Vs)	505	1900	400	105	180			500	880	420	800	320	104
Electron saturation velocity (10^7 cm/s)	1.0	0.70	1.0	0.85	1.0			4.0	0.4	0.7	4.0		
Thermal cond. (W/cmK)	1.31	0.31	0.5	0.7	0.7			0.27	0.4	0.7	0.15		0.06
Relative dielectric constant	11.9	16.0	12.8	10.0	12.5			15.1	15.7	12.0	17.9	21	10.2
Substrate	Si, Ge		GaAs		InP			InAs, GaSb			InSb	CdZnTe, GaAs, Si	
MW/LW detection mechanism	Heterojunction internal photoemission		QWIP, QDIP		QWIP			Superlattice (MW/LW) / Bulk (MW) / Band-to-band			Bulk / Band-to-band	Bulk / Band-to-band	
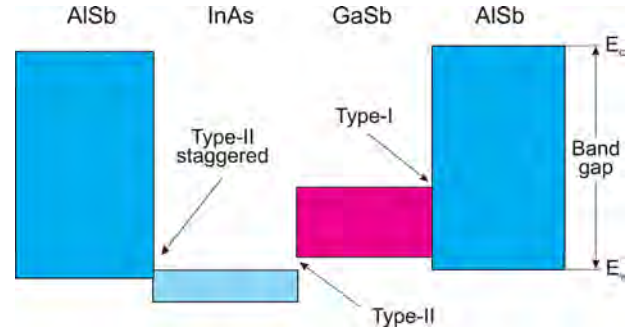
FIG. 29. Schematic illustration of the energy band alignment in the nearly lattice matched InAs/GaSb/AlSb material system. Three types of band alignment are available in this material system: type-I (nested) band alignment between GaSb and AlSb, type-II staggered alignment between InAs and AlSb, and type-II broken gap (or type-III) alignment between InAs and GaSb. Reproduced with permission from Ting *et al.*, Proc. SPIE **7660**, 76601R (2010). Copyright 2010 SPIE.

whereas the HH$_1$ band is highly anisotropic and appears nearly dispersionless along the growth (transport) direction. The electron effective mass along the growth direction is quite small and even slightly smaller than the in-plain electron effective mass. The values estimated by Ting *et al.*[49] for LWIR SL material (22 ML InAs/6 ML GaSb) are as follows: $m_e^{x*} = 0.023 m_0$, $m_e^{z*} = 0.022 m_0$, $m_{hh1}^{x*} = 0.04 m_0$ and $m_{hh1}^{z*} = 1055 m_0$. The SL conduction band structure near the zone centre is approximately isotropic in contrary to the highly anisotropic valence band structure. From this reasons, we would expect very low hole mobility along the growth direction what is unfavorable in detector designs for LWIR FPAs.[69] The estimation of effective masses for MWIR SL material (6 ML InAs/34 ML GaSb) gives: $m_e^{x*} = 0.173 m_0$, $m_e^{z*} = 0.179 m_0$, $m_{hh1}^{x*} = 0.0462$, and $m_{hh1}^{z*} = 6.8 m_0$.[49]

The effective masses are not directly dependent on the band gap energy, as it is the case in a bulk semiconductor. The electron effective mass of InAs/GaSb SL is larger compared to $m_e^* = 0.009 m_0$ in HgCdTe alloy with the same band gap ($E_g \approx 0.1$ eV). Thus, diode tunneling currents in the SL can be reduced compared to the HgCdTe alloy. Although in-plane mobilities drop precipitously for thin wells, electron mobilities approaching 10^4 cm²/Vs have been observed in InAs/GaSb SLs with the layers less than 40 Å thick.

In the T2SL, the electrons are mainly located in the InAs layers, whereas holes are confined to the GaSb layers. This suppresses Auger recombination mechanisms and thereby enhances carrier lifetime. Optical transitions occur spatially indirectly, and, thus, the optical matrix element for such transitions is relatively small. Theoretical analysis of band-to-band Auger and radiative recombination lifetimes for InAs/GaSb SLSs showed that Auger recombination rates are suppressed by several orders of magnitude, compared to those of bulk HgCdTe with similar band-gap. However, the promise of Auger suppression has not been observed yet in practical device material. At present time, the measured carrier lifetime is typically below 100 ns and is limited by SRH mechanism in both MWIR and LWIR compositions. It is interesting to note that InSb, a member of III–V compound family, has had a similar SRH lifetime issue since its inception in 1950 s. Recently, an increase in the minority carrier
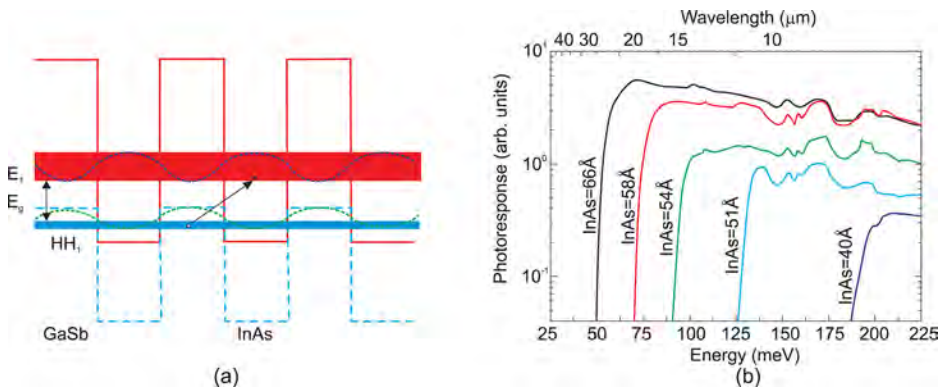
FIG. 30. InAs/GaSb strained layer superlattice: (a) band edge diagram illustrating the confined electron and hole minibands which form the energy bandgap; (b) experimental data of type II SLS cutoff wavelengths change with changing InAs thickness while GaSb is fixed at 40 Å. Reprinted with permission from Y. Wei and M. Razeghi, Phys. Rev. B **69**, 085316 (2004). Copyright 2004 the American Physical Society.

lifetime to 157 ns has been observed due to incorporation of InSb interfacial layer in InAs/GaSb T2SLs.[70]

From the viewpoint of producibility, III–V materials offer much stronger chemical bonds and thus, higher chemical stability compared to HgCdTe. The 6.1 Å materials can be epitaxially grown on GaSb and GaAs substrates. In particular, 4-in. diameter GaSb substrates became commercially available in 2009 offering improved economy of scale for fabrication of large format FPAs arrays.

The most promising materials for barrier detector structures are InAs(InAsSb)/B-AlAsSb and InAs/GaSb T2SLs due to nearly zero VBO with respect to AlAsSb barriers. The InAsSb ternary alloy has a fairly weak dependence of the band edge on the composition and is used in the MWIR region. It was shown that in InAsSb nBn devices, the signal to noise ratio increases as a result of decreasing the valence band offset.[62] The InAs/GaSb T2SLs can be used as mid- or long-wavelength infrared absorber. In particular, the ability to tune the positions of the conduction band and valence band edges independently in the T2SL is especially helpful in the design of unipolar devices. This material system is in an early stage of development. Problems exist in material growth, processing, substrate preparation, and device passivation. Optimization of SL growth is a trade-off between interface roughness and residual background carrier concentrations, where the former requires high growth temperatures and the latter benefit from low temperature growth conditions.

B. MWIR InAsSb barrier detectors

Detailed growth procedures and device characterization of InAsSb/AlAsSb nBn MWIR detectors were the topic of several papers, e.g., Refs. 51, 52, 62, and 71. The n-type doping was usually obtained by either Si or Te elements, and the InAsSb structures were grown on either GaAs(100) or GaSb(100) substrates in a Veeco Gen200 MBE system.[70] The lattice mismatched structures that used GaAs(100) as the substrate were grown on a 4-μm thick GaSb buffer layer, whereas the remaining structures were grown directly onto GaSb(100) substrates. The principal layers of the device structures consisted of a thick n-type InAsSb absorption layer (1.5–3 μm), a thin n-type AlAsSb barrier layer (0.2–0.35 μm), and a thin (0.2–0.3 μm) n-type InAsSb contact layer. The bottom contact layer was highly doped.

Figure 31 shows an example of such an nBn structure that was considered theoretically by Martyniuk and Rogalski,[72] along with the *I-V* characteristics as a function of temperature that were taken from Ref. 44. The alloy composition of $x = 0.09$ for the InAs$_{1-x}$Sb$_x$ absorber layer provided a cutoff wavelength of ~4.9 μm at 150 K. J_{dark} was 10^{-3} A/cm^2 at 200 K and 3×10^{-6} A/cm^2 at 150 K. The detectors are dominated by diffusion currents at -1.0 V bias where the quantum efficiency peaks.

Recently, Klipstein *et al.* have presented one of the first commercial nBn array detectors operating in the blue part of the MWIR atmospheric window (3.4–4.2 μm) that were launched on the market by SCD. It is known as "Kinglet" and is a very low SWaP integrated detector cooler assembly (IDCA) with an aperture of $F/5.5$ and an operating temperature of 150 K. The complete IDCA has a diameter of 28 mm, length of 80 mm, and weight of <300 g; its power consumption is about 3 W at a 60 Hz frame rate [see Fig. 32(a)]. The Kinglet digital detector based on SCD's Pelican-D ROIC
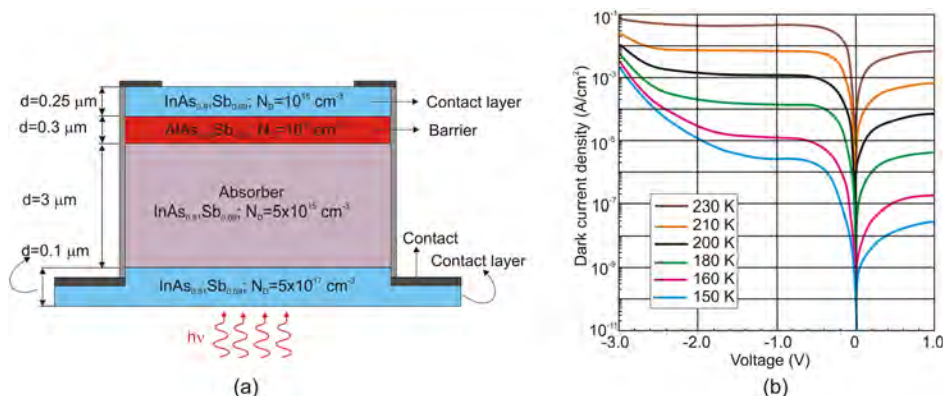

FIG. 31. InAsSb/AlAsSb nBn MWIR detector: (a) the device structure and (b) dark current density vs. bias voltage as a function of temperature for 18 mm pitch detectors ($\lambda_c \approx 4.9\,\mu$m at 150 K) tied together in parallel. Reproduced with permission from Sharifi *et al.*, Proc. SPIE **8704**, 87041U (2013). Copyright 2013 SPIE.
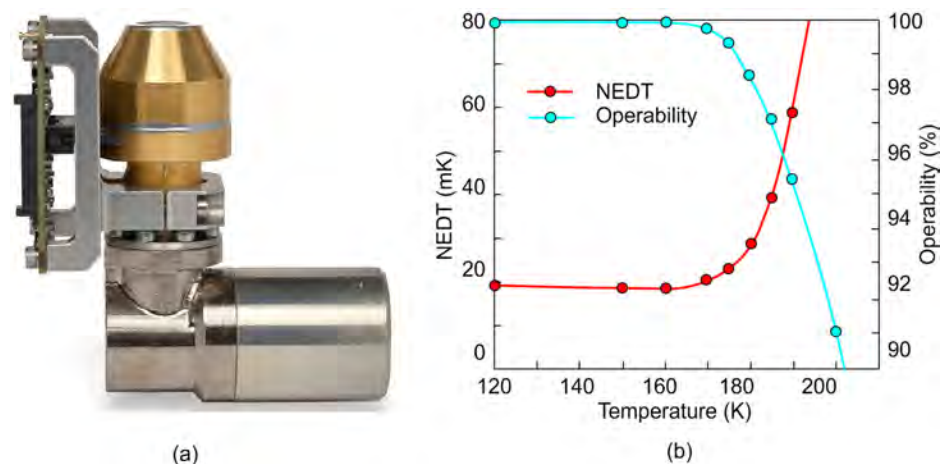
FIG. 32. The Kinglet detector: (a) photograph, and (b) temperature dependence of the *NETD* (at optics *F*/3.2) and the pixel operability. Reproduced with permission from Klipstein *et al.*, Proc. SPIE **8704**, 87041S (2013). Copyright 2013 SPIE.

contains nBn $InAs_{0.91}Sb_{0.09}$/B-AlAsSb 640×512 pixel architecture with a 15-μm pitch. The *NETD* for *F*/3.2 optics and the pixel operability is shown in Fig. 32(b) as a function of temperature. The *NETD* was 20 mK at 22 ms integration time, and the operability of non defective pixels was greater than 99.5% after a standard two point non uniformity correction. The *NETD* and operability begin to change above 170 K, which is consistent with the estimated BLIP temperature of 175 K.

It should be mentioned that recently, a 1280×1024 nBn InAsSb FPA with 12-μm unit cells has been demonstrated by Lockheed Martin Santa Barbara Focal Plane and Teledyne Nova Sensors.

C. T2SL barrier detectors

Building unipolar barriers for InAs/GaSb superlattices is relatively straightforward because of the flexibility of the 6.1 Å III–V material family–InAs, GaSb, and AlSb. For SLs with the same GaSb layer widths, their valence band edges tend to line up very closely due to the large heavy-hole mass. As a result, an electron-blocking unipolar barrier for a given InAs/GaSb SL can be formed by using another InAs/GaSb SL with thinner InAs layers or a GaSb/AlSb SL.

The hole-blocking unipolar barrier can be obtained in different ways using complex supercells, such as the four-layer InAs/GaInSb/InAs/AlGaInSb "W" structure[73] and the four-layer GaSb/InAs/GaSb/AlSb "M" structure.[74] Their designs are shown in Fig. 33. In the "W" structure, two InAs electron-wells are located on either side of an InGaSb hole-well and are bound on either side by AlGaInSb barrier layers. The barriers confine the electron wavefunctions symmetrically about the hole-well, increasing the electron-hole overlap while nearly localizing the wavefunctions. The resulting quasi-dimensional densities of states give strong absorption the near band edge. Due to flexibility in adjusting of the "W" structure, this SL has been used as hole-blocking unipolar barrier, an absorber, as well as an electron-blocking unipolar barrier.

FIG. 33. Schematic energy band diagrams of (a) InAs/GaSb SL, (b) InAs/GaInSb/InAs/AlGaInSb "W" SL, (c) GaSb/InAs/GaSb/AlSb "M" SL, and (d) GaSb/InAs/AlSb "N" SL. From Ting *et al.*, *Type-II Superlattice Infrared Detectors in Semiconductors and Semimetals*. Copyright 2011 Elsevier. Reprinted by permission of Elsevier.

In the "M" structure,[74,75] the wider energy gap AlSb-layer blocks the interaction between electrons in two adjacent InAs wells, thus reducing the tunneling probability and increasing the electron effective mass. The AlSb 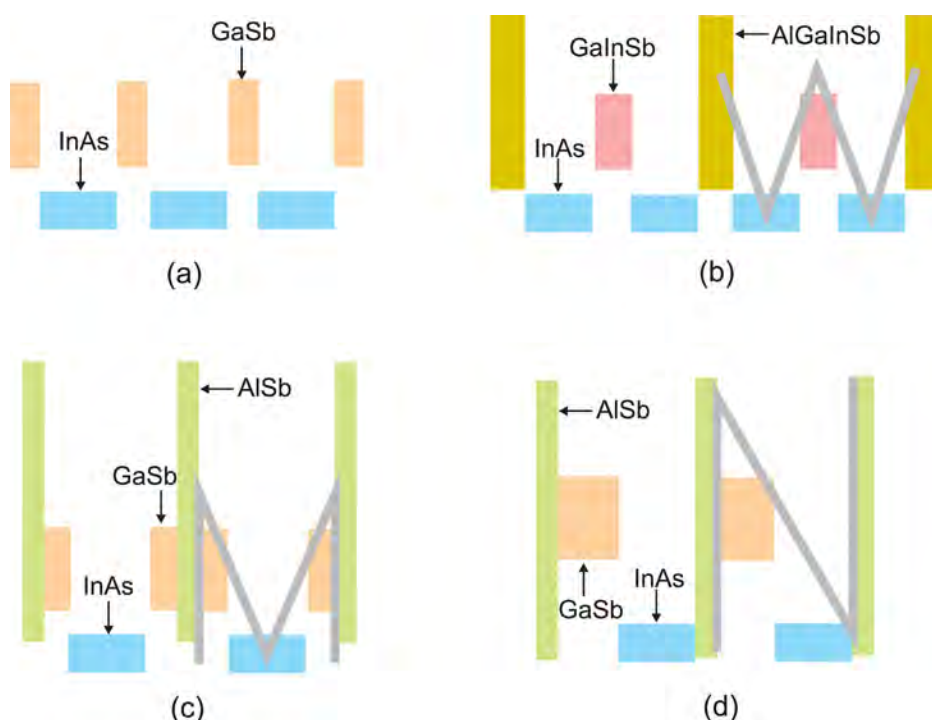layer also acts as a barrier for holes in the valence band and converts the GaSb hole-quantum well into a double quantum well. As a result, the effective well width is reduced, and the hole's energy level becomes sensitive to the well dimension. This structure significantly reduces the dark current and does not show any strong degradation of the optical properties of the devices. Moreover, it has a proven control of positioning of the conduction and valence band energy levels.[76] Consequently, FPAs for imaging within various IR regions, from SWIR to VLWIR, can be fabricated.[77]

In the "N" structure,[78] two monolayers of AlSb are inserted asymmetrically between InAs and GaSb layers, along the growth direction, as an electron barrier. This configuration increases significantly electron-hole overlap under bias, and consequently increases absorption while decreasing the dark current.

Table III illustrates some flat-band energy band diagrams and describes superlattice-based infrared detectors

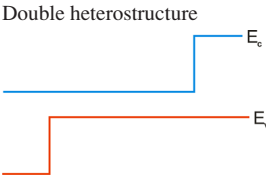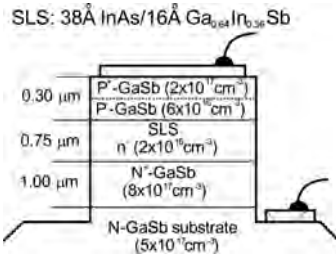TABLE III. Type-II superlattice barrier detectors.
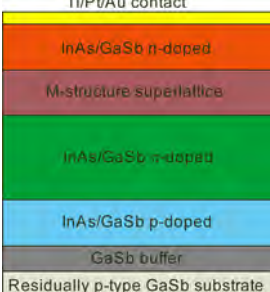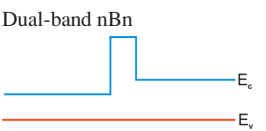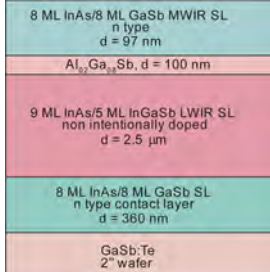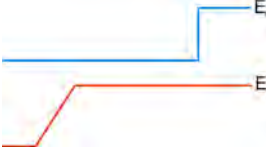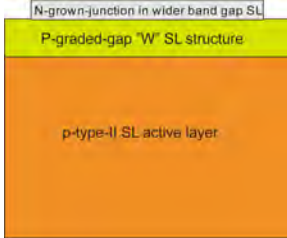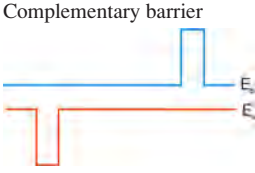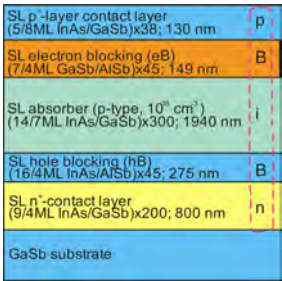
Flat-band energy diagrams	Examples	Description	Refs.
Double heterostructure	SLS: 38Å InAs/16Å Ga$_{0.64}$In$_{0.36}$Sb	**Double heterojunction (DH) photodiode** The first LWIR InAs/InGaSb SL DH photodiode grown on GaSb substrates with photoresponse out to 10.6 μm. The active region consisting of n-type 39 Å InAs/16 Å Ga$_{0.65}$In$_{0.35}$Sb SL (2×10^{16} cm^{-3}) is surrounded by barriers made from p-GaSb and n-GaSb.	79
		p-π-M-n photodiode structure The M structure is inserted between the π and n regions of a typical p-π-n structure. The T2SL part is chosen to have nominally 13 ML InAs and 7 ML GaSb for a cutoff wavelength of around 11 μm. The M structure is designed with 18 ML InAs/3 ML GaSb/5 ML AlSb/3 ML GaSb for a cutoff wavelength of approximately 6 μm. In comparison with standard p-π-n structure, the electric field in depletion region of p-π-M-n structure is reduced and the tunneling barrier between the p and the n regions is spatially broadened. The structure consists of a 250 nm thick GaS:Be p$^+$ buffer (p $\sim 10^{18}$ cm^{-3}), followed by a 500 nm thick InAs/GaSb:Be p$^+$ (p $\sim 10^{18}$ cm^{-3}) superlattice, a 2000 nm thick slightly p-type doped InAs:Be/GaSb region (π-region p $\sim 10^{18}$ cm^{-3}), a M-structure barrier, and a 500 nm thick InAs:Si/GaSb n$^+$ (n $\sim 10^{18}$ cm^{-3}) region, and topped with a thin InAs:Si n$^+$ doped (n $\sim 10^{18}$ cm^{-3}) contact layer.	74–77
Dual-band nBn	8 ML InAs/8 ML GaSb MWIR SL n type d = 97 nm; Al$_{.77}$Ga$_{.23}$Sb, d = 100 nm; 9 ML InAs/5 ML InGaSb LWIR SL non intentionally doped d = 2.5 μm; 8 ML InAs/8 ML GaSb SL n type contact layer d = 360 nm; GaSb:Te 2" wafer	**MWIR/LWIR nBn detector** In this dual-band SL nBn detector, the LWIR SL and MWIR SL are separated by AlGaSb unipolar barrier. The dual band response is achieved by changing the polarity of applied bias (see Fig. 34). The advantage of this structure is design simplicity and compatibility with commercially available readout integrated circuits. The concerns are connected with low hole mobility and lateral diffusion.	80
DH with graded-gap Junction	N-grown-junction in wider band gap SL; P-graded-gap "W" SL structure; p-type-II SL active layer	**Shallow etch mesa isolation (SEMI) structure** It is n-on-p graded-gap "W" photodiode structure in which the energy gap is increased in a series of steps from that of the lightly p-type absorbing region to a value typically two to three times larger. The hole-blocking unipolar barrier is typically made from a four-layer InAs/GaInSb/InAs/AlGaInSb SL. The wider gap levels off about 10 nm short of the doping defined junction, and continues for another 0.25 μm into the heavily n-doped cathode before the structure is terminated by an n$^+$-doped InAs top cap layer. Individual photodiodes are defined using a shallow etch that typically terminates only 10 nm to 20 nm past the junction, which is sufficient to isolate neighboring pixels while leaving the narrow-gap absorber layer buried 100–200 nm below the surface.	83, 84

TABLE III. (*Continued.*)

Flat-band energy diagrams	Examples	Description	Refs.
Complementary barrier		**Complimentary barrier infrared detector (CBIRD)** This device consists of a lightly p-type InAs/GaSb SL absorber sandwiched between an n-type InAs/AlSb hole barrier (hB) SL and wider InAs/GaSb electron barrier (eB). The barriers are designed in a way to have approximately zero conduction and valence band offset with respect to SL absorber. A heavily doped n-type InAsSb layer adjacent to the eB SL acts as the bottom contact layer. The N-p junction between the hB InAs/AlSb SL and the absorber SL reduces SRH-related dark current and trap-assisted tunneling. The LWIR CBIRD superlattice detector performance is close to the "Rule 07" trend line. For a detector having a cutoff wavelength of 9.24 μm, the value of $R_0A > 10^5$ Ωcm^2 at 78 K was measured.	52, 85
		pBiBn detector structure This is another variation of the DH CBIRD structure. In this design a pin photodiode is modified, such that the unipolar electron barrier (eB) and hole barrier (hB) layers, are sandwiched between, respectively; the p-contact layer and the absorber, and the n-contact layer and the absorber. This design facilitates a significant reduction in the electric field drop across the narrow-gap absorber region (most of the electric field drop across the wider bandgap eB and hB layers) leading to a very small depletion region in the absorber layer, and hence reduction in the SRH, band-to-band tunneling and trap-assisted-tunneling current components.	86, 87

that make use of unipolar barriers including: double hetero-structure (DH), dual band nBn structure, DH with graded gap junction and complementary barrier structure. As can be seen, these structures are based on either the nBn/pBp/XBn architecture or different double heterostructure designs.

The first LWIR InAs/InGaSb SL double heterostructure photodiode (see Table III, double heterostructure) grown on GaSb substrates with photoresponse out to 10.6 μm was described by Johnson *et al.* in 1996.[79] In this structure, the active SL region was surrounded by barriers made from p-GaSb and n-GaSb binary compounds. More recently, the barriers are also fabricated using different types of superlattices.

The realization of dual band detection capabilities with nBn design (see Table III, dual-band nBn) is schematically shown in Fig. 34.[49,81] Under forward bias (defined as negative voltage applied to the top contact), the photocarriers are collected from the SL absorber with λ_2 cutoff wavelength. When the device is under reverse bias (defined as positive voltage applied to the top contact), the photocarriers are collected from the SL absorber with λ_1 cutoff wavelength, while those from the absorber with λ_2 cutoff wavelength are blocked by the barrier. Thus, a two-color response is obtained under two different bias polarities.

Hood *et al.*[82] have modified the nBn concept to make the superior pBn LWIR device (see Fig. 25). In this structure, the p-n junction can be located at the interface between the heavily doped p-type contact material and the lower-doped barrier, or within the lower-doped barrier itself. Similar to the nBn structure, the pBn structure still reduces G-R currents associated with SRH centers (the depletion region exists primarily in the barrier and does not

appreciably penetrate the narrow-bandgap n-type absorber). In addition, the electric field in the barrier improves the response of the detector by sweeping from the active layer those photogenerated carriers that reach the barrier before they can recombine.

A variation of the DH detector structure is a structure with graded band gap in the depletion region (see Table III,
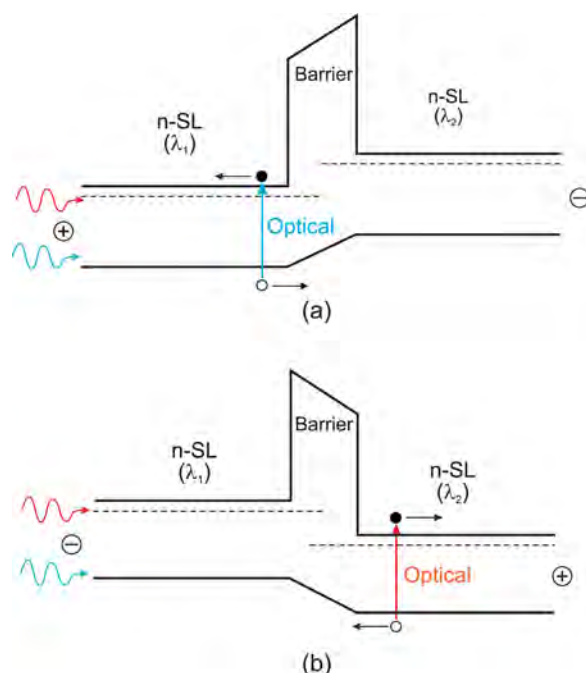

FIG. 34. Schematic band diagram for dual band nBn detector under (a) forward and (b) reverse bias.

DH with graded-gap junction). The graded gap region is inserted between the absorber and the hole barrier to reduce tunneling and generation-recombination processes. A similar structure that was developed by The Naval Research Laboratory and Teledyne enables the shallow-etch mesa isolation (SEMI) structure for surface leakage current reduction. The junction is placed in the wider gap portion of the transition graded gap "W" layer. A shallow mesa etch just through the junction but not into the active layer isolates the diode, but still leaves a wide band gap surface for ease of passivation. A modest reverse bias allows efficient collection from the active layer similar to planar double heterojunction p-on-n HgCdTe photodiodes.[1]

However, the culminating feature is the use of a pair of complementary barriers, namely, an electron barrier and a hole barrier formed at different depths in the growth sequence (see Table III, complementary barrier). Such structure is known as complementary barrier infrared device (CBIRD) and was invented by Ting and others at Jet Propulsion Laboratory. An electron barrier (eB) appears in the conduction band and a hole barrier (hB) in the valence band. The two barriers complement one another to impede the flow of dark current. The absorber region, where the bandgap is smallest, is p-type and the top contact region is n-type, making an n-on-p polarity for the detector element. In sequence from the top, the first three regions are composed of superlattice material: the n-type cap, the p-type absorber, and the p-type eB. The highly doped n-InAsSb layer below the eB is an alloy. Further at the bottom are a GaSb buffer layer and the GaSb substrate.

The introduction of device designs containing unipolar barriers has taken the LWIR CBIRD superlattice detector performance close to the "Rule 07" trend line, which provides a heuristic predictor of the state-of-the-art HgCdTe photodiode performance.[88] The barriers prove to be very effective in suppressing the dark current. Figure 35 compares the *I-V* characteristics of a CBIRD device to a homojunction
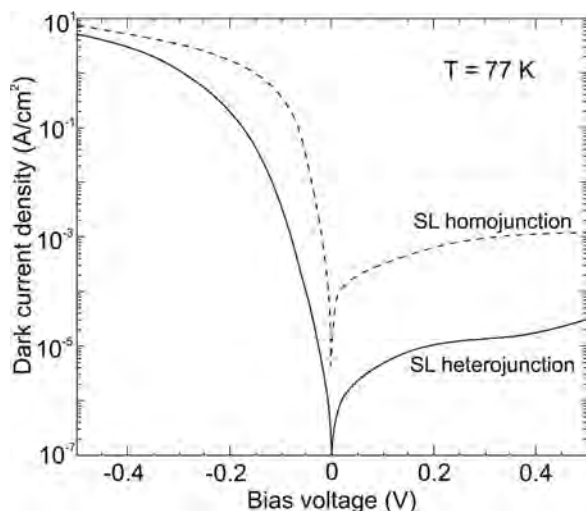
device made with the same absorber superlattice. Lower dark current determines higher *RA* product.

Usually, R_0A values are plotted for devices with near zero-bias turn-on. However, since the detector is expected to operate at a higher bias, a more relevant quantity is the effective resistance-area product. In the case of a detector having a cutoff wavelength of 9.24 μm, the value of $R_0A > 10^5$ Ωcm^2 at 78 K was measured, as compared with about 100 Ωcm^2 for an InAs/GaSb homojunction of the same cutoff. For good photoresponse, the device must be biased to typically -200 mV; the estimated internal quantum efficiency is greater than 50%, while the RA_{eff} remains above 10^4 Ωcm^2.[52]

Rhiger has gathered the 78 K dark current densities versus detector cut-off wavelengths for nonbarrier (homojunction) and barrier (heterojunction) T2SL detectors reported in literature in the period since late 2010 (see Fig. 36).[89] The nonbarrier dark currents are generally higher, with the best approaching Rule 07 to within a factor of about 8. The barrier devices clearly show lower dark currents on average, and some are close to the curve Rule 07.

D. HgCdTe barrier detectors

The nBn architecture has been also implemented into HgCdTe, where technological successful attempts show a prospect for the circumventing of the p-type doping requirements in MBE technology.[90] The HgCdTe nBn devices operating in MWIR range were presented by Itsuno *et al.*[63] and Kopytko *et al.*[64] The HgCdTe ternary alloy is a close to ideal infrared material system. Its position is conditioned by three key features: composition-dependent tailorable energy band gap, large optical coefficients that enable high quantum efficiency, and favorable inherent recombination mechanisms leading to long carrier lifetime and high operating temperature. In addition, extremely small change of lattice constant with composition makes it possible to grow high quality layered heterostructures. However, the existence of valence bands offset in HgCdTe-based nBn detectors creates several issues limiting their performance.[91] Depending on the

FIG. 35. Dark *I-V* characteristics for a LWIR CBIRD detector and a superlattice homojunction at 77 K. From Ting *et al.*, *Type-II Superlattice Infrared Detectors in Semiconductors and Semimetals*. Copyright 2011 Elsevier. Reprinted by permission of Elsevier.

FIG. 36. The 78 K dark current densities plotted against cut-off wavelength for T2SL non-barrier and barrier detectors reported in the literature since late 2010. The solid line indicates the dark current density calculated using the empirical "Rule 07" model. Reprinted with permission from D. R. Rhiger, J. Electron. Mater. **40**, 1815–1822 (2011). Copyright 2011 Springer Science and Business Media, Fig. 8.

FIG. 37. Detector dark current density as a multiple of Rule 07. The black line is drawn as a guide to the eye to show the trend line of dark current reduction with time for single element-detector, and the red line helps to show the trend for FPAs. Reproduced with permission from Zheng *et al.*, Proc. SPIE **7660**, 7660 (2010). Copyright 2010 SPIE.

density as a multiple of Rule 07 versus time. The best SL device is within three times the value of HgCdTe Rule 07. Most of the devices cited here have an absorber thickness of 2–4 μm, which limits its quantum efficiency to less than 40%. At the FPA level, the dark current density is about one order of magnitude higher than that of single-element detectors, and within a factor of 20 of Rule 07.

In the last few years, the first megapixel MWIR and LWIR type-II SL FPAs have been demonstrated with excellent imaging.[59,96–98] At about 78 K, an *NETD* value of below 20 mK has been presented for MWIR arrays and just above 20 mK for LWIR arrays. Figure 38 shows images taken with MWIR 640×512 nBn array and two (MWIR and LWIR) megapixel photovoltaic arrays.

Multicolor capabilities are highly desirable for advanced IR systems since gathering data in discrete IR spectral bands can be used to discriminate for both absolute temperature and unique signatures of objects in the scene. By providing this new dimension of contrast, multiband det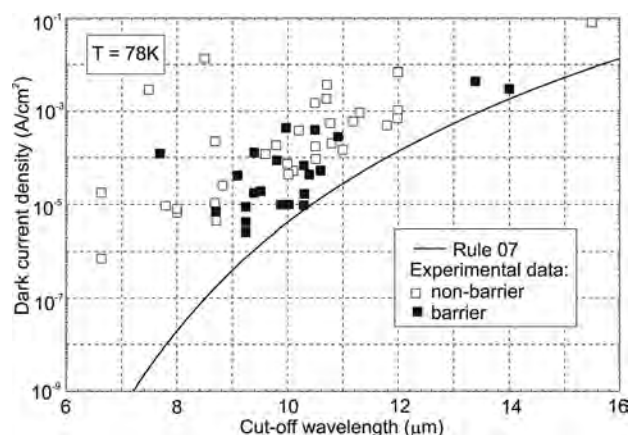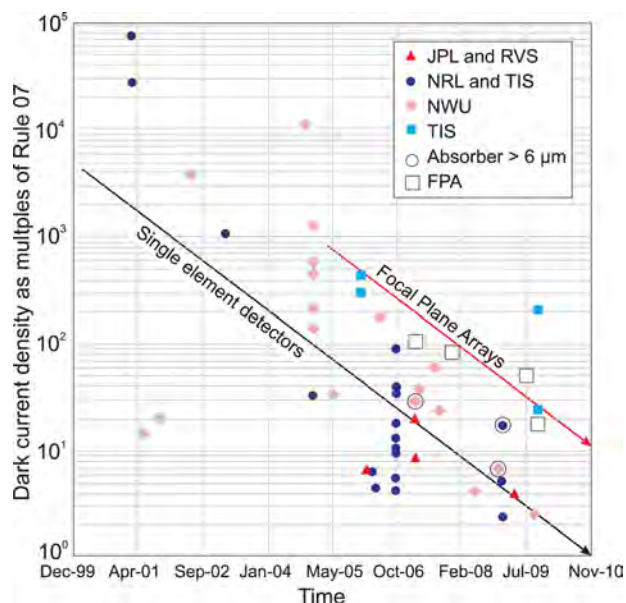ection offers advanced color processing algorithms to further improve sensitivity compared to that of single-color devices. Recent trends in multi-spectral FPA development have leaned towards integrating multi-band functionality into single pixel, rather than combining multiple single-spectral arrays which requires spectral filters and spectrometers.

Apart from HgCdTe photodiodes and QWIPs, T2SL material system has emerged as a candidate suitable for multi-spectral detection due to its ease in bandgap tuning while retaining closely-matched lattice conditions.[99] Three basic approaches to achieve multicolor detection have been proposed: multiple leads, voltage switched, and voltage tuned. They are shortly described in chapter 16 of Rogalski's monograph.[1]

Usually, the unit cell of integrated multicolor FPAs consists of several co-located detectors, each sensitive to a different spectral band (see Fig. 39). Radiation is incident on the shorter band detector, with the longer wave radiation passing through to the next detector. Each layer absorbs radiation up to its cutoff, and hence is transparent to the longer wavelengths, which is then collected in subsequent layers. The device architecture is realized by placing a longer wavelength detector optically behind a shorter wavelength detector.

Research group of the Northwestern University has demonstrated different types of bias-selectable dual-band T2SL FPAs including combination of SW/MW, MW/LW, and LW1/LW2 arrays.[77,100–102] Figure 39(b) presents schematic diagram of a dual-band SW/MW back-to-back p-i-n-n-i-p photodiode structure together with band alignment of superlattices in two absorption layers.

wavelength of operation, a relatively high bias, typically greater than the bandgap energy, is required to be applied to the device in order to collect all of the photogenerated carriers. This leads to strong band-to-band and trap-assisted tunneling due to the high electric field within the depletion layer.

Further strategy in development of HgCdTe nBn detectors should focus on decreasing or even removing the valence band offset in the barrier layer, which will result in lower operating bias, lower dark current, and ability to operate at higher temperatures. Ways to eliminate valence band offset have been proposed[92,93] and have been undertaken for HgCdTe barrier detectors by appropriate bandgap engineering.[94]

E. Imaging arrays

Figure 37 shows tremendous progress made in past few years in the performance of type-II superlattice single element detectors or mini-arrays from USA major institutions: Northwestern University (NWU), Naval Research Laboratory (NRL), Jet Propulsion Laboratory (JPL), and Teledyne Imaging Scientific (TIS).[95] This figure shows superlattice detector performance through measurements of the dark current

FIG. 38. Images taken with (a) an nBn 640×512 MWIR FPA, as well as with megapixel (b) MWIR and (c) LWIR Sb-based photovoltaic FPAs. Reproduced with permission from Hill *et al.*, Proc. SPIE **7298**, 7294 (2009), Copyright 2009 SPIE and reproduced with permission from Soibel *et al.*, Proc. SPIE **8353**, 83530U (2012). Copyright 2012 SPIE.
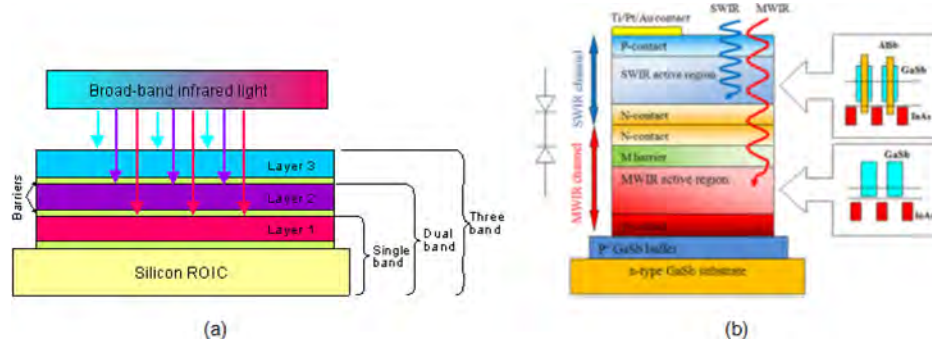
FIG. 39. Multi-color detector pixels: (a) structure of a three-color detector pixel. IR flux from the first band is absorbed in layer 3, while longer wavelength flux is transmitted through to the next layers. Thin barriers separate the absorbing bands. (b) Dual-band SW/MW InAs/GaSb/AlSb T2SL back-to-back p-i-n-n-i-p photodiode structure and schematic band alignment of superlattices in the two absorption layers (dotted lines represent the effective band gaps of superlattices). Reprinted with permission from Appl. Phys. Lett. **102**, 011108 (2013). Copyright 2013 AIP Publishing LLC.

The MW/LW combination uses a back-to-back n-M-π-p-p-π-M-n structure, where MW active region was achieved using 7.5 mono-layers (MLs) of InAs and 10 MLs of GaSb per period with the doping M-barrier. In the LW active region, 13 MLs of InAs and 7 MLs of GaSb were used in superlattice periods. An n-type GaSb semitransparent substrate was mechanically lapped down to a thickness of 30–40 μm and polished to a mirror-like surface. Figure 40(a) shows the detectivity spectrum of both MW and LW channels at 77 K. The *RA* product of LW channel at bias voltage of 0.2 V attained a value close to 600 Ωcm^2. Median *NETD* of ~10 mK and ~30 mK were achieved using 10 ms and 0.18 ms integration times for MW and LW channels, respectively. The obtained images are shown in Fig. 40(b).

F. Barrier detectors vs. HgCdTe photodiodes

The nBn detectors are designed to reduce the dark current associated with SRH processes and to decrease the influence of surface leakage current without impeding the photocurrent (signal). In consequence, absence of a depletion region in barrier detectors offers a way to overcome the disadvantage of large depletion dark currents. So, they are typically implemented in materials with relatively poor SRH lifetimes, such as all III–V compounds.

The band gap structure and physical properties of III–V compounds are found to be remarkably similar to HgCdTe

with the same bandgap. It is interesting to compare the dark currents generated within the detector absorber region composed of III–V and HgCdTe material systems.

The dark diffusion current density generated in the absorber region, J_{dark}, is given by

$$J_{dark} = qGt, \qquad (5)$$

where q is the electron charge, G is the thermal generation rate in the base region, and t is the thickness of active region. Assuming that the thermal generation is a sum of Auger 1 and SRH mechanisms

$$G = \frac{n_i^2}{N_d \tau_{A1}} + \frac{n_i^2}{(N_d + n_i)\tau_{SRH}}, \qquad (6)$$

and that $\tau_{A1} = 2\tau_{A1}^i/[1 + (N_d/n_i)^2]$, the dark current density of n-type absorber region is

$$J_{dark} = \frac{qN_d t}{2\tau_{A1}^i} + \frac{qn_i^2 t}{(N_d + n_i)\tau_{SRH}}. \qquad (7)$$

In the above equations, n_i is the intrinsic carrier concentration, N_d is the absorber doping level, and τ_{A1}^i is the intrinsic Auger 1 lifetime. Eq. (7) shows that the contribution of Auger 1 generation varies as N_d, whereas the SRH generation varies as $1/N_d$. As a result, the minimum dark current density depends on the absorber doping concentration and on
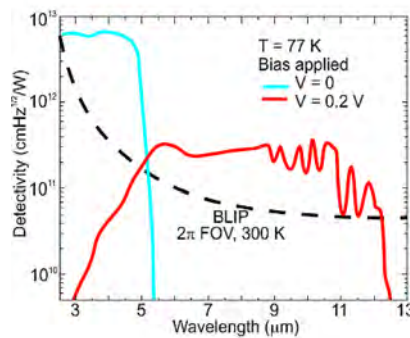
FIG. 40. Bias selectable dual-band MW/LW T2SL array: (a) detectivity spectrum of both MWIR and LWIR channels at 77 K shown with BLIP detectivity limit (2π FOV, 300 K background), (b) MWIR and LWIR channels imaging a 11.3 μm narrow-band pass optical filter at 81 K. Reproduced with permission from Razeghi *et al.*, Proc. SPIE **8704**, 87040S (2013). Copyright 2013 SPIE.

the value of the SRH lifetime. This is demonstrated in Fig. 41. To approach BLIP performance, the detector with 4.8-μm cut-off wavelength operating at 160 K with $F/3$ optics requires a generic IR material SRH lifetime of about 1 μs and optimized absorber doping of $\sim10^{16}$ cm^{-3}. A value of 0.6 μs, relatively independent of temperature, for τ_{SRH} has been suggested in Ref. 65.

Figure 42 compares the predicted dependence of the dark current density on operating temperature for different types of detectors with a 3-μm thick absorber and a cut-off wavelength of 4.8 μm.[103] In comparison with InAsSb photodiode (with built-in depletion region), the benefits of the nBn structure are evident as it allows operation at considerably higher temperatures up to 200 K. However, the HgCdTe photodiode enables higher operating temperatures than the InAsSb nBn detector by $\sim$20 K. The best MWIR III–V devices are heavily doped with Auger lifetime significantly reduced. 300-K data from Bewley *et al.*[104] shows that Auger coefficients for SL devices are 5 to 20 times lower than those for HgCdTe. To attain their full potential, the detector developers need to realize Auger-limited devices at doping levels in the 10^{15} cm^{-3} range. It should be stated that both III–V and HgCdTe MWIR detector architectures fall short of the ultimate performance possible with an $F/3$ optics, namely operation at about 150 K.

Theoretically, LWIR T2SL materials are predicted to have lower fundamental dark currents than HgCdTe [see Fig. 3(b)]; however, their performance has not achieved theoretical values. This limitation appears to be due to two main factors: relatively high background concentrations (about 10^{16} cm^{-3}), and a short minority carrier lifetime (typically tens of nanoseconds). Up until now, non-optimized carrier lifetimes limited by SRH recombination mechanism have been observed. The minority carrier diffusion length is in the range of several micrometers. Improving these fundamental parameters is essential to realize the predicted performance of type-II photodiodes.

FIG. 42. Comparison of the dark current density vs temperature for InAsSb photodiode and nBn detector, as well as an HgCdTe p-on-n photodiode with cut-off wavelength of 4.8 μm.

To date, LWIR T2SL photodiodes perform slightly worse than HgCdTe photodiodes. For example, Fig. 43 compares the predicted dependence of dark current density on operating temperature for InAs/GaSb pBp and HgCdTe photodiode with cut-off wavelength of 10 μm.[103] The BLIP performance with $F/1$ optics for HgCdTe photodiode is achieved at about 130 K, about 15 K higher than for InAs/GaSb pBp detector.

NETD can be determined knowing the dark current density, J_{dark}, the background flux (system optics), ϕ_B, and integration time, τ_{int}, according to relations[105]

$$\text{NETD} = \frac{1 + J_{dark}/J_B}{\sqrt{N}\left(\frac{1}{\phi_B}\frac{d\phi_B}{dT}\right)}, \tag{8}$$

$$J_B = q\eta\phi_B, \tag{9}$$

$$\sqrt{N} = \frac{(J_{dark} + J_B)\tau_{int}}{q}, \tag{10}$$

where N is the well capacity of readout, $J_B = \eta\phi_B A_d$ is the background flux current, and A_d is the detector area.

FIG. 41. Dependence of absorber dark current density on doping concentration for various values of SRH lifetime at an operating temperature of 160 K and a cut-off wavelength of 4.8 μm, operating at an $F/3$ background flux. Reproduced with permission from Kinch *et al.*, Proc. SPIE **7660**, 76602V (2010). Copyright 2010 SPIE.
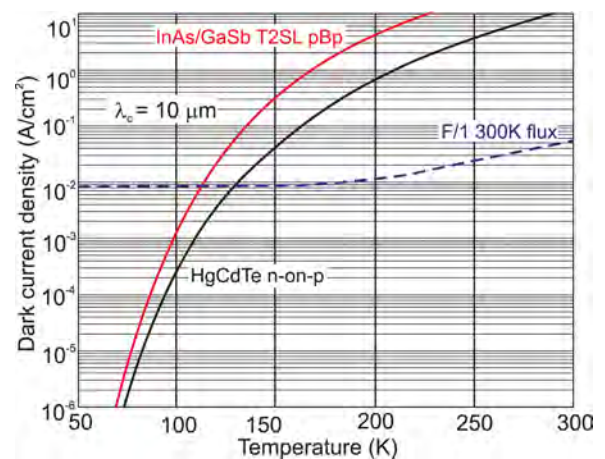
FIG. 43. Comparison of dark current density vs temperature for InAs/GaSb T2SL pBp detector and HgCdTe n-on-p photodiode with cut-off wavelength of 10 μm.
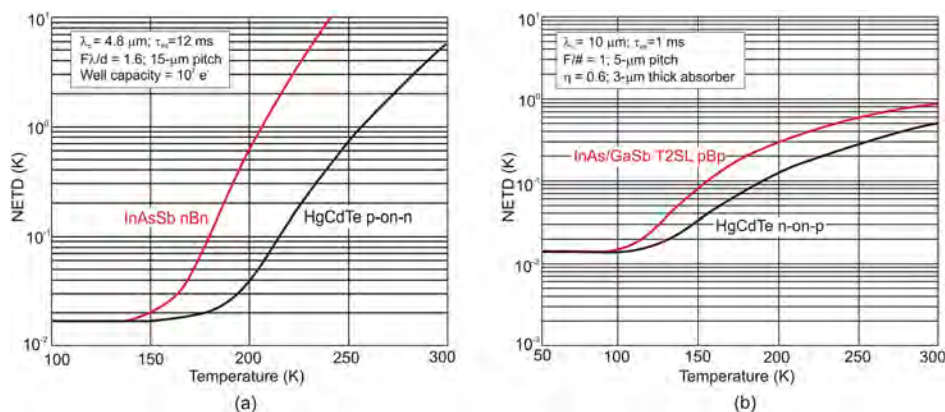
FIG. 44. Temperature dependence of the *NETD* for barrier detectors and HgCdTe photodiodes with cut-off wavelength of (a) 4.8 μm and (b) 10 μm.

Figure 44 shows the temperature dependence of the *NETD* for barrier detectors and HgCdTe photodiodes with cut-off wavelength of 4.8 μm and 10 μm.[103] At the low temperature range, the figure of merit of both material systems provide similar performance because they are predominantly limited by the readout circuits.

Figure 45 compares the performance of optically immersed MWIR photovoltaic HgCdTe detectors with InAsSb, InAs/GaSb T2SLs, and HgCdTe nBn HOT detectors. Properly designed, optically immersed HgCdTe devices (green solid line) approach BLIP limit (for 2π FOV) with thermoelectric (TE) cooling using 2-stage Peltier coolers. In this case, the detectivity is proportional to n^2, where n is the refractive index equal 3.4 for GaAs substrates/lenses. Without optical immersion MWIR HgCdTe photovoltaic detectors are sub-BLIP devices.

The detectivity of nBn T2SLs InAs/GaSb (10 ML/10 ML) and B-Al$_{0.2}$Ga$_{0.8}$Sb is presented for $T = 300$ K. The maximum $D^* = 4 \times 10^8$ cmHz$^{1/2}$/W and quantum efficiency of 15% were estimated.[36] $D^* = 2 \times 10^9$ cmHz$^{1/2}$/W was reported for nBn InAsSb/AlAsSb detectors.[72] nBn and complementary barrier HgCdTe detectors operating in the MWIR range at $T = 200$ K reach detectivity of 6×10^9 and 2×10^{10} cmHz$^{1/2}$/W, respectively.[91]
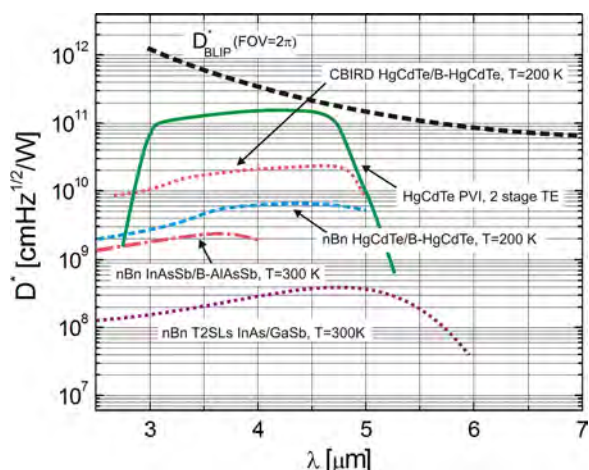
FIG. 45. Comparison of spectral detectivities of optically immersed MWIR photovoltaic HgCdTe detectors and different types of XBn detectors: nBn T2SLs InAs/GaSb and nBn InAsSb/B-AlAsSb operated at $T = 300$ K; nBn HgCdTe/B-HgCdTe and complementary barrier HgCdTe detectors operated at $T = 200$ K.

From the above considerations, it seems that despite numerous advantages of III–V barrier detectors over present-day detection technologies, including reduced tunneling and surface leakage currents, normal-incidence absorption, and suppressed Auger recombination, the promise of superior performance of these detectors has not been realized yet. The dark current density is higher than that of bulk HgCdTe photodiodes, especially in MWIR range. Essential technological limitations need to be overcome in order to attain their full potential. These include short carrier lifetime, passivation, and heterostructure engineering.

VII. MULTI-STAGE INFRARED DETECTORS

In a conventional photodiode, the responsivity and diffusion length are closely coupled and an increase in the absorber thickness much beyond the diffusion length may not result in the desired improvement in signal to noise (S/N) ratio. This effect is particularly pronounced at high temperatures, where diffusions lengths are typically reduce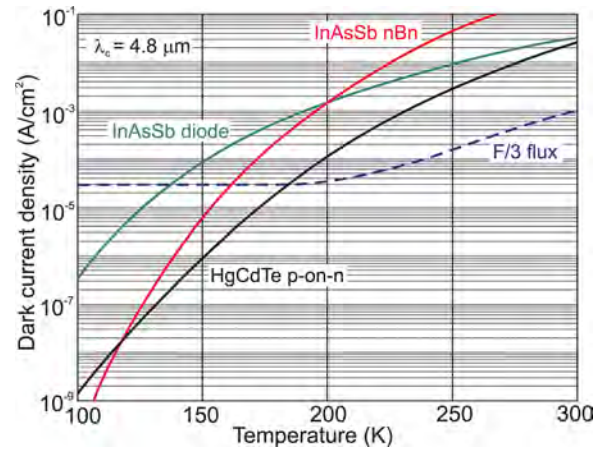d. Only charge carriers that are photogenerated at distance shorter than the diffusion length from junction can be collected. In HOT detectors, the absorption depth of LWIR radiation is longer than the diffusion length. Therefore, only a limited fraction of the photogenerated charge contributes to the quantum efficiency.

To avoid the limitation imposed by the reduced diffusion length and to effectively increase the absorption efficiency, novel detector designs based on multi-stage detection and currently termed as cascade infrared detectors (CIDs) have been introduced in the last decade. CIDs contain multiple discrete absorbers, where each one is shorter or narrower than the diffusion length. In this discrete CID absorber architecture, the individual absorbers are sandwiched between engineered electron and hole barriers to form a series of cascade stages. The photogenerated carriers travel only over one cascade stage before they recombine in the next stage, and every individual cascade stage can be significantly shorter than the diffusion length, while the total thickness of all the absorbers can be comparable or even longer than the diffusion length.

In this case, the S/N ratio and the detectivity will continue to increase with multiple discrete absorbers resulting in improved device performance at elevated temperatures compared to a conventional p-n photodiode. In addition,

flexibility to vary the number and thicknesses of the discrete absorbers result in the ability to tailor the CID designs for optimized performance in meeting specific applications.

Different types of multi-stage IR detectors have been proposed and are now grouped into two main classes: (i) so called intersubband (IS) unipolar quantum cascade IR detectors (QCIDs), and (ii) interband (IB) ambipolar CIDs. Intersubband QCIDs have evolved from the quantum cascade lasers (QCLs) research and have been built for about 15 years.[106–110] A schematic comparison between the band structure of a photoconductive QWIP and a photovoltaic QCID is shown in Fig. 46. The QWIP structure is polarized in order to make the electrons circulate in the external circuit and to record the variation. The active detector region consists of identical QWs separated by thicker barriers. Electrons are excited from the quantum wells by either photoemission (red arrows) or by thermionic emission (black arrows). In contrast, the QCIDs are usually designed to be photovoltaic detectors. They consist of several identical periods made of one active doped well and some other coupled wells. The photoexcited electrons are transported from one active well to the next one by phonon emission through cascaded levels. Figure 46(b) shows the conduction band of one period. Incident photon induces an electron to go from the ground state E_1 to the excited level E_2 which is next transferred to the right hand QWs through longitudinal optical phonon relaxations and finally to the fundamental subband of the next period. The detector period is repeated N times in order to increase the detectivity.

To describe the performance of IS QCIDs, it is convenient to use the formalism originally developed for QWIPs.[111] A theoretical model is presented in, e.g., Refs. 106, 107, and 110.

The detectivity of QCID, including Johnson noise and electrical shot noise components, is determined by[106]

$$D^* = \frac{\eta \lambda q}{hc} \left(\frac{4kT}{Nr_0 A_d} + \frac{2q I_{dark}}{N} \right)^{-1/2}, \tag{11}$$

where $r_0 A_d$ is the resistance at zero bias times the detector area corresponding to one period of QCID, T is the detector temperature, N is the number of periods, and I_{dark} is the dark current. Eq. (11) shows that the signal-to-noise ratio is $\propto \sqrt{N}$.

The promising technology of IS QCDs has been proven in the wavelength range from the near IR to the terahertz (THz) region, and the attained detectivity is presented in Fig. 47. At present, well established semiconductor material systems and processing methods are available. Early QCDs have been demonstrated in the near-IR using InGaAs/AlAsSb, in the mid-IR using InGaAs/InAlAs, and in long-IR up to THz-region using GaAs/AlGaAs materials. These detectors have been cryogenically cooled.[108,109]

A. T2SL interband cascade IR detectors

It has been demonstrated recently that bipolar devices based on type-II InAs/GaSb interband (IB) SL absorbers[112–117] are a good candidate for detectors operating near-room temperature. These interband cascade detectors combine the advantages of interband optical transitions with the excellent carrier transport properties of the interband cascade laser structures. Thermal generation rate at any specific temperature and cut-off wavelength in these devices is usually orders of magnitude smaller than that for corresponding intersubband QCIDs, and devices with good performance have been recently demonstrated.

Hinkley and Yang[116] have shown that multiple-stage architecture is useful for improving the sensitivity of high operating temperature detectors, where the quantum efficiency is limited by short diffusion length. In the case of HgCdTe photodiodes at room temperature, the absorption depth for long wavelength IR radiation ($\lambda > 5\,\mu$m) is longer than the diffusion length. Therefore, only a limited fraction of the photogenerated charge contributes to the quantum

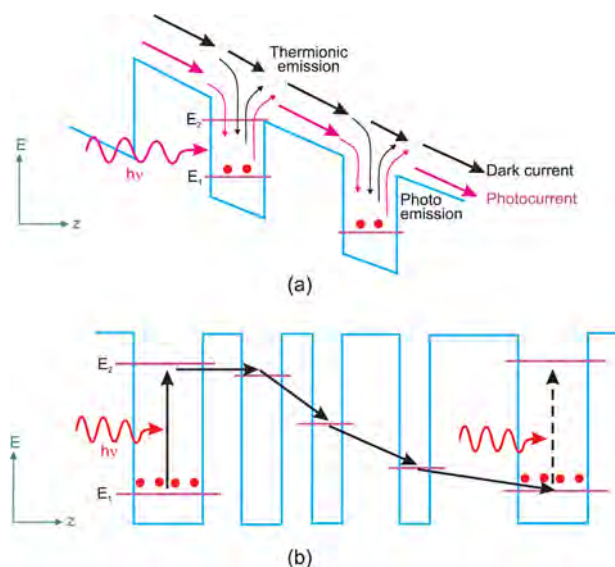FIG. 46. Schematic conduction band diagram of (a) a QWIP and (b) a QCID. In the QWIP, electron transport is accomplished by an external voltage bias whereas an internal potential ramp ensures carrier transport in QCID. Reproduced with permission from Buffaz *et al.*, Proc. SPIE **7660**, 76603Q (2010). Copyright 2010 SPIE.
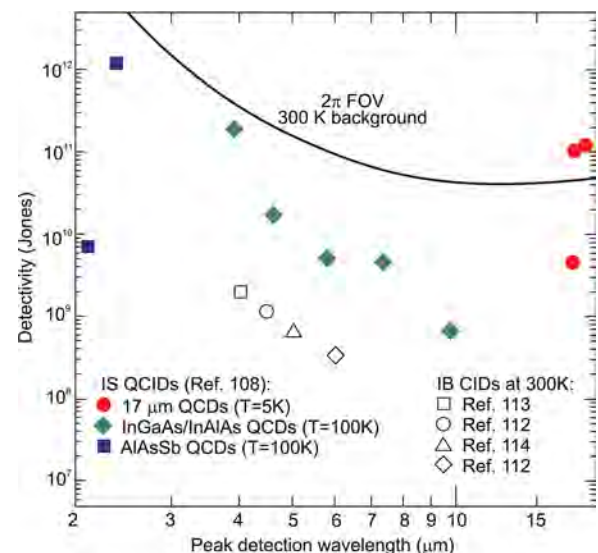

FIG. 47. Detectivity as function of wavelength for different types of CIDs.
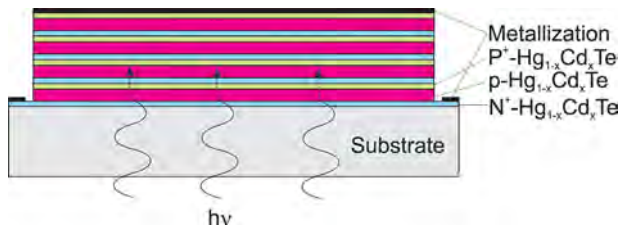
FIG. 48. Backside illuminated 4-cell stacked HgCdTe photovoltaic detector.

efficiency. Calculations considering the example of an uncooled 10.6-μm photodiode show that the ambipolar diffusion length is less than $2\,\mu$m while the absorption depth is $\approx 13\,\mu$m. This reduces the quantum efficiency to $\approx 15\%$ for single pass of radiation through the detector.

Similar situation occurs in the case of HOT T2SL interband cascade IR detectors (IB CIDs). For detector designs where the absorber lengths in each stage are equal, the multiple stage architecture offers the potential for significant detectivity improvement when $\alpha L \leq 0.2$, where α is the absorption coefficient and L is the diffusion length.[116] This theoretical prediction has been confirmed by experimental data as is shown in Fig. 47.

The operation idea of IB cascade photodetectors is similar to that described by Piotrowski and Rogalski (see Fig. 48).[7,118] Earlier attempts to realize this type of devices using HgCdTe were carried out by utilizing tunnel junctions to electrically connect the conduction band of one absorber to the valence band of an adjacent absorber in a way similar to multi-junction solar cells. Each cell is composed of p-type doped narrow gap absorber and heavily doped N^+ and P^+ heterojunction contacts. The incoming radiation is absorbed only in absorber regions, while the heterojunction contacts collect the photogenerated charge carriers. Such devices are capable of achieving high quantum efficiency, large differential resistance and fast response. A practical problem is associated with electrical conductivity through the adjacent N^+ and P^+ layers, however, this is generally overcome by employing tunnel currents through the N^+ and P^+ interface.

The T2SL material system is a natural candidate for realizing multiple-stage IB devices. Figure 49 shows the general design structure for a T2SL cascade detector.[119] Each stage is composed of a *n*-period InAs/GaSb T2SL

sandwiched between an AlSb/GaSb quantum well (QW) electron barrier and an InAs/Al(In)Sb QW hole barrier.

Because the design of IB CIDs is relatively complicated involving many interfaces and strained thin layers, their growth by MBE is challenging. Detector designs exhibit key differences in their approach to construct the relaxation and tunneling regions, as well as the contact layers. As an example, two types of detector designs are shown and shortly described below.

Tian *et al.* have proposed a structure shown schematically in Fig. 50.[113] The detector consists of a 0.5 μm p-type GaSb buffer layer, on which a 7-stage interband cascade structure is grown that uses a finite InAs/GaSb T2SL as the absorber, and finally, a 45-nm-thick n-type InAs the top contact layer. Each cascade stage is composed of a thin InAs/GaSb (7 ML/9 ML) T2SL absorber, where GaSb is sandwiched between the electron relaxation and the interband-tunneling regions that serve also as the hole and the electron barriers, respectively. The barriers act as a means for suppressing leakage current. The electron-relaxation region is designed to facilitate the extraction of photogenerated carriers from the conduction miniband of the absorber and transport them ideally (with little or no resistance) to the valence band of the absorber in the next stage. The energy levels of coupled InAs/AlSb multi-QWs form a staircase, with energy separations comparable to the LO-phonon energy. The uppermost energy level of the relaxation region staircase is close to the conduction miniband in the InAs/GaSb SL, and the bottom energy-level is positioned below the valence-band edge of the adjacent GaSb layer, allowing the interband tunneling of extracted carriers to the next stage. Figure 50(b) shows two channels through which an electron can tunnel through to the next stage: interband tunneling through the type-II broken gap, and intraband tunneling across or thermionic emission over the electron barrier. The enhanced electron barriers suppress intraband-tunneling current between stages and p-type type-II InAs/GaSb superlattice absorbers.

Figure 51 presents the Johnson-noise limited detectivity spectra at various temperatures, extracted from the measured responsivity spectra and R_0A product for the above described detector structure. The dark current density at 50 mV and 300 K is 2.8×10^{-2} A/cm^2, and the extracted R_0A is
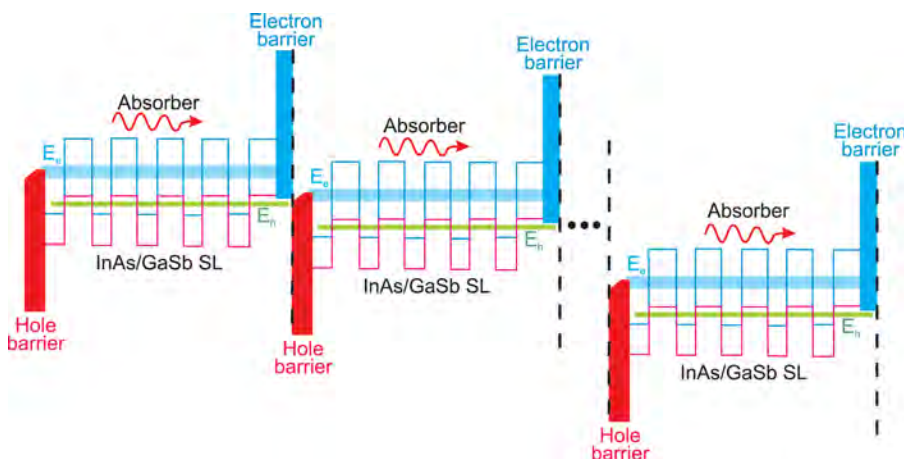
FIG. 49. Schematic illustration of an IB CID device with multiple stages. Each stage is composed of a SL absorber sandwiched between electron and hole barriers. E_e and E_h denote the energy for electron and hole minibands, respectively. The energy difference $(E_e - E_h)$ is the bandgap, E_g, of the SL. Reprinted with permission from Appl. Phys. Lett. **102**, 211103 (2013). Copyright 2013 AIP Publishing LLC.
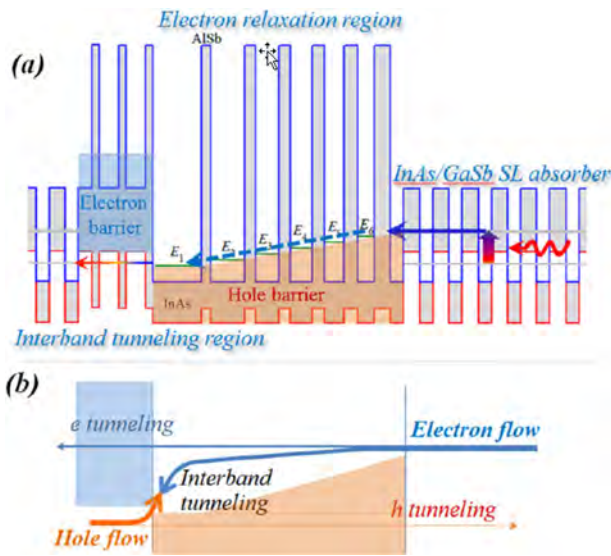
FIG. 50. Schematic illustration of the interband cascade type-II InAs/GaSb superlattice photodetector: (a) photocarrier dynamics, and (b) dark current dynamics. Reprinted with permission from J. Appl. Phys. **111**, 024510 (2012). Copyright 2012 AIP Publishing LLC.

FIG. 51. Johnson-noise limited detectivity spectra of interband cascade type-II InAs/GaSb superlattice photodetector at various temperatures. Reprinted with permission from J. Appl. Phys. **111**, 024510 (2012). Copyright 2012 AIP Publishing LLC.

$1.9 \ \Omega\text{cm}^2$, corresponding to a Johnson-noise limited D^* of 2×10^9 Jones at $4.5 \ \mu\text{m}$.

Modification of the MWIR detector structure has been proposed by Gautam *et al.*[114] A schematic representation of a single stage of the reported cascade detector is shown in Fig. 52(a) and includes (1) the absorber region, (2) the interband tunneling region, and (3) the transport region. Due to built-in electric field, photo-generated electron-hole pairs in the absorber region (1) move in opposite directions: electrons to the right, while the holes to the left. The separation between the quantized energy level in the GaSb QW of region (2) and the valence band in region (1) is designed to be equal to the LO-phonon energy in AlSb (to make the tunneling of holes a phonon-assisted process). The hole and electron barriers represented by the relaxation region (3) and the interband tunneling region (2) also act as the hole and the electron barriers, respectively, and block the flow of dark carriers from one cascade stage into the other.

The heterostructure schematic of the QCD structure is illustrated in Fig. 52(b). It consists of a bottom n$^+$-type InAs/AlSb T2SL contact layer (doped with GaTe to a level of $3 \times 10^{18} \ \text{cm}^{-3}$) followed by seven cascade stages, which precede a 2-nm thick AlSb tunneling barrier, and then the top contact layer (doped at $3 \times 10^{18} \ \text{cm}^{-3}$ with Be). The absorber, non-intentionally doped region, is made from 9ML InAs/9ML GaSb T2SL. The total thickness of the absorber is about $1 \ \mu\text{m}$. The devices were passivated with silicon dioxide.

In the presented design, the total thickness of the absorber is about $1 \ \mu\text{m}$, and theoretically, the absorption quantum efficiency could be increased by increasing the number of stages. However, the conversion quantum efficiency is lower than that of the absorption quantum efficiency by a factor of N.

The dark current density as a function of bias voltage for different temperatures in the range of 225–380 K is shown in Fig. 53(a). Its value at 300 K is about $10^{-2} \ \text{A/cm}^2$ at 5 mV of applied voltage. Since the dark current components scale rapidly with an increase in applied bias, operation

FIG. 52. MWIR T2SL interband cascade detector: (a) a schematic representation of a single stage and (b) a schematic of the detector layered structure. Reprinted with permission from Gautam *et al.*, Infrared Phys. Technol. **59**, 72–77 (2013). Copyright 2013 Elsevier.
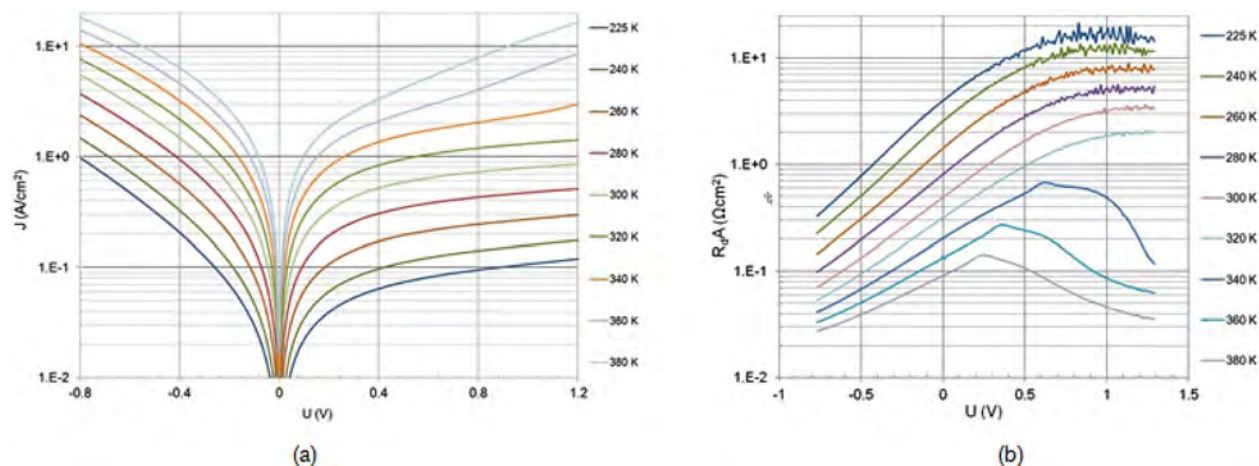
FIG. 53. Dark characteristics of T2SL MWIR cascade detector as a function of bias voltage for different operating temperatures: (a) dark current density and (b) R_dA product. Reproduced with permission from Pusz *et al.*, Proc. SPIE **8868**, 88680M (2013). Copyright 2013 SPIE.

close to zero bias is important for focal plane array high temperature operation. The maximum value of R_dA product exceeds 10 Ωcm^2 for 225 K operation and appears for 0.8–0.9 V bias voltage, and decreases by about two orders of magnitude for 380 K operation with a shift of applied voltage to 0.2 V.

The spectral responsivity of MWIR T2SL cascade detector has been observed up to 380 K. The 100% cut-off wavelength of 6 μm and 7 μm is measured at 225 K and 380 K, respectively (see Fig. 54). At room temperature, for a wavelength $\approx$ 5 μm, the Johnson noise limited detectivity is 3×10^9 Jones. The performance of the device can be further improved by optimizing the doping in the absorber and barrier regions.

Using the equation for spectral responsivity, $R_i = (\lambda \eta / hc)qg$, (where h, c, and g are Planck's constant, speed of light, and photoconductive gain, respectively) and the experimental data gathered in Fig. 54(a), we can estimate room-temperature conversion quantum efficiency at a wavelength of 5 μm, as $\eta g \approx 2.5\%$. Since the device has seven stages, one would estimate a gain of 1/7 (0.14). This leads to the absorption quantum efficiency of 17.5%. The absorption quantum efficiency would

be increased by increasing the number of stages provided that the absorbers are distributed closely in real space and are not very thick, ensuring equal absorption of the photon flux in each of the stages (total thickness of all stages should be comparable to the diffusion length). However, the conversion quantum efficiency remains lower than that of the absorption quantum efficiency by the factor of number of absorbers (stages).

The transport of photoexcited carriers is very fast and occurs over a distance in each cascade stage that is much shorter than a typical diffusion length ($\approx$50–200 nm depending on wavelength). Therefore, the lateral diffusion transport may not be significant over such a short distance, and thus, the deeply etched mesa structures for confining photoexcited carriers may not be necessary in QCDs in contrast to conventional photodiodes. Moreover, significant wave function overlap of energy states in the multiple QW region (relaxation region) causes that the intersubband relaxation time (e.g., optical-phonon scattering time $\approx$ 1 ps) is much shorter than the interband recombination time ($\approx$ 1 ns, or $\approx$ 0.1 ns at high temperatures with significant Auger recombination). Consequently, the photoexcited electrons in the active region
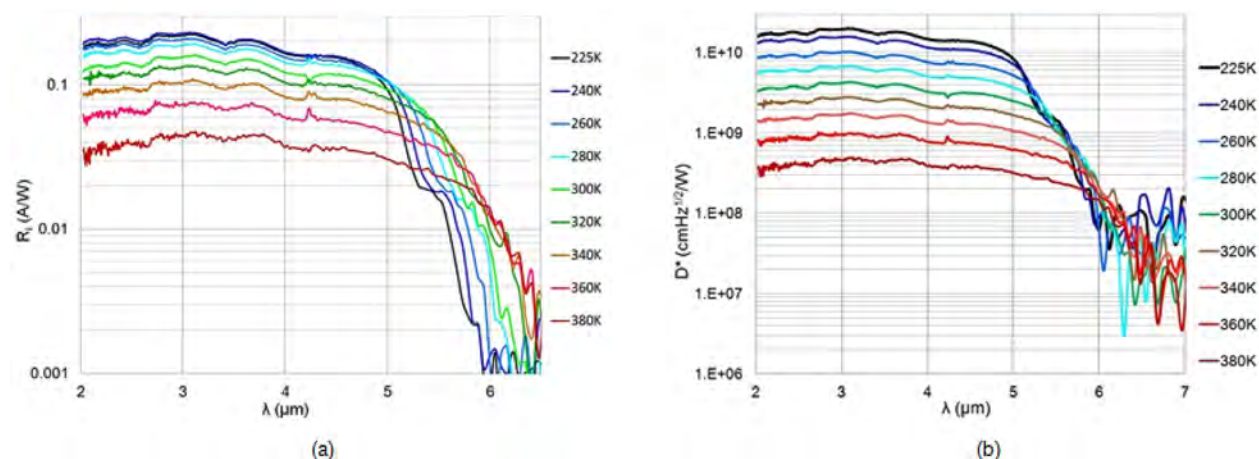
FIG. 54. Spectral characteristics of T2SL MWIR cascade detector: (a) current responsivity and (b) Johnson-noise limited detectivity. Reproduced with permission from Pusz *et al.*, Proc. SPIE **8868**, 88680M (2013). Copyright 2013 SPIE.
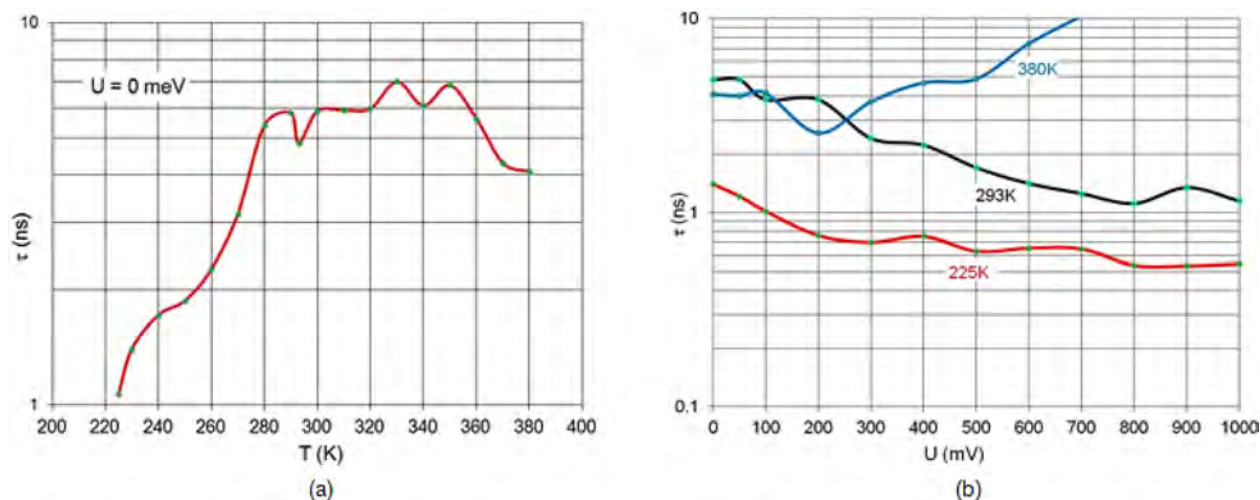
FIG. 55. Response time of T2SL MWIR cascade detector: (a) at zero bias voltage versus temperature and (b) versus negative bias voltage at 225 K, 293 K, and 380 K. Reproduced with permission from Pusz *et al.*, Proc. SPIE **8868**, 88680M (2013). Copyright 2013 SPIE.

are transferred to the bottom of the energy ladder with a very high efficiency. This mechanism enables the quick and efficient removal of carriers after photoexcitation.

Figure 55 presents the experimentally measured response time of a cascade detector versus temperature at zero bias (see Fig. 55(a)) and versus bias voltage for three temperatures of operation: 225 K, 293 K, and 380 K (see Fig. 55(b)). These results confirm short response time of interband cascade detectors. At zero bias, in a temperature range of 225–280 K, the response time increases with increasing temperature from about 1 ns to 5 ns. It stabilizes at about 5 ns for further increase in temperature to about 360 K, when it decreases reaching a value of ~ 2 ns at 380 K.

The negative bias is beneficial for a cascade detector response time (see Fig. 55(b)). The negative correlation between the response time and the applied voltage for temperatures of 225 and 293 K is probably related to drift component decreasing with increasing bias as the electric field increases across the absorber region. In this context, behavior of the response time as a function of bias above a bias of 200 mV for the detector operated at 380 K is not identified to the full extent as the time response raises with increasing voltage. The authors believe that under this condition, the separation between the quantized energy level in the GaSb QW of the tunneling region and the valence band in the transport region does not match the LO-phonon energy in AlSb which is responsible for tunneling of holes by phonon-assisted process. In addition, ambipolar mobility is reduced which in turn influences detector's time response.

Recently, the first 5-stage MWIR interband cascade detector 320×256 focal plane array has been demonstrated with pixel size of 24×24 μm and a pitch size of 30 μm.[120] This device demonstrated BLIP performance above 150 K (300 K, 2π FOV).

B. Performance comparison with HgCdTe HOT photodetectors

At present, HgCdTe is the most widely used variable gap semiconductor for IR photodetectors, including

uncooled operation. However, the junction resistance of HgCdTe photodiodes operated in the long wavelength IR region is very low due to high thermal generation. For example, small sized uncooled 10.6-μm photodiodes $(50 \times 50$ μm$^2)$ exhibit less than 1Ω zero bias junction resistance which is well below the series resistance of a diode. Consequently, the performance of conventional devices is very poor and they are not usable for practical applications.

Figure 56 compares the R_0A product of HgCdTe photodiodes with room-temperature experimental data for interband CIDs fabricated with type-II InAs/GaSb SL absorbers. It is evident that at the present early stage of the CID technology, the experimentally measured R_0A values at room temperature are higher than those for the state-of-the-art HgCdTe photodiodes. However, their quantum efficiencies are low, typically below 10%, resulting in lower detectivity for interband T2SL cascade detectors in comparison to HgCdTe photodiodes.

FIG. 56. R_0A product of HgCdTe photodiodes (solid lines) in comparison with room-temperature experimental data for IB CIDs with type-II InAs/GaSb SL absorbers. Reproduced with permission from Pusz *et al.*, Proc. SPIE **8868**, 88680M (2013). Copyright 2013 SPIE.

FIG. 57. Typical spectral detectivity of HgCdTe detectors with 2-stage TE coolers (solid lines). The best experimental data (white dots) are measured for detectors with FOV equal to 36 degrees. BLIP detectivity is calculated for FOV = 2π. Black dots are measured for detectors with 4-stage TE coolers.

Figure 57 shows the performance of the HgCdTe devices. Without optical immersion MWIR photovoltaic detectors are sub-BLIP devices with performance close to the generation-recombination limit. However, well designed optically immersed devices approach the BLIP limit while thermoelectrically cooled with 2-stage Peltier coolers. Situation is less favorable for >8-μm LWIR photovoltaic detectors, which exhibit detectivities below the BLIP limit by an order of magnitude. Typically, the devices are used at zero bias. The attempts to use Auger suppressed non-equilibrium devices were not successful due to large $1/f$ noise extending to $\approx$100 MHz in extracted photodiode.

Figure 58 gathers the experimentally measured response times of a T2SL interband CID and HgCdTe photodetectors (mainly photodiodes) of different designs and operated in a temperature range between 220 K and room temperature.

FIG. 58. Response time versus wavelength for zero-biased and reverse biased (as indicated) HgCdTe photodiodes and a T2SL MWIR cascade detector operating in the temperature range between 220 and 300 K. "Stacked"–double-stacked photovoltaic detector; PVM-multiple heterojunction photovoltaic detector. Reproduced with permission from Pusz *et al.*, Proc. SPIE **8868**, 88680M (2013). Copyright 2013 SPIE.

Most of the zero-biased LWIR photodiodes are characterized by response times below 10 ns. The device response time decreases under reverse bias achieving value below 1 ns. In this comparison, the response time of T2SL cascade detectors is comparable or even shorter than that of HgCdTe photodetectors.

It is expected that better understanding of the quantum cascade device physics and other aspects related to their design and material properties will enable high performance HOT detectors. In addition, the discrete architecture of QCD provides a great deal of flexibility for manipulating carrier transports to achieve high-speed operation which determines the maximum bandwidth. The possibility of having them monolithically integrated with active components, for instance lasers, offers entirely new avenues for telecommunication systems based on quantum devices.

VIII. CONCLUSIONS

It is predicted that in the IR region, the capabilities of HgCdTe-based technology will continue to expand because of the excellent material properties. Despite serious competition from alternative technologies, HgCdTe is unlikely to be seriously challenged for high-performance applications or applications requiring multispectral capability and fast response. However, the composition non-uniformity is a serious problem in the case of LWIR and VLWIR HgCdTe detectors. For applications that require operation in the LWIR band as well as in two-color MWIR/LWIR/VLWIR bands, HgCdTe, most probably, will not be the optimal solution. The type II InAs/GaInSb superlattice structure is a relatively new alternative for an IR material system and has great potential for LWIR/VLWIR spectral ranges with performance comparable to HgCdTe with the same cutoff wavelengths. The fact that Sb-based superlattice fabrication processing is based on standard III–V technology raises the potential of being more competitive due to lower costs of mass production.

Advances in optoelectronic related materials science, such as metamaterials and nanostructures, have opened doors for new non-classical approaches to device design methodologies improving light coupling with detector active region. In particular, research on plasmonic techniques and on photonic crystal structures has revealed several new ways for the control of light leading to enhancement of IR detector performance.

In the last two decades, several new concepts for improving the performance of photodetectors have been proposed. They are particularly addressing the drive towards the so called HOT detectors aiming to increase detector operating temperatures. New strategies in photodetector designs include barrier detectors, unipolar barrier photodiodes, multistage detectors, and trapping detectors. Some of these solutions have emerged as real competitors to HgCdTe photodetectors. The superior performance of barrier detectors in comparison to conventional p-n junction photodiodes is due to fact that the nBn structure is not limited by generation-recombination and tunneling currents.

Absence of a depletion region in barrier detectors offers a way to overcome the disadvantage of large depletion dark

currents. Consequently, they can be implemented in materials with relatively poor SRH lifetimes, such as all III–V compounds. In addition, one can simultaneously harness the fully developed III–V material technology with its superior uniformity over large area and use bulk materials for HOT detection in MWIR range (e.g. InAsSb ternary alloy). At present time, theoretical predictions place T2SLs InAs/GaSb at the forefront of IR systems development, and these $A^{III}B^{V}$ material systems being grown on the GaAs/GaSb substrates are very promising candidates for future integration with Si technology.

Despite numerous advantages of III–V barrier detectors over present-day detection technologies, the promise of superior performance of these detectors has not materialized to date. In particular, the dark current density is persistently higher than that of bulk HgCdTe photodiodes, especially in the MWIR range. Essential technological limitations need to be overcome in order to attain their full potential. These include short carrier lifetime, passivation, and heterostructure engineering.

Further strategy in development of barrier detectors should be focusing on the decreasing or even removal of the valence band offset in the barrier layer (especially in HgCdTe nBn detectors) what will result in lower operating bias, lower dark current, and ability to operate at higher temperatures. Ways to eliminate valence band offset have been proposed and are being developed for HgCdTe barrier detectors by appropriate bandgap enegineering.

Currently, the only commercially available fast room temperature detectors in the IR range are based on the HgCdTe material. A novel HOT detector design, the so-called interband cascade T2SL detector design, has demonstrated the capability to provide high performance in terms of high detectivity and a response time below 1 ns. The cascade detectors have demonstrated high operating temperatures, up to 400 K, which is not possible to achieve by photodetectors based on the HgCdTe material.

ACKNOWLEDGMENTS

[1] A. Rogalski, *Infrared Detectors*, 2nd ed. (CRC Press, Boca Raton, 2010).

[2] W. D. Lawson, S. Nielson, E. H. Putley, and A. S. Young, "Preparation and properties of HgTe and mixed crystals of HgTe-CdTe," J. Phys. Chem. Solids **9**, 325–329 (1959).

[3] W. S. Boyle and G. E. Smith, "Charge-coupled semiconductor devices," Bell Syst. Tech. J. **49**, 587–593 (1970).

[4] S. Krishna, "The infrared retina," J. Phys. D: Appl. Phys. **42**, 234005 (2009).

[5] S. J. Lee, Z. Ku, A. Barve, J. Montoya, W.-Y. Jang, S. R. J. Brueck, M. Sundaram, A. Reisinger, S. Krishna, and S. K. Noh, "A monolithically integrated plasmonic infrared quantum dot camera," Nat. Commun. **2**, 286 (2011).

[6] J. Piotrowski and A. Rogalski, "Uncooled long wavelength infrared photon detectors," Infrared Phys. Technol. **46**, 115–131 (2004).

[7] J. Piotrowski and A. Rogalski, *High-Operating Temperature Infrared Photodetectors* (SPIE Press, Bellingham, 2007).

[8] J. Piotrowski and A. Piotrowski, "Room temperature IR photodetectors," in *Mercury Cadmium Telluride. Growth, Properties and Applications*, edited by P. Capper and J. Garland (Wiley, West Sussex, 2011), pp. 513–537.

[9] C. T. Elliott and N. T. Gordon, "Infrared detectors," in *Handbook on Semiconductors*, edited by C. Hilsum (North-Holland, Amsterdam, 1993), Vol. 4, pp. 841–936.

[10] C. T. Elliott, "New infrared and other applications of narrow gap semiconductors," Proc. SPIE **3436**, 763–775 (1998).

[11] C. T. Elliott, "Photoconductive and non-equilibrium devices in HgCdTe and related alloys," in *Infrared Detectors and Emitters: Materials and Devices*, edited by P. Capper and C. T. Elliott (Kluwer Academic Publishers, Boston, 2001), pp. 279–312.

[12] J. Piotrowski and A. Rogalski, "Comment on "Temperature limits on infrared detectivities of InAs/In$_x$Ga$_{1-x}$Sb superlltices and bulk Hg$_{1-x}$Cd$_x$Te" [J. Appl. Phys. **74**, 4774 (1993)]," J. Appl. Phys. **80**(4), 2542–2544 (1996).

[13] J. Piotrowski and W. Gawron, "Ultimate performance of infrared photodetectors and figure of merit of detector material," Infrared Phys. Technol. **38**, 63–68 (1997).

[14] A. Rogalski, "Quantum well photoconductors in infrared detectors technology," J. Appl. Phys. **93**, 4355–4391 (2003).

[15] P. Norton, "Detector focal plane array technology," in *Encyclopedia of Optical Engineering*, edited by R. Driggers (Marcel Dekker Inc., New York, 2003), pp. 320–348.

[16] L. Pillans, R. M. Ash, L. Hipwood, and P. Knowles, "MWIR mercury cadmium telluride detectors for high operating temperatures," Proc. SPIE **8353**, 83532W (2012).

[17] C. Li, G. Skidmore, C. Howard, E. Clarke, and C. J. Han, "Advancement in 17 micron pixel pitch uncooled focal plane arrays," Proc. SPIE **7298**, 72980S (2009).

[18] G. Destefanis, P. Tribolet, M. Vuillermet, and D. B. Lanfrey, "MCT IR detectors in France," Proc. SPIE **8012**, 801235 (2011).

[19] See http://www.sofradir-ec.com/wp-uncooled-detectors-achieve.asp for ULIS.

[20] P. B. Catrysse and T. Skauli, "Pixel scaling in infrared focal plane arrays," Appl. Opt. **52**(7), C72–C76 (2013).

[21] W. E. Tennant, "Limits of infrared imaging," Int. J. High Speed Electron. Syst. **20**, 529–539 (2011).

[22] See nird_darpa_baa_08_54_final_for_posting_28aug08.pdf for the link to the description of the Darpa Nyquist-Limited Infrared Detectors (NIRD) Program. Goal of the program is to develop 5-micrometer pitch IR detectors. This value, if attained, will reach diffraction limit on most practical optical systems.

[23] R. D. Driggers, R. Vollmerhausen, J. P. Reynolds, J. Fanning, and G. C. Holt, "Infrared detector size: how low should you go?," Opt. Eng. **51**(6), 063202 (2012).

[24] K. T. Posani, V. Tripathi, S. Annamalai, N. R. Weisse-Bernstein, S. Krishna, R. Perahia, O. Crisafulli, and O. J. Painter, "Nanoscale quantum dot infrared sensors with photonic crystal cavity," Appl. Phys. Lett. **88**, 151104 (2006).

[25] K. T. Posani, V. Tripathi, S. Annamalai, S. Krishna, R. Perahia, O. Crisafulli, and O. Painter, "Quantum dot photonic crystal detectors," Proc. SPIE **6129**, 612906-1–8 (2006).

[26] S. C. Lee, S. Krishna, and S. R. J. Brueck, "Quantum dot infrared photodetector enhanced by surface plasma wave excitation," Opt. Exp. **17**(25) 23160–23168 (2009).

[27] S. Kalchmair, H. Detz, G. D. Cole, A. M. Andrews, P. Klang, M. Nobile, R. Gansch, C. Ostermaier, W. Schrenk, and G. Strasser, "Photonic crystal slab quantum well infrared photodetector," Appl. Phys. Lett. **98**, 011105 (2011).

[28] S. A. Maier, *Plasmonic: Fundamentals and Applications* (Springer, New York, 2007).

[29] J. Zhang, L. Zhang, and W. Xu, "Surface plasmon polaritons: physics and applications," J. Phys. D: Appl. Phys. **45**, 113001 (2012).

[30] P. Berini, "Surface plasmon photodetectors and their applications," Laser Photonics Rev. **8**, 197–220 (2013).

[31] R. Stanley, "Plasmonics in the mid-infrared," Nat. Photonics **6**, 409–411 (2012).

[32] D. Li and C. Z. Ning, "All-semiconductor active plasmonic system in mid-infrared wavelengths," Opt. Express **19**(15), 14594–14603 (2011).

[33] J. Rosenberg, R. V. Shenoi, S. Krishna, and O. Painter, "Design of plasmonic photonic crystal resonant cavities for polarization sensitive infrared photodetectors," Opt. Express **18**(4), 3672–3686 (2010).

[34] C.-C. Chang, Y. D. Sharma, Y.-S. Kim, J. A. Bur, R. V. Shenoi, S. Krishna, D. Huang, and S.-Y. Lin, "A surface plasmon enhanced infrared photodetector based on InAs quantum dots," Nano Lett. **10**, 1704–1709 (2010).

[35]P. Biagioni, J.-S. Huang, and B. Hecht, "Nanoantennas for visible and infrared radiation," Rep. Prog. Phys. **75**, 024402 (2012).

[36]K. Ishihara, K. Ohashi, T. Ikari, H. Minamide, H. Yokoyama, J.-I. Shikata, and H. Ito, "Therahertz-wave near field imaging with subwavelength resolution using surface-wave-assisted bow-tie aperture," Appl. Phys. Lett. **89**, 201120 (2006).

[37]P. Bouchon, F. Pardo, B. Portier, L. Ferlazzo, P. Ghenuche, G. Dagher, C. Dupuis, N. Bardou, R. Haidar, and J.-L. Pelouard, "Total funneling of light aspect ratio plasmonic nanoresonators," Appl. Phys. Lett. **98**, 191109 (2011).

[38]J. G. A. Wehner, E. P. G. Smith, G. M. Venzor, K. D. Smith, A. M. Ramirez, B. P. Kolasa, K. R. Olsson, and M. F. Vilela, "HgCdTe photon trapping structure for broadband mid-wavelength infrared absorption," J. Electron. Mater. **40**, 1840–1846 (2011).

[39]K. D. Smith, J. G. A. Wehner, R. W. Graham, J. E. Randolph, A. M. Ramirez, G. M. Venzor, K. Olsson, M. F. Vilela, and E. P. G. Smith, "High operating temperature mid-wavelength infrared HgCdTe photon trapping focal plane arrays," Proc. SPIE **8353**, 83532R (2012).

[40]D. A. G. Bruggeman, "Berechnung verschiedener physikalischer Konstanten von heterogenen Substanzen," Ann. Phys. (Leipzig) **416**, 636–679 (1935).

[41]N. K. Dhar and R. Dat, "Advanced imaging research and development at DARPA," Proc. SPIE **8353**, 835302 (2012).

[42]A. I. D'Souza, E. Robinson, A. C. Ionescu, D. Okerlund, T. J. de Lyon, R. D. Rajavel, H. Sharifi, D. Yap, N. Dhar, P. S. Wijewarnasuriya, and C. Grein, "MWIR InAs$_{1-x}$Sb$_x$ nCBn detectors data and analysis," Proc. SPIE **8353**, 835333 (2012).

[43]H. Sharifi, M. Roebuck, T. De Lyon, H. Nguyen, M. Cline, D. Chang, D. Yap, S. Mehta, R. Rajavel, A. Ionescu, A. D'Souza, E. Robinson, D. Okerlund, and N. Dhar, "Fabrication of high operating temperature (HOT), visible to MWIR, nCBn photon-trap detector arrays," Proc. SPIE **8704**, 87041U (2013).

[44]A. I. D'Souza, E. Robinson, A. C. Ionescu, D. Okerlund, T. J. de Lyon, R. D. Rajavel, H. Sharifi, N. K. Dhar, P. S. Wijewarnasuriya, and C. Grein, "MWIR InAsSb barrier detector data and analysis," Proc. SPIE **8704**, 87041U (2013).

[45]J. Schuster and E. Bellotti, "Numerical simulation of crosstalk in reduced pitch HgCdTe photon-trapping structure pixel arrays," Opt. Express **21**(12) 14712 (2013).

[46]A. White, "Infrared detectors," U.S. Patent 4,679,063 (22 September 1983).

[47]P. C. Klipstein, "Depletionless photodiode with suppressed dark current and method for producing the same," U.S. Patent 7,795,640 (2 July 2003).

[48]S. Maimon and G. Wicks, "nBn detector, an infrared detector with reduced dark current and higher operating temperature," Appl. Phys. Lett. **89**, 151109-1–3 (2006).

[49]D. Z.-Y. Ting, A. Soibel, L. Höglund, J. Nguyen, C. J. Hill, A. Khoshakhlagh, and S. D. Gunapala, "Type-II superlattice infrared detectors," in *Semiconductors and Semimetals*, edited by S. D. Gunapala, D. R. Rhiger, and C. Jagadish (Elsevier, Amsterdam, 2011), Vol. 84, pp. 1–57.

[50]G. R. Savich, J. R. Pedrazzani, D. E. Sidor, and G. W. Wicks, "Benefits and limitations of unipolar barriers in infrared photodetectors," Infrared Phys. Technol. **59**, 152–155 (2013).

[51]P. Klipstein, "XBn barrier photodetectors for high sensitivity operating temeprature infrared sensors," Proc. SPIE. **6940**, 69402U-1–11 (2008).

[52]D. Z. Ting, C. J. Hill, A. Soibel, J. Nguyen, S. A. Keo, M. C. Lee, J. M. Mumolo, J. K. Liu, and S. D. Gunapala, "Antimonide-based barrier infrared detectors," Proc. SPIE **7660**, 76601R (2010).

[53]P. Klipstein, O. Klin, S. Grossman, N. Snapi, I. Lukomsky, D. Aronov, M. Yassen, A. Glozman, T. Fishman, E. Berkowicz, O. Magen, I. Shtrichman, and E. Weiss, "XBn barrier photodetectors based on InAsSb with high operating temperatures," Opt. Eng. **50**, 061002 (2011).

[54]G. R. Savich, J. R. Pedrazzani, D. E. Sidor, S. Maimon, and G. W. Wicks, "Use of unipolar barriers to block dark currents in infrared detectors," Proc. SPIE **8012**, 8022T (2012).

[55]P. Martyniuk and A. Rogalski, "HOT infrared photodetectors," Opto-Electron. Rev. **21**, 239–257 (2013).

[56]J. B. Rodriguez, E. Plis, G. Bishop, Y. D. Sharma, H. Kim, L. R. Dawson, and S. Krishna, "nBn structure based on InAs/GaSb type-II strained layer superlattices," Appl. Phys. Lett. **91**, 043514-1–2 (2007).

[57]P. Klipstein, D. Aronov, E. Berkowicz, R. Fraenkel, A. Glozman, S. Grossman, O. Klin, I. Lukomsky, I. Shtrichman, N. Snapi, M. Yassem,

and E. Weiss, "Reducing the cooling requirements of mid-wave IR detector arrys," SPIE Newsroom (published online).

[58]M. Razeghi, S. P. Abdollahi, E. K. Huang, G. Chen, A. Haddadi, and B. M. Nquyen, "Type-II InAs/GaSb photodiodes and focal plane arrays aimed at high operating temperatures," Opto-Electron. Rev. **19**, 261–269 (2011).

[59]M. Razeghi, "Type II superlattice enables high operating temperature," SPIE Newsroom (published online).

[60]G. R. Savich, J. R. Pedrazzani, D. E. Sidor, S. Maimon, and G. W. Wicks, "Dark current filtering in unipolar barrier infrared detectors," Appl. Phys. Lett. **99**, 121112 (2011).

[61]P. C. Klipstein, Y. Gross, A. Aronov, M. ben Ezra, E. Berkowicz, Y. Cohen, R. Fraenkel, A. Glozman, S. Grossman, O. Kin, I. Lukomsky, T. Markowitz, L. Shkedy, I. Sntrichman, N. Snapi, A. Tuito, M. Yassen, and E. Weiss, "Low SWaP MWIR detector based on XBn focal plane array," Proc. SPIE **8704**, 87041S (2013).

[62]A. Khoshakhlagh, S. Myers, E. Plis, M. N. Kutty, B. Klein, N. Gautam, H. Kim, E. P. G. Smith, D. Rhiger, S. M. Johnson, and S. Krishna, "Mid-wavelength InAsSb detectors based on nBn design," Proc. SPIE **7660**, 76602Z (2010).

[63]A. M. Itsuno, J. D. Philips, and S. Velicu, "Design and modeling of HgCdTe nBn detectors," J. Electron. Mater. **40**, 1624–1629 (2011).

[64]M. Kopytko, A. Kębłowski, W. Gawron, P. Madejczyk, A. Kowalewski, and K. Jóźwikowski, "High-operating temperature MWIR nBn HgCdTe detector grown by MOCVD," Opto-Electron. Rev. **21**(42), 402–405 (2013).

[65]J. F. Klem, J. K. Kim, M. J. Cich, S. D. Hawkins, T. R. Fortune, and J. L. Rienstra, "Comparison of nBn and nBp mid-wave barrier infrared photodetectors," Proc. SPIE **7608**, 76081P (2010).

[66]H. Kroemer, "The 6.1 Å family (InAs, GaSb, AlSb) and its heterostructures: a selective review," Physica E **20**, 196–203 (2004).

[67]H. Sakaki, L. L. Chang, R. Ludeke, C. A. Chang, G. A. Sai-Halasz, and L. Esaki, "In$_{1-x}$Ga$_x$As-GaSb$_{1-y}$As$_y$ heterojunctions by molecular beam epitaxy," Appl. Phys. Lett. **31**, 211–213 (1977).

[68]Y. Wei and M. Razeghi, "Modelling of type-II InAs/GaSb superlattices using an empirical tight-binding method and interface engineering," Phys. Rev. B **69**, 085316 (2004).

[69]G. A. Umana-Membreno, B. Klein, H. Kala, J. Antoszewski, N. Gautam, M. N. Kutty, E. Plis, S. Krishna, and L. Faraone, "Vertical minority carrier electron transport in p-type InAs/GaSb type-II superlattices," Appl Phys. Lett. **101**, 253515 (2012).

[70]D. Zuo, P. Qiao, D. Wasserman, and S. L. Chuang, "Direct observation of minority carrier lifetime improvement in InAs/GaSb type-II superlattice photodiodes via interfacial layer control," Appl. Phys. Lett. **102**, 141107 (2013).

[71]E. Weiss, O. Klin, S. Grossmann, N. Snapi, I. Lukomsky, D. Aronov, M. Yassen, E. Berkowicz, A. Glozman, P. Klipstein, A. Fraenkel, and I. Shtrichman, "InAsSb-based XB$_n$n bariodes grown by molecular beam epitaxy on GaAs," J. Cryst. Growth **339**, 31–35 (2012).

[72]P. Martyniuk and A. Rogalski, "Modeling of InAsSb/AlAsSb nBn HOT detector's performance limits," Proc. SPIE **8704**, 87041X (2013).

[73]E. H. Aifer, J. G. Tischler, J. H. Warner, I. Vurgaftman, W. W. Bewley, J. R. Meyer, J. C. Kim, and L. J. Whitman, "W-structured type-II superlattice long-wave infrared photodiodes with high quantum efficiency," Appl. Phys. Lett. **89**, 053519 (2006).

[74]B.-M. Nguyen, M. Razeghi, V. Nathan, and G. J. Brown, "Type-II "M" structure photodiodes: an alternative material design for mid-wave to long wavelength infrared regimes," Proc. SPIE **6479**, 64790S (2007).

[75]B.-M. Nguyen, D. Hoffman, P.-Y. Delaunay, and M. Razeghi, "Dark current suppression in type II InAs/GaSb superlattice long wavelength infrared photodiodes with M-structure," Appl. Phys. Lett. **91**, 163511 (2007).

[76]B.-M. Nguyen, D. Hoffman, P.-Y. Delaunay, E. K. Huang, M. Razeghi, and J. Pellegrino, "Band edge tunability of *M*-structure for heterojunction design in Sb based type II superlattice photodiodes," Appl. Phys. Lett. **93**, 163502 (2008).

[77]M. Razeghi, H. Haddadi, A. M. Hoang, E. K. Huang, G. Chen, S. Bogdanov, S. R. Darvish, F. Callewaert, and R. McClintock, "Advances in antimonide-based Type-II superlattices for infrared detection and imaging at center for quantum devices," Infrared Phys. Technol. **59**, 41–52 (2013).

[78]O. Salihoglu, A. Muti, K. Kutluer, T. Tansel, R. Turan, Y. Ergun, and A. Aydinli, ""N" structure for type-II superlattice photodetectors," Appl. Phys. Lett. **101**, 073505 (2012).

[79]J. L. Johnson, L. A. Samoska, A. C. Gossard, J. L. Merz, M. D. Jack, G. H. Chapman, B. A. Baumgratz, K. Kosai, and S. M. Johnson, "Electrical

and optical properties of infrared photodiodes using the InAs/Ga$_{1-x}$In$_x$Sb superlattice in heterojunctions with GaSb," J. Appl. Phys. **80**, 1116–1127 (1996).

[80] A. Khoshakhlagh, J. B. Rodriguez, E. Plis, G. D. Bishop, Y. D. Sharma, H. S. Kim, L. R. Dawson, and S. Krishna, "Bias dependent dual band response from InAs/Ga(In)Sb type II strain layer superlattice detectors," Appl. Phys. Lett. **91**, 263504 (2007).

[81] E. Plis, H. S. Kim, G. Bishop, S. Krishna, K. Banerjee, and S. Ghosh, "Lateral diffusion of minority carriers in nBn based type-II InAs/GaSb strained layer superlattice detectors," Appl. Phys. Lett. **93**, 123507 (2008).

[82] A. D. Hood, A. J. Evans, A. Ikhlassi, D. L. Lee, and W. E. Tennant, "LWIR strained-layer superlattice materials and devices at Teledyne Imaging Sensors," J. Electron. Mater. **39**, 1001–1006 (2010).

[83] I. Vurgaftman, E. H. Aifer, C. L. Canedy, J. G. Tischler, J. R. Meyer, and J. H. Warner, "Graded band gap for dark-current suppression in long-wave infrared W-structured type-II superlattice photodiodes," Appl. Phys. Lett. **89**, 121114 (2006).

[84] E. H. Aifer, J. H. Warner, C. L. Canedy, I. Vurgaftman, E. M. Jackson, J. G. Tischler, J. R. Meyer, S. P. Powell, K. Olver, and W. E. Tennant, "Shallow-etch mesa isolation of graded-bandgap "W"-structured type II superlattice photodiodes," J. Electron. Mater. **39**, 1070–1079 (2010).

[85] D. Z.-Y. Ting, C. J. Hill, A. Soibel, S. A. Keo, J. M. Mumolo, J. Nguyen, and S. D. Gunapala, "A high-performance long wavelength superlattice complementary barrier infrared detector," Appl. Phys. Lett. **95**, 023508 (2009).

[86] E. A. DeCuir, G. P. Meissner, P. S. Wijewarnasuriya, N. Gautam, S. Krishna, N. K. Dhar, R. E. Welser, and A. K. Sood, "Long-wave type-II superlattice detectors with unipolar electron and hole barriers," Opt. Eng. **51**(12), 124001 (2012).

[87] N. Gautam, S. Myers, A. V. Barve, B. Klein, E. P. Smith, D. Rhiger, E. Plis, M. N. Kutty, N. Henry, T. Schuler-Sandyy, and S. Krishna, "Band engineering HOT midwave infrared detectors based on type-II InAs/GaSb strained layer superlattices," Infrared Phys. Technol. **59**, 72–77 (2013).

[88] W. E. Tennant, D. Lee, M. Zandian, E. Piquette, and M. Carmody, "MBE HgCdTe Technology: A very general solution to IR detection, described by 'Rule 07', a very convenient heuristic," J. Electron. Mater. **37**, 1406 (2008).

[89] D. R. Rhiger, "Performance comparison of long-wavelength infrared type II superlattice devices with HgCdTe," J. Electron. Mater. **40**, 1815–1822 (2011).

[90] S. Velicu, J. Zhao, M. Morley, A. M. Itsuno, and J. D. Philips, "Theoretical and experimental investigation of MWIR HgCdTe nBn detectors," Proc. SPIE **8268**, 82682X-1–13 (2012).

[91] P. Maryniuk and A. Rogalski, "Modelling of MWIR HgCdTe complementary barrier HOT detector," Solid-State Electron. **80**, 96–104 (2013).

[92] E. F. Schubert, L. W. Tu, G. J. Zydzik, R. F. Kopf, A. Benvenuti, and M. R. Pinto, "Elimination of heterojunction band discontinuities by modulation doping," Appl. Phys. Lett. **60**, 466–468 (1992).

[93] S. D. Gunpala, D. Z. Ting, C. J. Hill, and S. V. Bandara, U.S. Patent No. 7,737,411 (15 June 2010).

[94] N. D. Akhavan, G. Jolley, G. Umana-Membreno, J. Antoszewski, and L. Faraone, "Performance modelling of bandgap engineered HgCdTe-based nBn infrared detectors," Extended Abstracts, The 2013 Workshop on the Physics and Chemistry of II–VI Materials, Chicago, 2013.

[95] L. Zheng, M. Tidrow, L. Aitcheson, J. O'Connor, and S. Brown, "Developing high-performance III-V superlattice IRFPAs for defense – challenges and solutions," Proc. SPIE **7660**, 76601E (2010).

[96] C. J. Hill, A. Soibel, S. A. Keo, J. M. Mumolo, D. Z. Ting, S. D. Gunapala, D. R. Rhiger, R. E. Kvaas, and S. F. Harris, "Demonstration of mid and long-wavelength infrared antimonide-based focal plane arrays," Proc. SPIE **7298**, 729804 (2009).

[97] A. Soibel, J. Nguyen, B. Rafol, A. Liao, L. Hoeglund, A. Khoshakhlagh, S. A. Keo, J. M. Mumolo, J. Liu, D. Z.-Y. Ting, and S. D. Gunapala, "High-performance LWIR superlattice detectors and FPA based on CBIRD design," Proc. SPIE **8353**, 83530U (2012).

[98] P. Manurkar, S. Ramezani-Darvish, B.-M. Nguyen, M. Razeghi, and J. Hubbs, "High performance long wavelength infrared mega-pixel focal plane array based on type-II superlattices," Appl. Phys. Lett. **97**, 193505-1–3 (2010).

[99] A. Rogalski, J. Antoszewski, and L. Faraone, "Third-generation infrared photodetector arrays," J. Appl. Phys. **105**, 091101 (2009).

[100] A. M. Hoang, G. Chen, A. Haddadi, and M. Razeghi, "Demonstration of high performance bias-selectable dual-band short-/mid-wavelength infra-red photodetectors based on type-II InAs/GaSb/AlSb superlattices," Appl. Phys. Lett. **102**, 011108 (2013).

[101] M. Razeghi, A. M. Hoang, A. Haddadi, G. Chen, S. Ramezani-Darvish, P. Bijjam, P. Wijewarnasuriya, and E. Decuir, "High-performance bias-selectable dual-band short-/Mid-wavelength infrared photodetectors and focal plane arrays based on InAs/GaSb/AlSb type-II superlattices," Proc. SPIE **8704**, 87041W (2013).

[102] M. Razeghi, A. M. Hoang, G. Chen, S. Ramezani-Darvish, and P. Bijjam, "High-performance bias-selectable dual-band mid-/long-wavelength infrared photodetectors and focal plane arrays based on InAs/GaSb type-II superlattices," Proc. SPIE **8704**, 87040S (2013).

[103] M. A. Kinch, H. F. Schaake, R. L. Strong, P. K. Liao, M. J. Ohlson, J. Jacques, C-F. Wan, D. Chandra, R. D. Burford, and C. A. Schaake, "High operating temperature MWIR detectors," Proc. SPIE **7660**, 76602V (2010).

[104] W. W. Bewley, J. R. Lindle, C. S. Kim, M. Kim, C. L. Canedy, I. Vurgaftman, and J. R. Meyer, "Lifetime and Auger coefficients in type-II W interband cascade lasers," Appl. Phys. Lett. **93**, 041118 (2008).

[105] M. A. Kinch, *Fundamentals of Infrared Detector Materials* (SPIE Press, Bellingham, 2007).

[106] A. Gomez, M. Carras, A. Nedelcu, E. Costard, X. Marcadet, and V. Berger, "Advantages of quantum cascade detectors," Proc. SPIE **6900**, 69000J-1–14 (2008).

[107] F. R. Giorgetta, E. Baumann, M. Graf, Q. Yang, C. Manz, K. Köhler, H. E. Beere, D. A. Ritchie, E. Linfield, A. G. Davies, Y. Fedoryshyn, H. Jäckel, M. Fischer, J. Faist, and D. Hofstetter, "Quantum cascade detectors," IEEE J. Quantum Electron. **45**, 1039–1052 (2009).

[108] D. Hofstetter, F. R. Giorgetta, E. Baumann, Q. Yang, C. Manz, and K. Köhler, "Mid-infrared quantum cascade detectors for applications in spectroscopy and pyrometry," Appl. Phys. B **100**, 313–320 (2010).

[109] A. Buffaz, M. Carras, L. Doyennette, A. Nedelcu, P. Bois, and V. Berger, "State of the art of quantum cascade photodetectors," Proc. SPIE **7660**, 76603Q (2010).

[110] A. Buffaz, A. Gomez, M. Carras, L. Doyennette, and V. Berger, "Role of subband occupancy on electronic transport in quantum cascade detectors," Phys. Rev. B **81**, 075304-1–8 (2010).

[111] H. Schneider and H. C. Liu, *Quantum Well Infrared Photodetectors* (Springer, Berlin, 2007).

[112] R. Q. Yang, Z. Tian, Z. Cai, J. F. Klem, M. B. Johnson, and H. C. Liu, "Interband-cascade infrared photodetectors with superlattice absorbers," J. Appl. Phys. **107**, 054514-1–6 (2010).

[113] Z. Tian, R. T. Hinkey, R. Q. Yang, D. Lubyshev, Y. Qiu, J. M. Fastenau, W. K. Liu, and M. B. Johnson, "Interband cascade infrared photodetectors with enhanced electron barriers and p-type superlattice absorbers," J. Appl. Phys. **111**, 024510 (2012).

[114] N. Gautam, S. Myers, A. V. Barve, B. Klein, E. P. Smith, D. R. Rhiger, L. R. Dawson, and S. Krishna, "High operating temperature interband cascade midwave infrared detector based on type-II InAs/GaSb strained layer superlattice," Appl. Phys. Lett. **101**, 021106-1–4 (2012).

[115] J. V. Li, R. Q. Yang, C. J. Hill, and S. L. Chung, "Interbad cascade detectors with room temperature photovoltaic operation," Appl. Phys. Lett. **86**, 101102-1–3 (2005).

[116] R. T. Hinkey and R. Q. Yang, "Theory of multiple-stage interband photovoltaic devices and ultimate performance limit comparison of multiple-stage and single-stage interband infrared detectors," J. Appl. Phys. **114**, 104506-1–18 (2013).

[117] W. Pusz, A. Kowalewski, W. Gawron, E. Plis, S. Krishna, and A. Rogalski, "MWIR type-II InAs/GaSb superllatice interband cascade photodetectors," Proc. SPIE **8868**, 88680M (2013).

[118] J. Piotrowski, P. Brzozowski, and K. Jóźwikowski, "Stacked multijunction photodetectors of long-wavelength radiation," J. Electron. Mater. **32**, 672–676 (2003).

[119] H. Lotfi, R. T. Hinkey, Lu Li, R. Q. Yang, J. F. Klem, and M. B. Johnson, "Narrow-bandgap photovoltaic devices operating at room temperature and above with high open-circuit voltage," Appl. Phys. Lett. **102**, 211103 (2013).

[120] Z.-B. Tian, T. Schuler-Sandy, S. E. Godoy, H. S. Kim, J. Montoya, and S. Krishna, "Mid-wave infrared interband cascade photodetectors and focal plane arrays based on InAs/GaSb superlattices," *Photonics Conference (IPC)* (IEEE, 2013), pp. 598–599.